Green synthesis and photocatalytic properties of manganese-based oxides

Ankita Gagrani

Jan 2020

A thesis submitted for the degree of Doctor of Philosophy of

The Australian National University

This thesis, to the best of my knowledge and belief, does not contain any results previously published by another person or submitted for a degree or diploma at any university except where due reference is made in the text.

Ankita Gagrani

Jan 2020

This thesis is dedicated to the lotus feet of Shri Narayan.

Acknowledgements

I would like to express my sincere gratitude to my primary supervisor A/Prof. Takuya Tsuzuki, for his constant support and guidance during my PhD. Without his motivation, encouraging words and very balanced guidance, I would have never been able to gather strength to carry on during hard times of my PhD. Most importantly, I would like to thank him for teaching me, by his own example, the value of ethics, kindness, mindfulness, punctuality and hard work. I am honoured to have worked under such a supervisor from whom I learned much more than just "*scientific research*". I will always remember and apply these lessons while meeting the challenges in my life ahead. I would also like to thank my committee members, Dr. Antonio Tricoli, Dr. Adrian Lowe and Dr. Michael Cheah for serving as my committee members and offering me valuable suggestions and guidance.

Through this PhD program, I have been lucky to collaborate with Dr. Gerhard Swiegers and Mr. Mohammed Alsultan at the University of Wollongong, Australia. A special thanks to Dr. Ronald Pace for his help in establishing the collaboration. I have also been fortunate to work in collaboration with Dr. Olinda C. Monteiro and Ms. Sara Sousa at the University of Lisbon, Portugal. I would like to thank them for offering their time, valuable knowledge and lab facilities.

I would also like to acknowledge the assistance of CAM staff members and technical and administrative staff members of Research School of Electrical, Energy and Materials Engineering for extending a warm and friendly hand to help setup my experiments, give me better ideas and keeping me safe at work. I would also like to acknowledge financial support

through ANU PhD scholarship, ANU HDR Fee Remission Merit Scholarship and Australian Government Research Training Program Fee-Offset Scholarship.

I would like to say a special thanks to my colleagues Ms. Joyce Yeoh, Mr. Jingwei Zhou, Mr. Bolun Ding, Mr. Yang Wang, Mr. Mahdiar Taheri, Ms. Elmira Mohammed, Mr. Ankur Sharma and Mr. Jun Peng for their friendship and support, and for creating an energetic working environment.

I am extremely grateful to Dr. Apurv Kumar for constantly motivating me, helping me with scientific and non-scientific troubles and teaching me the importance and application of "service attitude" in life. I am also thankful to his wife, Ms. Chandni Kumar, for feeding me delicious homemade Indian food at countless occasions and taking care of me like a mother in Canberra. Their love, care and teachings have permanently changed my world. I am also very lucky to have a strong friend like Richa Awasthy. We shared our happiness, pains and thoughts about everything that exists in and beyond this universe. Those discussions kept me motivated and helped me in staying sane during PhD. Also, a big thanks to my friends, Parbinder Kaur, Priya Srivastava, Amitesh Kumar, Anand Krishna, Deepu Ashok, Siddharth Iyer, B.V. Mahesh and other well-wishers for always keeping me motivated with their friendly advices and jokes.

My life in Canberra, particularly the last one year, would have never been so comfortable without the support and care of my sister, Nikita Gagrani. Despite being a busy and full time PhD student, she took care of all the household chores so that I could focus completely on my research work and health. A big thanks to her!

And finally, a humble obeisance to my family, especially parents, grandparents and brother, for their unparalleled love, help and support.

List of Publications

Published Articles

1. **Ankita Gagrani**, Jingwei Zhou, Takuya Tsuzuki, "*Solvent free mechanochemical synthesis of MnO_2 for the efficient degradation of Rhodamine-B*", Ceramics International, 44, 4694-4698, 2018.
2. **Ankita Gagrani**, Takuya Tsuzuki, "*Calcium manganese oxides as biomimetic catalysts in energy applications: A short review*", Chemical Engineering Science, 194, 116-126, 2019.
3. **Ankita Gagrani**, Yang Wang, Bolun Ding, Takuya Tsuzuki, "*pH dependent catalytic redox properties of Mn_3O_4 nanoparticles*", Materials Chemistry and Physics, 231, 41-47, 2019.
4. **Ankita Gagrani**, Mohammed Alsultan, Gerhard F Swiegers, Takuya Tsuzuki, "*Photo-electrochemical oxygen evolution reaction by biomimetic $CaMn_2O_4$ catalyst*", Applied Sciences, 9, 2196, 2019.

Manuscripts Under Preparation

1. **Ankita Gagrani**, Sara Sousa, Olinda C Monteiro, Takuya Tsuzuki, "*Green synthesis and photocatalytic activity of calcium manganese oxides catalysts*".
2. **Ankita Gagrani**, Mohammed Alsultan, Gerhard F Swiegers, Takuya Tsuzuki, *"Photo-electrochemical oxygen evolution reaction by manganese-based oxides"*.

Abstract

In recent years, manganese-based oxides, particularly calcium manganese oxides, have attracted significant interest as a new class of bio-mimetic catalysts, due to their elemental and structural similarity to the natural photocatalytic centre in plant cells. In natural photosynthesis, bio-electricity decomposes water into hydrogen and oxygen within a unique catalytic centre composed of a $CaMn_4O_5$ cluster, in the oxygen evolving complex (OEC) enzyme hidden in the Photosystem II protein. Inspired by this nature's solar technology, calcium manganese oxides have been explored as photo catalysts in sustainability-related application including the generation of clean hydrogen fuel through water splitting.

For this application, calcium manganese oxides have some unique advantages over other common photocatalysts, (i) bang gap energy allowing the absorption of visible light to utilise a wide range of solar spectrum, and (ii) constitution of low cost, Earth abundant and environment friendly elements. The combination of these unique properties makes calcium manganese oxides a suitable choice as a photocatalyst for a large-scale operation in an eco-friendly manner.

However, there are still considerable research gaps in the catalytic applications of calcium manganese oxides. For example, investigation into the catalysis of calcium manganese oxides has been carried out mostly without light irradiation and there is little knowledge about how and which calcium manganese oxides behave as a photocatalyst or as an electrode material in photo-electrochemical cells. Furthermore, information critical to these light-driven applications, such as band edge position and bandgap energy, is still lacking for calcium manganese oxides. Moreover, the relationship between catalytic performance under light and

different structural parameters such as manganese oxidation states, structural similarity to the natural OEC cluster, and morphology of the catalyst, is not fully understood. Also, the role of calcium in the catalysis is not known. There is also a strong need to develop new techniques to synthesise nanoscale catalysts that have less environmental impacts than conventional solvent-based methods.

In this study, a solvent-free method to synthesize manganese-based oxide catalysts was developed. MnO_2, $Ca_2Mn_3O_8$, $CaMn_2O_4$ and $CaMnO_3$ ultrafine particles were successfully synthesized in two steps; mechanochemical processing and subsequent heat treatment. The study of band-edge position and bandgap energy revealed that theoretically the selected manganese-based oxide catalysts can absorb the visible solar spectrum, degrade organic pollutants by free-radical generation, and generate oxygen through photo-electro-catalytic water splitting. However, experimentally, at pH 7, manganese oxides and calcium manganese oxides showed poor charge transfer efficiency, leading to poor photo-catalytic dye degradation. For the study of photo-electrochemical water splitting, polypyrrole, a conducting polymer, was used along with catalyst powders in the anode of a photo-electrochemical cell, to increase charge separation efficiency. This study also identified that oxygen evolution catalysis by $CaMn_2O_4$ is affected more by surface area than particle morphology.

This work has added new knowledge into the research field of bio-inspired photocatalysts. In this work, potentially green and scalable techniques to produce manganese-based oxide catalysts were developed. The photocatalytic performance of manganese-based oxides in dye decolourisation were investigated under various conditions. Their catalytic and photocatalytic water oxidation performance was investigated using a photo-electrochemical cell and the effects of particle morphology, manages oxidation states and crystal structures on the water

splitting reaction were elucidated. These findings will be helpful in designing sustainable technologies for the environment.

Table of Contents

List of Figures

$CaMn_2O_4$ particles, and (c) polypyrrole containing $CaMn_2O_4$ nanowires. (*='light on', #='light off').

Figure 6.6 GC traces of collected gases (a) reference, (b) in the dark, and (c) under light irradiation.

Figure 6.7 (a) Nyquist and (b) Bode plots showing measured data (individual data points) and modelled data (solid lines) using the equivalent circuit depicted in (c): (i) $CaMn_2O_4$ nanowires /PPy (with light illumination),(ii) $CaMn_2O_4$ nanowires / PPy (without light illumination), (iii) irregular-shaped $CaMn_2O_4$ particles / PPy (with light illumination), (iv) irregular-shaped $CaMn_2O_4$ particles / PPy (without light illumination) (dark), (v) PPy only (with light illumination) and (vi) PPy only (without light illumination).

Figure 6.8 Tafel plots of (i) $CaMn_2O_4$ nanowires /PPy (with light illumination), (ii) $CaMn_2O_4$ nanowires /PPy (without light illumination, (iii) irregular-shaped $CaMn_2O_4$ particles /PPy (with light illumination), (iv) irregular-shaped $CaMn_2O_4$ particles /PPy (without light illumination) (dark), (v) PPy only (with light illumination) and (vi) PPy only (without light illumination).

List of Tables

Data from Tafel plot studies (slope (A), exchange current density (i_o)). ‘dark’ = without light illumination; ‘light’ = with light illumination.

Commonly Used Acronyms

AOS	Average oxidation state
BET	Brunauer-Emmett-Teller
CA	Chronoamperograms
CB	Conduction band
EIS	Electrochemical impedance spectroscopy
FESEM	Field emission scanning electron microscope
FTO	Fluorine doped tin oxide
GC	Gas chromatograph
HOMO	Highest occupied molecular orbital
LHE	Light harvesting efficiency
LSV	Linear sweep voltammetry
LUMO	Lowest unoccupied molecular orbital
NHE	Normal hydrogen electrode
OEC	Oxygen evolving complex
OER	Oxygen evolution reaction
ORR	Oxygen reduction reaction
PEC	Photo-electro chemical

PPy	Polypyrrole
Pt	Platinum
PSII	Photosystem-II
Rh6G	Rhodamine 6G
RhB	Rhodamine B
RPM	Revolutions per minute
SEM	Scanning electron microscope
SSA	Specific surface area
TEM	Transmission electron microscope
TOF	Turn over frequency
UV	Ultraviolet
VB	Valence band
Vis	Visible
XANES	X-ray absorption near edge structure
XPS	X-ray photoelectron spectroscopy
XRD	X-ray diffraction

Chapter 1

Introduction

1.1 Background and motivation

Global energy demand is rapidly rising due to the increase in population and living standards. However, most energy generation still relies on fossil fuels. This situation poses a significant challenge to the 21st century, because of green-house gas emission and diminishing fuel supplies. Alternative energy sources must be developed to provide sustainable energy and environmental security for the future. A highly promising technology is to use clean fuels, such as hydrogen. Hydrogen is recognised as clean for both combustion and fuel-cell operations. As fuel, it does not emit harmful by-products or green-house gases. Its specific energy storage capacity, 120 MJ/kg, is much higher than gasoline (40 MJ/kg) or lithium batteries (8 MJ/kg). It can be stored as gas, liquid or solid, making it portable and easily transportable. However, currently, fossil fuels are the dominant source (>90%) of hydrogen fuel. Therefore, it is critical to develop cleaner alternative methods for its production. A highly promising technology is to produce hydrogen from water, by splitting water into H_2 and O_2. This approach offers a potential solution for meeting the world's escalating energy demand in an environmentally friendly manner [1].

Photosynthesis, nature's solar technology, is the most efficient water-splitting system known. The reaction occurs within the Photosystem-II proteins (PSII) in plant cells, where $CaMn_4O_5$ clusters are the key structural component responsible for the reaction to splits water in the presence of sunlight [2]. This cluster evolved three billion years ago and has supported nearly all the life to prosper on Earth [2]. The idea of biological water splitting in the natural system has inspired researchers to produce hydrogen fuel by splitting water using catalyst and sunlight, an abundant, renewable and carbon-neutral energy source [3, 4].

Thermodynamically, photocatalysts for water splitting applications should have their bottom of the conduction band more negative than the H^+/H_2 redox potential (0 V vs NHE at pH=0) and their top of the valence band more positive than the O_2/OH^- redox potential (+1.23 V vs NHE at pH =0), as shown in Figure 1.1 [5].

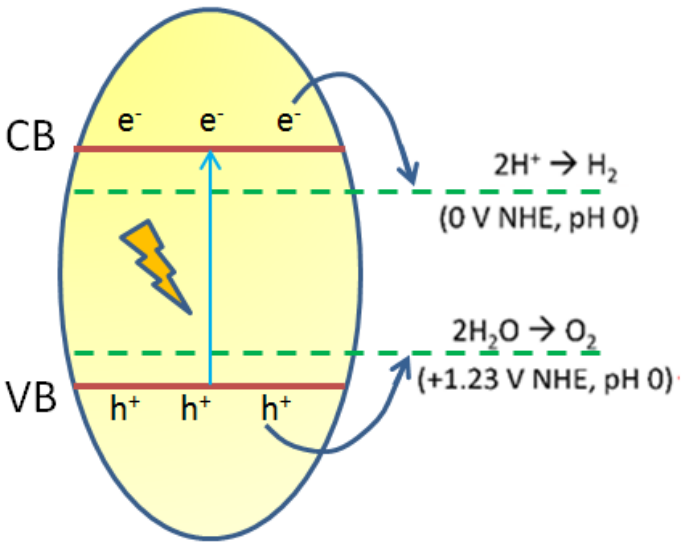

Figure 1.1. Mechanism of photocatalytic water splitting.

A variety of photocatalysts, consisting of different elements such as iron [6], titanium [7], zinc [8], cobalt [9], manganese [10] and other heavy metals [11-13], have been developed for water splitting. However, it is still challenging to develop efficient photocatalysts with non-toxic elements that works under visible light.

To develop an effective water-oxidation catalyst, biomimetic approach is useful, especially from the sustainability point of view. In fact, the $CaMn_4O_5$-cluster in PSII is low cost and made of earth-abundant elements, which operates near pH neutral conditions at room temperature under visible light. To understand the role and water splitting mechanism of $CaMn_4O_5$-cluster

in PSII, several investigations have been carried out to identify its structure [16-19]. Among them, the geometric cubane-like arrangement within the $CaMn_4O_5$ cluster, reported by Umena *et al*., at 1.9 Å resolution, is still the highest resolution structural information available today [17]. Although the water splitting mechanism of the $CaMn_4O_5$ cluster in PSII is still largely unknown [20-22], these structural studies of PSII have provided valuable guidance to developing efficient Ca-Mn-O-based catalysts for water oxidation and artificial photosynthesis by imitating the $CaMn_4O_5$ cluster, in terms of elemental compositions, oxidation states of manganese and atomic arrangement [23, 24].

In recent years, several articles have discussed multiple topics related to the catalytic properties of manganese-based oxide compounds. These include the structure of natural $CaMn_4O_5$-cluster [17, 25], their water oxidation mechanism [22, 26, 27], synthesis methods of $CaMn_4O_4$-based organometallic compounds [28-30], artificial water oxidation [10, 31, 32] and its energetic basis [33], as well as other catalytic applications [29, 34-37]. In particular, ceramic calcium manganese oxides have been subject of recent research activities due to its structural similarity to the natural $CaMn_4O_5$ cluster within PSII [14, 15].

Despite these prior works, there are critical knowledge gaps that need to be addressed, for producing hydrogen fuel using manganese and calcium manganese oxides. For example, the sustainability aspect of the production process of the catalysts is essential to the technology uptake but rarely addressed in the literature. In addition, it is not fully understood how their crystal structure, energy band structure and morphology affect the photocatalytic performance and water splitting efficiency of manganese and calcium manganese oxides. This thesis aims to fill these research gaps to develop a new class of green photocatalysts for solar-driven water splitting.

1.2 Structure of the thesis

Chapter 1 gives a brief overview of the background and motivation of the project.

In **Chapter-2,** a critical literature review is given to understand the detailed knowledge relevant to the project. The Literature review aims to explain important aspects of synthesis, crystal structure and other physicochemical characteristics of calcium manganese oxides, and their potential applications in photocatalytic dye degradation and water splitting. Previous research in water splitting using various manganese oxides is reviewed. The current knowledge about the role of calcium in calcium manganese oxides for catalytic water splitting is presented. Finally, research gaps in understanding the photocatalytic activities of these compounds are identified to define the aims and scope of the present project.

Chapter 3 reports the experimental investigation of the synthesis of amorphous and crystalline MnO_2 and their dye decolourization abilities. The study demonstrates the importance of dry mechanochemical methods for the green production of manganese oxides. The study reveals that amorphous MnO_2 nanoparticles give a higher dye-degradation rate than crystalline MnO_2 nanorods under simulated sunlight and that the degradation rate is higher under acidic conditions.

Chapter 4 reports the experimental investigation of the synthesis of different calcium manganese oxides nanoparticles ($Ca_2Mn_3O_8$, $CaMn_2O_4$ and $CaMnO_3$) and their photocatalytic activities on the decolourization of Rhodamine 6G aqueous solutions. Synthesis conditions using dry mechanochemical processing is investigated and physicochemical characteristics of resulting nanoparticles, including band edge positions, are studied. A mechanism of dye

degradation is proposed from an electrochemical point of view, using an energy band diagram. The chapter reports that the photocatalytic activity of the prepared powders increases in the order $Ca_2Mn_3O_8 < CaMnO_3 < CaMn_2O_4$.

Chapter 5 presents the experimental results of water splitting using the catalytic compounds studied in Chapters 3 and 4. Their catalytic performance was compared and the reasons behind the difference in their performances are discussed. The Chapter also includes a theoretical study of goodness-of-fit of the crystal structures of synthesized calcium manganese oxides against calcium manganese cluster ($CaMn_4O_5$) in the natural photocatalytic centre in plant cells and discusses the effect of manganese oxidation state and role of calcium in water splitting.

In **Chapter 6**, the influence of particle morphology (nanowires and irregular-shaped particles) on the photo-electrocatalytic water splitting is investigated, using the best performing compound identified in Chapter 5. Nanowires and irregular-shaped particles were synthesized using mechanochemical processing and a hydrothermal method, respectively. The results of electrochemical impedance spectroscopy, and gas chromatograph analysis are discussed to understand the nature of the catalytic process and the effects of particle morphology.

Chapter 7 presents a conclusion by combining the results of the previous chapters, to answer the research question. The Chapter also covers suggestions for future work.

Appendix 1 describes the pH dependent redox catalytic activities of mechanochemically synthesized Mn_3O_4 nanoparticles with sizes between 10-90 nm.

1.3 References

1. Tachibana, Y., Vayssieres, L. and Durrant, J.R., 2012. *Artificial photosynthesis for solar water-splitting*. Nature Photonics, 6, pp.511-518.
2. Najafpour, M.M., 2011. *Calcium-manganese oxides as structural and functional models for active site in oxygen evolving complex in photosystem II: lessons from simple models*. Journal of Photochemistry and Photobiology B: Biology, 104, pp.111-117.
3. Grewe, T., Meggouh, M. and Tüysüz, H., 2016. *Nanocatalysts for solar water splitting and a perspective on hydrogen economy*. Chemistry–An Asian Journal, 11, pp.22-42.
4. Walter, M.G., Warren, E.L., McKone, J.R., Boettcher, S.W., Mi, Q., Santori, E.A. and Lewis, N.S., 2010. *Solar water splitting cells*. Chemical reviews, 110, pp.6446-6473.
5. Currao, A., 2007. *Photoelectrochemical water splitting*. CHIMIA International Journal for Chemistry, 61, pp.815-819.
6. Sivula, K., Le Formal, F. and Grätzel, M., 2011. *Solar water splitting: progress using hematite (α-Fe_2O_3) photoelectrodes*. ChemSusChem, 4, pp.432-449.
7. Ni, M., Leung, M.K., Leung, D.Y. and Sumathy, K., 2007. *A review and recent developments in photocatalytic water-splitting using TiO_2 for hydrogen production*. Renewable and Sustainable Energy Reviews, 11, pp.401-425.
8. Maeda, K., Takata, T., Hara, M., Saito, N., Inoue, Y., Kobayashi, H. and Domen, K., 2005. *GaN: ZnO solid solution as a photocatalyst for visible-light-driven overall water splitting*. Journal of the American Chemical Society, 127, pp.8286-8287.
9. Artero, V., Chavarot-Kerlidou, M. and Fontecave, M., 2011. *Splitting water with cobalt.* Angewandte Chemie International Edition, 50, pp.7238-7266.
10. Najafpour, M.M., Rahimi, F., Aro, E.M., Lee, C.H. and Allakhverdiev, S.I., 2012. *Nano-sized manganese oxides as biomimetic catalysts for water oxidation in artificial photosynthesis: a review*. Journal of the Royal Society Interface, 9, pp.2383-2395.
11. Tang, C., Cheng, N., Pu, Z., Xing, W. and Sun, X., 2015. *NiSe nanowire film supported on nickel foam: an efficient and stable 3D bifunctional electrode for full water splitting.* Angewandte Chemie International Edition, 54, pp.9351-9355.
12. Kim, T.W. and Choi, K.S., 2014. *Nanoporous $BiVO_4$ photoanodes with dual-layer oxygen evolution catalysts for solar water splitting*. Science, 343, pp.990-994.
13. Duan, L., Bozoglian, F., Mandal, S., Stewart, B., Privalov, T., Llobet, A. and Sun, L., 2012. *A molecular ruthenium catalyst with water-oxidation activity comparable to that of photosystem II. Nature chemistry*, 4, pp.418-423.
14. Bourajoini, H., Rautio, A.R., Kordas, K. and Mikkola, J.P., 2016. *Calcium Manganese oxide catalysts for water oxidation: Unravelling the influence of various synthesis strategies*. Materials Research Bulletin, 79, pp.133-137.
15. Najafpour, M.M., Pashaei, B. and Nayeri, S., 2012. *Calcium manganese (IV) oxides: biomimetic and efficient catalysts for water oxidation*. Dalton Transactions, 41, pp.4799-4805.
16. Ferreira, K.N., Iverson, T.M., Maghlaoui, K., Barber, J. and Iwata, S., 2004. *Architecture of the photosynthetic oxygen-evolving center*. Science, 303, pp.1831-1838.
17. Umena, Y., Kawakami, K., Shen, J.R. and Kamiya, N., 2011. *Crystal structure of oxygen-evolving photosystem II at a resolution of 1.9 Å*. Nature, 473, pp.55-60.
18. Guskov, A., Kern, J., Gabdulkhakov, A., Broser, M., Zouni, A. and Saenger, W., 2009. *Cyanobacterial photosystem II at 2.9-Å resolution and the role of quinones, lipids, channels and chloride*. Nature structural & molecular biology, 16, pp.334-342.
19. Zouni, A., Witt, H.T., Kern, J., Fromme, P., Krauss, N., Saenger, W. and Orth, P., 2001. *Crystal structure of photosystem II from Synechococcus elongatus at 3.8 Å resolution*. Nature, 409, pp.739-743.
20. Dau, H., Limberg, C., Reier, T., Risch, M., Roggan, S. and Strasser, P., 2010. *The mechanism of water oxidation: from electrolysis via homogeneous to biological catalysis.* ChemCatChem, 2, pp.724-761.

21. Najafpour, M.M., 2011. *Oxygen evolving complex in Photosystem II: Better than excellent.* Dalton Transactions, 40, pp.9076-9084.
22. Vrettos, J.S., Limburg, J. and Brudvig, G.W., 2001. *Mechanism of photosynthetic water oxidation: combining biophysical studies of photosystem II with inorganic model chemistry*. Biochimica et Biophysica Acta (BBA)-Bioenergetics, 1503, pp.229-245.
23. Zhang, C., Chen, C., Dong, H., Shen, J.R., Dau, H. and Zhao, J., 2015. *A synthetic Mn_4Ca-cluster mimicking the oxygen-evolving center of photosynthesis*. Science, 348, pp.690-693.
24. Zaharieva, I., Najafpour, M.M., Wiechen, M., Haumann, M., Kurz, P. and Dau, H., 2011. *Synthetic manganese–calcium oxides mimic the water-oxidizing complex of photosynthesis functionally and structurally*. Energy & Environmental Science, 4, pp.2400-2408.
25. Yano, J., Kern, J., Sauer, K., Latimer, M.J., Pushkar, Y., Biesiadka, J., Loll, B., Saenger, W., Messinger, J., Zouni, A. and Yachandra, V.K., 2006. *Where water is oxidized to dioxygen: structure of the photosynthetic Mn4Ca cluster.* Science, 314, pp.821-825.
26. Britt, R.D., Campbell, K.A., Peloquin, J.M., Gilchrist, M.L., Aznar, C.P., Dicus, M.M., Robblee, J. and Messinger, J., 2004. *Recent pulsed EPR studies of the photosystem II oxygen-evolving complex: implications as to water oxidation mechanisms*. Biochimica et Biophysica Acta (BBA)-Bioenergetics, 1655, pp.158-171.
27. Pecoraro, V.L., Baldwin, M.J., Caudle, M.T., Hsieh, W.Y. and Law, N.A., 1998. *A proposal for water oxidation in photosystem II*. Pure and applied chemistry, 70, pp.925-929.
28. Zhou, Q. and Kennedy, B.J., 2006. *Thermal expansion and structure of orthorhombic $CaMnO_3$.* Journal of Physics and Chemistry of Solids, 67, pp.1595-1598.
29. Khanahmadzadeh, S., Mikaeili, N. and Hasanpour, S., 2017. *Facile synthesis of $CaMn_2O_4$ nanoparticles and investigation of photocatalytic activity, optical and magnetic properties and its influence on the thermal stability of polymeric nanocomposite*. Journal of Materials Science: Materials in Electronics, 28, pp.4521-4529.
30. de Muro, I.G., Insausti, M., Lezama, L. and Rojo, T., 2005. *Morphological and magnetic study of $CaMnO_{3-x}$ oxides obtained from different routes*. Journal of Solid State Chemistry, 178, pp.928-936.
31. Rong, F., Zhao, J., Chen, Z., Xu, Y., Zhao, Y., Yang, Q. and Li, C., 2016. *Highly active water oxidation on nanostructured biomimetic calcium manganese oxide catalysts.* Journal of Materials Chemistry A, 4, pp.6585-6594.
32. Baktash, E., Zaharieva, I., Schröder, M., Goebel, C., Dau, H. and Thomas, A., 2013. *Cyanamide route to calcium–manganese oxide foams for water oxidation*. Dalton Transactions, 42, pp.16920-16929.
33. Birkner, N., Nayeri, S., Pashaei, B., Najafpour, M.M., Casey, W.H. and Navrotsky, A., 2013. *Energetic basis of catalytic activity of layered nanophase calcium manganese oxides for water oxidation.* Proceedings of the National Academy of Sciences, 110, pp.8801-8806.
34. Hu, Y., Han, X., Zhao, Q., Du, J., Cheng, F. and Chen, J., 2015. *Porous perovskite calcium–manganese oxide microspheres as an efficient catalyst for rechargeable sodium–oxygen batteries.* Journal of Materials Chemistry A, 3, pp.3320-3324.
35. Dias, J.M., Alvim-Ferraz, M.C.M., Almeida, M.F., Díaz, J.D.M., Polo, M.S. and Utrilla, J.R., 2013. *Biodiesel production using calcium manganese oxide as catalyst and different raw materials.* Energy conversion and management, 65, pp.647-653.
36. Barrocas, B., Sério, S. and Melo Jorge, M.E., 2014. *Hierarchically grown $CaMn_3O_6$ nanorods by RF magnetron sputtering for enhanced visible-light-driven photocatalysis*. The Journal of Physical Chemistry C, 118, pp.24127-24135.
37. Wang, Y., Xie, Y., Sun, H., Xiao, J., Cao, H. and Wang, S., 2016. *Hierarchical shape-controlled mixed-valence calcium manganites for catalytic ozonation of aqueous phenolic compounds*. Catalysis Science & Technology, 6, pp.2918-2929.

Chapter 2

Literature Review

Remarks:

The publication relevant to this chapter is "Ankita Gagrani, Takuya Tsuzuki, "*Calcium manganese oxide as biomimetic catalysts in energy applications: A short review*", **Chemical Engineering Science**, 194, 116-126, **2019**". The publication contains a comprehensive review of the synthesis and applications of calcium manganese oxides. The chapter contains the part of the publication relevant in defining the scope of the thesis. The chapter also contains additional information to present a clear understanding of the research questions addressed in the thesis.

Abstract

This chapter introduces a critical review of the recent research results concerning the synthesis and photocatalytic applications of calcium manganese oxides. Current knowledge gaps are summarised and research questions in the present project are articulated towards the end of the chapter.

2.1 Natural Photosynthesis

Oxygenic photosynthesis, supported by the sun, is the most crucial natural process for the existence of life on our planet. Cyanobacteria algae are considered to have started the process many millions of years ago [1]. Today, photosynthesis is the major process used to convert sunlight into chemical energy on Earth. It serves as a model process to artificially generate hydrogen fuel using sunlight and water, to solve energy crisis. The basic reaction of photosynthesis is:

$$6\ CO_2 + 6\ H_2O \xrightarrow[\text{energy}]{\text{light}} C_6H_{12}O_6 + 6\ O_2 \qquad (2.1).$$

The photochemical reaction in photosynthesis is a redox reaction, where CO_2, taken from the atmosphere, acts as an electron acceptor and H_2O as an electron donor to form a carbohydrate molecule. The resulting sugar molecule stores light energy as chemical energy, which can be released to fuel the life on the planet. Oxygen is released as a by-product of the process.

In higher plants, photosynthesis occurs in a cellular structure known as chloroplasts. Chloroplasts contain thylakoid membranes, which are embedded with Photosystem II (PSII) enzymes. PSII, having a molecular weight of 650 kDa, is a dimeric protein complex that is responsible for catalysing photosynthetic water oxidation [2]. According to the latest 1.9 Å resolution structure, each PSII core complex consists of 20 proteins, 35 chlorophylls, 2 pheophytins, 11 β-carotenes, more than 20 lipids, 2 plastoquinones, 2 heme iron, 1 non-heme iron, 3 chloride ions, 1 bicarbonate ion, more than 15 detergents in a monomer, more than 1300 water molecules, 4 manganese atoms and 3 or 4 calcium atoms (one of which in the Mn_4CaO_5 cluster) [3]. The $CaMn_4O_5$ cluster, the so-called oxygen evolving centre (OEC) within PSII

proteins, is the key catalyst used for light-induced water oxidation in natural photosynthesis. Other entities, bounded by the PSII core proteins, are responsible for the electron transport within the reaction centre to produce O_2 from water [4-7].

2.2 Concept of artificial photosynthesis

The idea of biological water splitting in the natural system has inspired researchers to produce hydrogen fuel by splitting water using sunlight, an abundant, renewable and carbon-neutral energy source [8]. This approach offers a potential solution to meeting the world's escalating energy demand, in an environmentally friendly manner [9]. Although the concept of "artificial photosynthesis" was first anticipated many years ago by Italian chemist Giacomo Ciamician [10], the practicality of the idea received recognition in late 1960, soon after the discovery of the photocatalytic properties of titania by Fujishima and Honda [11].

Artificial photosynthesis, which is achieved by employing either organic or inorganic catalysts or their composites, is considered advantageous due to its high theoretical efficiency and requirements of relatively simple engineering facilities. The core strategy to achieve artificial photosynthesis is to find an efficient catalyst to split water under ambient conditions. Water splitting can be achieved by either using a single catalyst to split water to H_2 and O_2 simultaneously or using two different catalysts for oxygen and hydrogen generation, according to Eq (2.2) and (2.3) [12].

$$2H_2O \longrightarrow O_2 + 4H^+ + 4e^- \quad (2.2)$$

$$4H^+ + 4e^- \longrightarrow 2H_2 \quad (2.3)$$

Following subsections discuss the different ways to carry out water oxidation and provide a brief overview of OER catalysts.

2.2.1 Methods of water splitting

2.2.1.1 Chemically driven catalytic water oxidation

For chemically driven catalytic water oxidation, a sacrificial chemical oxidant is used to chemically activate a transition-metal catalyst, as shown in Figure 2.1.

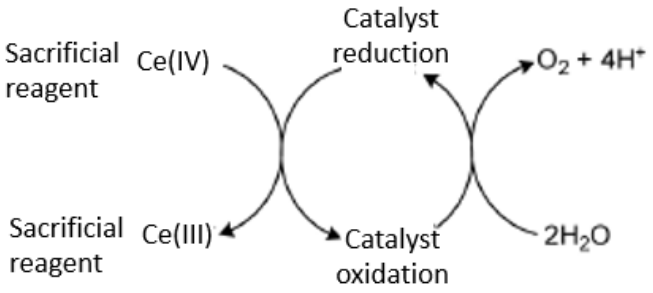

Figure 2.1. Schematic of chemical water splitting.

Ce(IV) salts are the most commonly used chemical oxidant. The main advantages of this approach are possibility of studies for a longer duration (for a stable oxidant), establishment of uniform contact between oxidant and catalyst, and ease of operation. On the other hand, irreversible consumption and high over-potentials (energetical inefficiency) are the major disadvantages of this approach.

2.2.1.2 Electro-catalytic water splitting

Electrocatalytic water splitting approach helps in addressing some of the challenges of chemically driven catalytic water oxidation [13]. Electrocatalytic water splitting is composed of two half reactions: hydrogen evolution on the cathode and oxygen evolution on the anode, as shown in Figure 2.2. Although the theoretical minimum energy required to drive the phenomenon is 1.23 V, commercial electrolysers typically require additional 0.6-0.8 V as the so-called over-potential [14]. This over-potential is largely caused by an accumulation of energy barriers in each step of electron transfer for O_2 generation; O_2 generation requires four electron transfer and simultaneous multiple electron transfer is not kinetically favourable. To overcome the over-potential, often electro-catalysts are selected in such a manner that they can produce maximum current density with minimum potential and stay stable in the system. To achieve this, several strategies are adopted, including selection of materials, increased surface area, introduction of structural defects, doping, protection layer deposition [14].

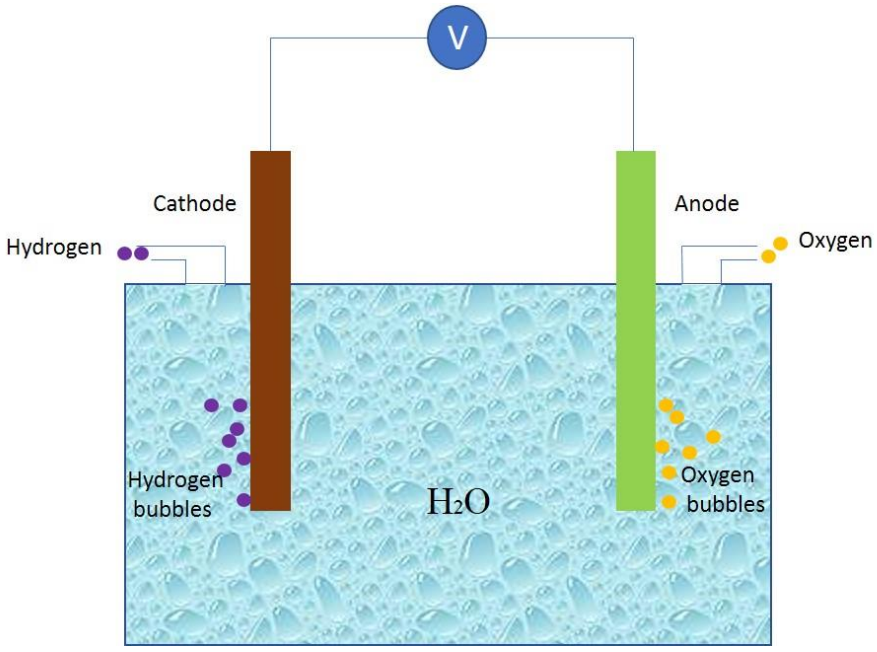

Figure 2.2. Schematic of electrochemical water splitting.

A variety of electrocatalysts that are based on precious metals [15-16], Co [14], Mn [17] and other elements [18], have been reported. Even though catalysts can reduce the over-potential, electrochemical water splitting requires an external energy source. The idea of obtaining external energy from the Sun, has gained significant interest in recent years. This has given rise to the concept of visible light photon-induced water splitting.

2.2.1.3 Photo-catalytic and Photo-electro-catalytic water splitting

Visible light driven water splitting can be achieved by using two methods. The first method is to use a photosensitizer, a sacrificial electron acceptor and a water oxidation catalyst in a three-component system. A photosensitizer absorbs light, energetically excites electrons and transfers exited electrons to the sacrificial electron acceptor. This generates a higher oxidation state of the photosensitizer, which in turn promotes the oxidation of the catalyst and oxygen generation by splitting water [13]. The schematic of the process is shown in Figure 2.3. The stability of photosensitizers and charge transfer kinetics are the major challenges of this approach [13].

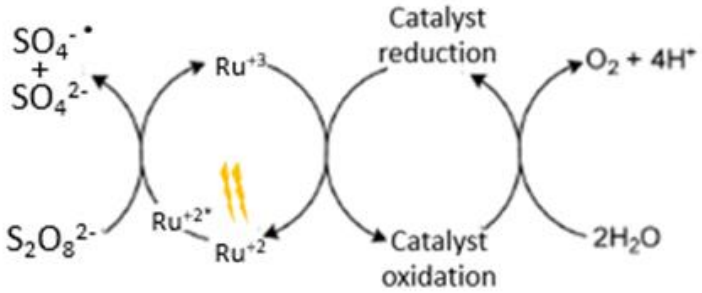

Figure 2.3. Schematic of photochemical water splitting.

These molecules can also be immobilized on electrodes and used as photoanodes in the water-splitting cell, which is the second method.

While constructing photoanodes, it is also possible to eliminate photosensitizers and instead to employ a semiconductor material, capable of charge separation by utilizing visible light photons, thus assisting in oxygen and hydrogen production via Equations 2.2 and 2.3. As shown in Figure 1.1, an ideal photo-catalyst must have its bottom of the conduction band more negative than the H^+/H_2 redox potential (0 V vs NHE at pH=0) and the top of the valence band more positive than the O_2/OH- redox potential (+1.23 V vs NHE at pH =0), and a band gap that that can absorb most of the solar spectrum [19]. These stringent requirements make the conception of a single photosystem very difficult. To overcome these barriers, a dual photosystem with two light-absorbers (n-type photoanode and p-type photocathode) has been proposed [19]. However, for the maximum efficiency, it requires both types of semiconductors to absorb complementary wavelength ranges, which narrows down the choice of available materials [20-21]. Therefore, a single photosystem with a small band gap photo-catalyst as an anode and a metal (usually platinum) as a cathode, is commonly utilized. Between these two half reactions, OER is an uphill reaction, with a driving potential of 1.23 V vs NHE. However, in reality, potential greater than 1.23 V vs NHE is required to generate oxygen due to kinetic barriers such as electrical resistance of the system. Hence, it is important to synthesize an OER catalyst capable of overcoming the high kinetic barrier at a lower over-potential. For spontaneous charge transfer, Fermi level of the cathode must be more negative than the H^+/H_2 redox potential. However, if these conditions are not met, an external bias is required to elevate the Fermi level of the cathode, and the process is termed as “photo-electrochemical water splitting”, as shown in Figure 2.4. External bias also provides energy to overcome system resistance (over potential) and help facilitate the reactions [22].

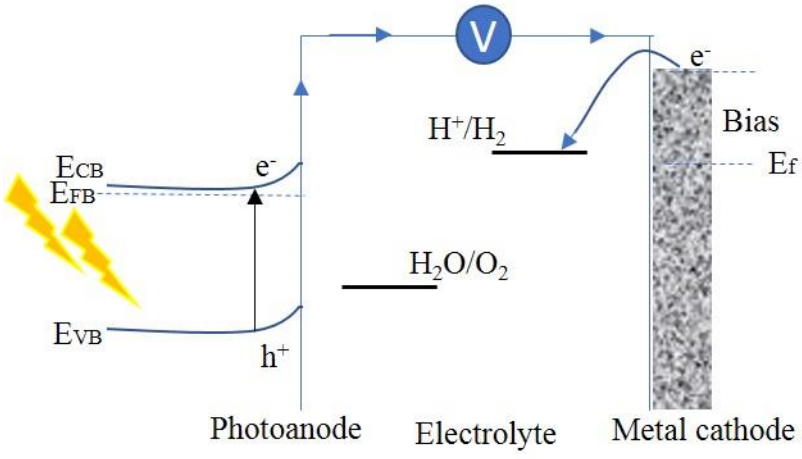

Figure 2.4. Schematic of the band model of the photo-electro-chemical cell circuit including a semiconducting photoanode and metallic cathode.

2.2.2 OER catalysts

Recently, there has been a great focus on finding suitable materials that can be used as photo-anodes. Among them, one category of catalysts is molecular catalysts, which are composed mainly of organometallic compounds such as ($[(bpy)_2(H_2O)RuORu(H_2O)(bpy)2]^{4+}$), and other metal (Ir, Fe, Mn, Co)-oxo species. [23-25]. Although these catalysts are inspired by the natural organisms, their short life span due to failure of bridging ligands between the organic components and the metal element, is the major disadvantage of this type of catalysts [23-25].

Rare earth metal oxides such as RuO_2 and IrO_2 have been reported as another type of highly efficient OER catalysts. However, their high cost and scarcity of the precious metals hinder their application on a large scale [26-29]. Recently, transition metal oxides, such as TiO_2, ZnO, MnO_x, Fe_2O_3, Co_3O_4, NiO_x, Cu_2O have gained significant attention due to their relatively low cost and good catalytic activity [14, 30-33]. Among them, transition-metal-based hydroxide catalysts have been considered more thermodynamically favourable compared to crystalline

oxides, due to their ability to form layered atomic structures by coordination of hydroxide ions with divalent and trivalent metal cations [34-35]. Non-traditional carbon-based materials, dichalcogenide materials and phosphate materials are also reported as OER catalysts [36-39].

Although a variety of materials with varying performances have been reported as OER catalysts, significant insights into the structure of natural OEC have led to increased research in mimicking the structure and composition of natural OEC [2, 40-44]. For developing an artificial system with efficiency close to the natural photosynthesis, in-depth knowledge about the oxygen evolution mechanism of natural OEC is critical. Although several potential models have been proposed, the exact mechanism is still not fully understood. A computational study showed that two water molecules bound to calcium and the fourth manganese ion plays a key role in the water-splitting process [45] and that the three other manganese in the cube act as hole donors to the fourth manganese. In this regard, it is speculated that the atomic arrangement of the Mn_4Ca cubane in PSII is critical to the natural water splitting process [45].

2.3 Structure of natural Mn_4CaO_5 cluster

The investigation of the structure of natural $CaMn_4O_5$ cluster is relatively new. In 2000, Nield *et al*. studied the structure of active PSII protein complex at 15–30 Å resolution [46]. In 2004, the research group of Iwata reported the structure of PSII protein at a higher resolution of 3.5 Å and provided detailed information about the position of most of the protein subunits [47]. The most important aspect of their studies was the inclusion of calcium in the structure. There were several other studies published on the structures of cyanobacterial PSII with a resolution of 3.8-2.9 Å [48-52]. These high resolutions studies provided detailed information on the arrangement of protein's structural units and chlorophylls' location. However, the

studies did not provide enough details on the structure of the water oxidising cluster, the key catalyst used for light-induced water oxidation in natural photosynthesis.

The most advanced investigation of OEC was reported in 2011 by Umena *et al*. [3]. They resolved the structure of PSII crystals of thermophilic cyanobacterium *T. vulcanus* at 1.9 Å resolution [3]. It revealed that OEC consists of one calcium, four manganese and five oxygen atoms. It also identified the location of water substrate molecules associated with the $CaMn_4O_5$ cluster, consequently determining the formula $CaMn_4O_5(H_2O)_4$ for the inorganic core of PSII protein [53]. They reported an asymmetrical cubane-like structure, which resembles a distorted chair, where the calcium and three manganese ions formed four corners and remaining four corners were occupied by four oxygen atoms (Figure 2.5a). Fourth manganese ion was reported to be outside the cubane which was linked to two manganese ions within the cubane by one oxygen, and the fifth oxygen by a di-μ-oxo bridge [3]. With regards to the position of water molecules, two of them were coordinated to the fourth manganese atom outside the cubane and remaining two were coordinated to the calcium atom (Figure 2.5b). The studies also determined the distances between individual atoms and water molecules (Figures 2.5c, 2.5d) [3]. To date, this result remains the highest resolved structure of inorganic core of PSII.

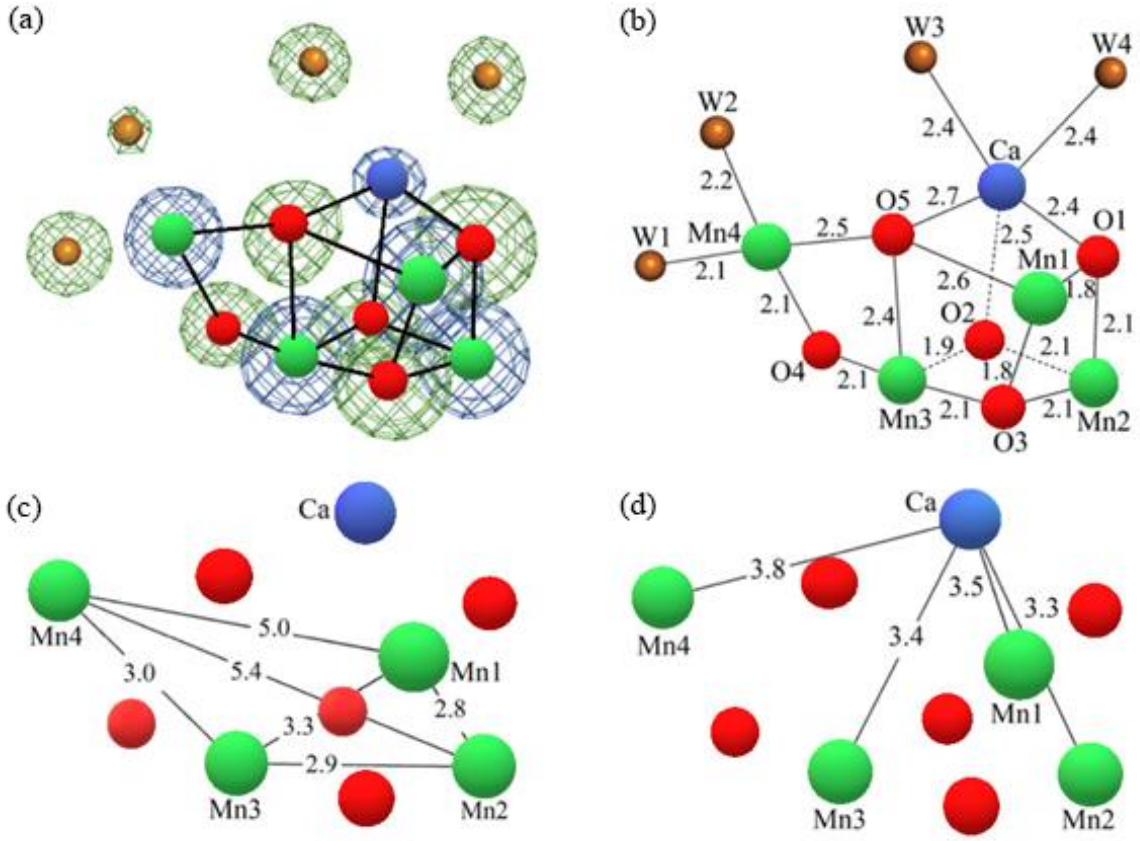

Figure 2.5. Structure of $CaMn_4O_5$ cluster in Photosystem II protein. Calcium in blue; manganese in green; oxygen in red.

2.4 Biomimetic catalysts for OER

2.4.1 Crystal structure

Due to their similar elemental composition to the natural OEC cubane, calcium manganese oxide ceramics have emerged as potential biomimetic catalysts [2,40-44]. Among different calcium manganese oxides, $CaMn_2O_4$ [43], $Ca_2Mn_3O_8$ [41] and $CaMn_3O_6$ [2] were found to have their sub-structure similar to that of natural OEC. Detailed analysis of X-ray absorption spectroscopy data revealed that, in these compounds, not only the shapes of local atomic

arrangements are cubane-like, but also the distances between atoms are similar to those of the natural $CaMn_4O_5$ cubane [2, 40]. These are described more in detail in the following paragraphs.

The structure of $CaMn_2O_4$ has manganese layers containing calcium between them (Figure 2.6a). In this structure, there are edge-sharing MnO_6 octahedral dimers with eight-coordinate calcium-centred polyhedrals, and also Mn_2O_{10}, which is the edge-sharing di-octahedra that vertex-shares to another Mn_2O_{10} di-octahedra. These make the local atomic arrangement similar to that of OEC (Figure 2.6b) [54].

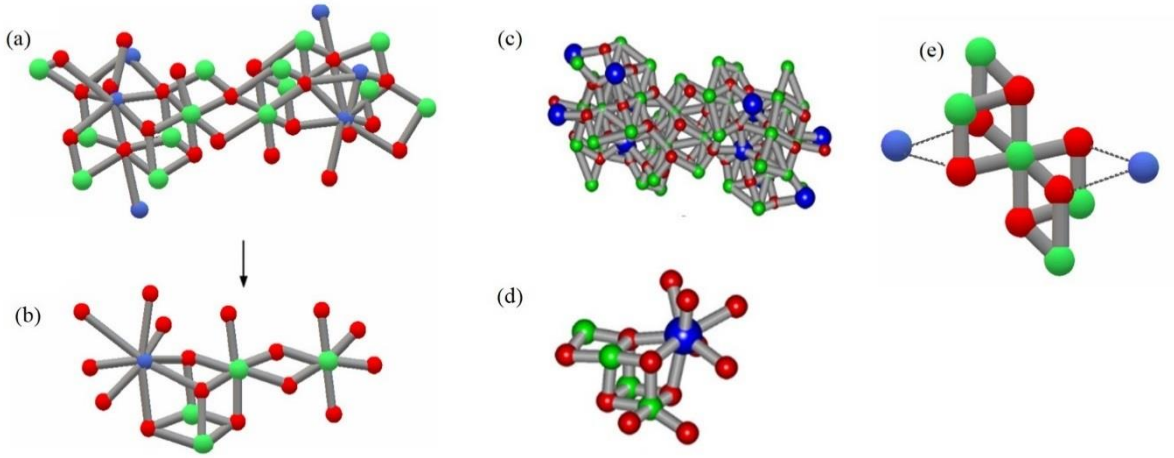

Figure 2.6. (a) Structure of $CaMn_2O_4$ and (b) the structure contains $CaMn_4O_x$ sub-units similar to that found in the oxygen evolving complex in photosystem II. Adapted from Ref. [43] with permission from Springer Nature. (c) Crystal structure of $CaMn_3O_6$ and (d) a cubane local atomic arrangement in $CaMn_3O_6$. Adapted from Ref. [2] with permission from Elsevier. (e) Two half-cubanes local atomic arrangement in the crystal structure of $Ca_2Mn_3O_8$. Adapted from Ref. [41] with permission from Elsevier. Calcium in blue; manganese in green; oxygen in red.

Figures 2.6 (c-d) show the structural similarity between another calcium manganate, $CaMn_3O_6$ and the natural OEC [2]. $CaMn_3O_6$ consists of double chains of edge-sharing MnO_6 octahedra. The corner-sharing chains form a framework with six-sided tunnels, where the Ca^{2+} cations are situated [55].

$Ca_2Mn_3O_8$ consists of sheets of $Mn_3O_8^{4-}$ which are held together by Ca^{2+} atoms (Figure 2.6e) [56]. Mn^{4+} atoms are octahedrally coordinated by oxygen atoms (MnO_6) and form octahedral sheets by sharing the edges [57]. The local atomic arrangement is similar to that of natural OEC cubane except one missing Mn.

Table 2.1 shows that, not only the atomic arrangement but also the atomic distances in the local structures of $CaMn_2O_4$, $Ca_2Mn_3O_8$ and $CaMn_3O_6$ are similar to those of natural Mn_4Ca cubane.

Table 2.1. Atomic distances in the local structures of $CaMn_2O_4$, $Ca_2Mn_3O_8$ ceramic crystals and natural Mn_4Ca cubane (OEC).

Compound	Distance (Å) Mn(1,2,3)-Mn(1,2,3)	Distance (Å) Ca-Mn(1,2,3)	Reference
Natural OEC	2.8-3.3	3.3-3.5	[3]
$Ca_2Mn_3O_8$	2.8-3.1	3.3-3.7	[58]
$CaMn_2O_4$	3.1	3.2	[59]
$CaMn_3O_6$	2.9-3.6	3-3.5	[60]

* Mn1, Mn2 and Mn3 represent the position of manganese ions in Figure 2.1. Accordingly, Mn(1,2,3)-Mn(1,2,3) represents the range of distances between Mn1, Mn2 and Mn3. Ca Mn(1,2,3) represent the range of distances between Ca and Mn1, Mn2 and Mn3.

Figure 2.7 shows the ball and stick model of crystal structure of $CaMnO_3$ [61]. It is evident that $CaMnO_3$ does not show structural similarity to the natural cubane. However, some perovskite-type materials, with ABO_3 type structure in which A is mainly a rare earth or alkaline earth element (Ca, Ba, La and Sr) and B is a transition metal element (Fe, Co, Ni, Mn, Cr), have been reported as good OER and ORR catalyst [62].

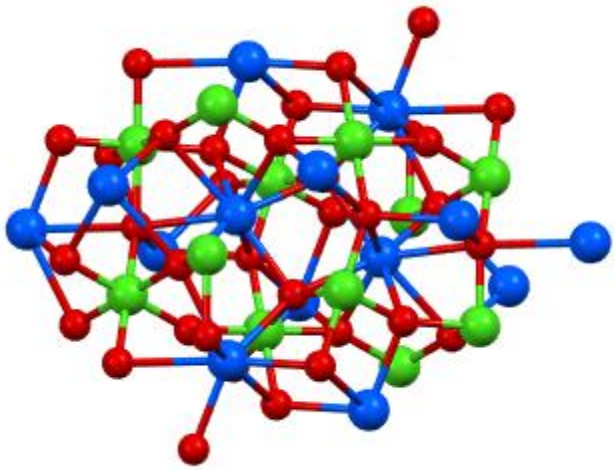

Figure 2.7. Structure of $CaMnO_3$. Calcium in blue; manganese in green; oxygen in red [61]

2.4.2 Synthesis Methods of Calcium Manganese Oxides

Due to their elemental and structural similarity to the natural OEC, the methods to synthesise calcium manganese oxides have received a great research interest. Various methods have been explored to synthesise different types of Ca-Mn-O systems. The preparation of stoichiometric compounds such as $CaMnO_3$, $CaMn_2O_4$, $Ca_2Mn_3O_8$, $CaMn_4O_8$ and $CaMn_3O_6$, have been a subject of investigation for a long time [55, 63-66]. The synthesis of other types of Ca-Mn-O, including non-stoichiometric [48, 67-68] and amorphous calcium manganese oxides [69] have also been studied recently.

The most conventional route to synthesize calcium manganese oxides is by using high temperature thermal decomposition methods [55, 70-73]. In this methods, calcium and manganese compounds, often nitrates, carbonates, acetates or oxides, are mixed in stoichiometric quantities to obtain solid solution precursors and then heated at temperature above several hundred degrees for several hours. In a recent report, Han *et al*. demonstrated the synthesis of $CaMnO_3$, $Ca_2Mn_3O_8$, $CaMn_2O_4$ and $CaMn_3O_6$ by firing the corresponding $Ca_{1-x}Mn_xCO_3$ (x = 0.5, 0.6, 0.67, and 0.75) solid–solution precursors in alumina boats in air, which resulted in micron sized particles [74]. Similarly, Najafpour *et al*. synthesized $Ca_2Mn_3O_8$ by heating a intimately ground mixture of $CaCO_3$ and $MnCO_3$ and reported spherical shaped particles with a typical diameter of 600 nm [75]. Gil de Muro *et al*. reported the synthesis of calcium manganese oxides by a ceramic method which resulted in grains of 10-30 mm [76]. The calcium manganese oxides synthesised using these methods normally have large particle sizes and low specific surface areas due to the involvement of high temperatures, which is not suitable for catalytic applications where a large surface area is beneficial to improved reaction rates [77].

The sol-gel technique is another common method to synthesize calcium manganese oxides [57, 71, 78-80]. In this method, a gel is often prepared by mixing solutions containing calcium and manganese ions to precipitate calcium manganese compound precursors. Often a binder such as citric acid and ethylene glycol is added to form a gel. The prepared gel is then heated slowly to higher temperatures to decompose the precursors into oxides [81]. This method has advantages in achieving better chemical homogeneity, because it involves mixing of precursors at an atomic level [71]. However, the gelation process induces the aggregation of resulting particles and hence reduces the specific surface areas of particles [82].

A common procedure to prepare Ca-Mn-O compounds at lower temperatures is via hydrothermal synthesis [83]. In this method, calcium and manganese salts are dissolved in water, followed by addition of $KMnO_4$ and a base. The resulting precipitate is transferred to an autoclave and heated at ~200°C for 2-3 days [84]. Ca-Mn-O compounds made using this method were reported to be nanowires with length varying from 100 nm [83] to 10 mm [84]. Solvothermal synthesis using ethanol was also reported [85].

In addition to these conventional methods, new methods are constantly being explored for the synthesis of different shapes of Ca-Mn-O compounds. Nakhowong demonstrated the synthesis of one-dimensional porous $CaMnO_3$ nanofibers using an electrospinning technique. A solution of calcium nitrate, manganese nitrate, and poly acrylonitrile was electrospun and then calcined at 700, 800, and 900 °C [86]. The report claimed the orthorhombic perovskite structure of $CaMnO_3$ with high crystallinity. Average fiber diameters were reduced upon increasing the calcination temperature. Frey *et al*. demonstrated the synthesis of Ca-birnessite with a layered structure [68]. Barrocas *et al*. used a radio-frequency magnetron sputtering method to deposit $CaMn_3O_6$ films on unheated quartz glass substrates using $CaMnO_3$ solid solutions as a sputtering target [87]. The films were reported to be amorphous and therefore, heat treatment in air at 800 °C for 6 h was used to crystallize the film. Baktash *et al*. demonstrated the synthesis of a series of Ca-Mn-O foams using cyanamide, by varying experimental parameters such as cyanamide/metal ratios and temperature [88]. The structures were reported to be highly porous, which increased the catalytic efficiency of the material. The group of Calbet used heat treatment under a reducing environment (H_2 + He gas) to synthesize $CaMnO_2$ from $CaMnO_3$ [89] and $Ca_2Mn_3O_5$ from $Ca_2Mn_3O_8$ [90]. Similarly, Kim *et al*. showed preparation of $Ca_2Mn_2O_5$ by reducing $CaMnO_3$ under H_2 and air [80]. One report showed a method to prepare single crystals of $CaMn_2O_4$ and $CaMn_3O_6$ by heating a mixture of $Na_{0.44}MnO_2$ and $CaCl_2$ powder in high-purity alumina

crucibles in air and washing the resulting product [91]. In this approach, molten $CaCl_2$ was reported to act as a self-flux material during the reaction. Yu *et al*. demonstrated the fabrication of $CaMn_3O_6/CaMn_2O_4$ hetero-structure nanoribbons that exhibit unique physical and chemical properties [92]. They mixed polycrystalline $CaMnO_3$ powders and composite chlorides (molar ratio NaCl : KCl = 1 : 1) in an agate pestle and mortar and then heat treated the powder at various temperatures to obtain nanoribbons with different length. Figure 2.8 depicts the different morphologies of Ca-Mn-O compounds obtained by different synthesis methods.

Several studies have also focused on mimicking the structure of natural OEC in synthetic organometallic compounds [93-99]. Kanady *et al*. reported the synthesis of a $[CaMn_3O_4]^{6+}$ cubane that is structurally similar to a $CaMn_3$ sub-site of the natural OEC [98]. Mukherjee at al. demonstrated the synthesis of $CaMn_3O_4$ cubane consisting of additional metal externally, a model that closely resembled natural OEC, as shown in Figure 2.9 [100]. Although the demonstrated compound was structurally similar to OEC, the external element was reported to be calcium, rendering the different elemental composition of the overall compound than natural OEC.

Zhang *et al*. incorporated the fourth manganese ion in the cubane by synthesizing a metal-organic complex $[Mn_4CaO_4(Bu^tCO_2)_8(Bu^tCO_2H)_2(py)]$, where the asymmetric $CaMn_4O_5$-cluster had similarity to the native OEC in both structure of the metal oxygen complex core and the surrounding proteins [99]. To prepare the complex, first a precursor was obtained by a reaction between $Bu^n_4NMnO_4$ (Bu^n, n-butyl), $Mn(CH_3CO_2)_2{\cdot}(H_2O)_4$, and Ca $(CH_3CO_2)_2{\cdot}H_2O$ in boiling acetonitrile and an excess of pivalic acid, which was then recrystallized in the presence of 2% pyridine in ethyl acetate.

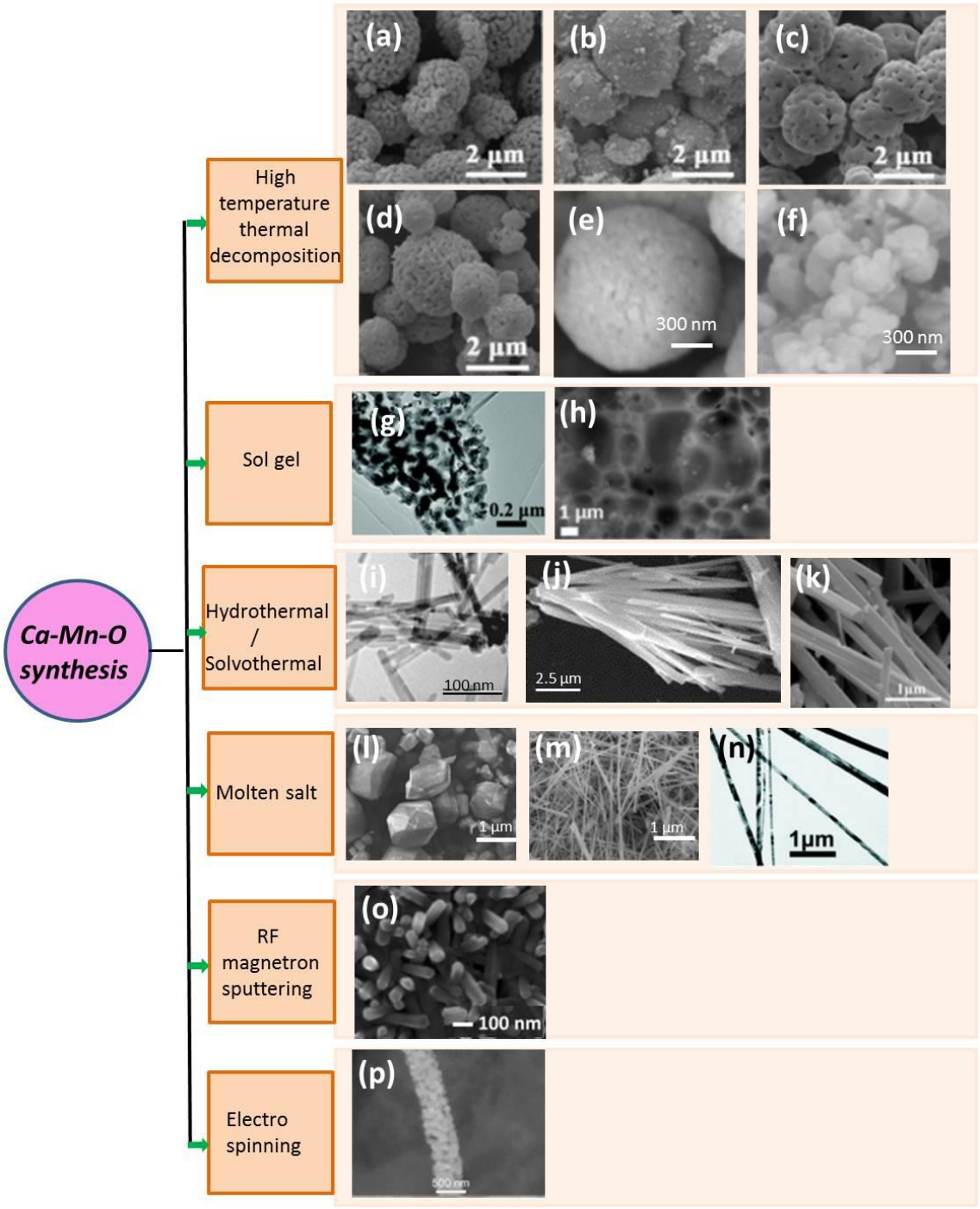

Figure 2.8. Microscopic image of (a) $CaMnO_3$ [74], (b) $Ca_2Mn_3O_8$ [74], (c) $CaMn_2O_4$ [74], (d) $CaMn_3O_6$ [74], (e) $Ca_2Mn_3O_8$ [75], (f) $CaMnO_3$ [75], (g) $CaMnO_3$ [81], (h) $CaMn_2O_x$ [88], (i) $CaMn_2O_4$ nanowires [83], (j) $CaMn_2O_4$ [84], (k) $CaMn_2O_4$ nanorods [85], (l) single crystals of $CaMn_2O_4$ [91], (m) single crystals of $CaMn_3O_6$ [91], (n) $CaMn_3O_6$ / $CaMn_2O_4$ heterostructure nanoribbons [92], (o) $CaMn_3O_6$ nanorods [87], and (p) $CaMnO_3$ nanofibers [86].

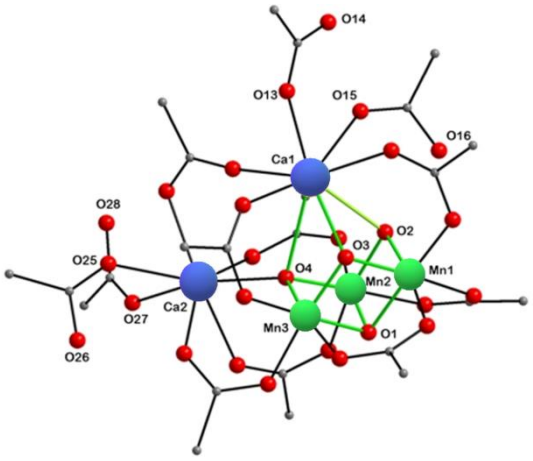

Figure 2.9. The structure of a synthetic organometallic compound that mimics the structure of natural OEC in PSII. Manganese in green; calcium in blue; oxygen in red; carbon in grey. The $CaMn_3O_4$ cubane within the synthetic organometallic compound is emphasized with green bonds. Adapted from Ref. [100] with permission from National Academy of Sciences.

2.4.3 Optical properties of Calcium Manganese Oxides

Optical properties play a significant role in photo-catalysis reactions. The knowledge of absolute band energies or band-edge positions of the catalytic materials is crucial to any photoelectric applications [101]. Although band-edge positions have been theoretically calculated for some of the Ca-Mn-O compounds [102], there is little study reported on the band-edge positions and bandgap energies of various Ca-Mn-O compounds with different Ca to Mn ratios. The bandgap energies of bulk and nanoscale $CaMn_2O_4$ were reported to be about 1.94 eV and 1.4 eV, respectively [103]. The bandgap of $Ca_2Mn_3O_8$ is slightly larger than $CaMn_2O_4$ but still in the visible light range, 2.4 eV [102] to 2.8 eV [41]. The bandgap of $CaMnO_3$, varying between 0.8 [104] eV-1.4 eV [102], is in the visible-light range. These values show that Ca-Mn-O compounds can potentially act as photo-catalysts under natural sunlight.

2.4.4 Photocatalytic Dye Degradation using calcium manganese oxide

Photocatalytic properties of calcium manganese oxides have been studied to degrade organic pollutants (dye) [105] for water purification. For the decomposition of organic pollutants by photo-generation of free radicals, the top of the valence band of catalysts should be more positive than the electrochemical potential of $OH^- + h^+ = OH^*$ free radical generation via the reaction $OH^- + h^+ = OH^*$ (+1.99 V vs NHE at pH =7) [106].

Khanahmadzadeh *et al*. demonstrated almost complete degradation of Rhodamine-B in 120 min in the presence of $CaMn_2O_4$ nanoparticles under visible light [103]. Barrocas *et al*. reported 83.1% degradation of Rhodamine-6G in 4 hours in the presence of $CaMn_3O_6$ nanorods under visible light irradiation, which was only 63.7% in the presence of immobilized TiO_2, demonstrating excellent catalytic performance of calcium manganese oxides [87]. The same group prepared $Ca_{1-x}Ln_xMnO_3$ (Ln = Sm, Ho; $0.1 \leq x \leq 0.4$) and showed that substitution of Ca with Ho was highly effective in degrading Rhodamine-6G [107]. Table 2.2 summarizes the experimental conditions and dye degradation efficiencies using different Ca-Mn-O compounds.

Table 2.2. Dye degradation efficiencies of different Ca-Mn-O compounds.

Compound	Experimental Conditions	Exposure time (h)	% Degradation	Reference
$CaMn_2O_4$	Rhodamine B; visible light irradiation	2	95	[103]
$Ca_{0.8}Ho_{0.2}MnO_3$	Rh6G; mercury vapor lamp (450 W, 0.37 W/cm^2); visible light irradiation(>400nm)	4	97.5	[107]

Table 2.2. (continued).

$Ca_{0.8}Sm_{0.2}MnO_3$	Rh6G; mercury vapor lamp (450 W, 0.37 W/cm^2); visible light irradiation(>400nm)	4	76.3	[107]
$CaMn_3O_6$	Rh6G; mercury vapor lamp (450 W, 0.37 W/cm^2); visible light irradiation(>400nm)	4	83.1	[87]
TiO_2	Rh6G; mercury vapor lamp (450 W, 0.37 W/cm^2); visible light irradiation(>400nm)	4	63.7	[87]

2.4.5 Water oxidation by calcium manganese oxides

Photocatalytic water splitting by calcium manganese oxides, inspired by the natural calcium manganese cluster, has been a subject of recent research activities. Despite their structural and compositional similarity to natural OEC, only a small number of published studies have addressed the oxygen evolution properties $CaMn_xO_y$ compounds by water-splitting to date [49, 52, 75, 108]. Table 2.3 summarizes the rate of water oxidation by different calcium manganese oxides catalysts.

Table 2.3. Catalytic water oxidation efficiency (Turn-over frequency, TOF) of calcium manganese oxide materials in the presence of sacrificial oxidants.

Compound	Oxidant	Rate of catalysis (TOF) ($mmol_{O2} \cdot mol^{-1}_{Mn}) \cdot s^{-1}$	Specific surface area ($m^2 g^{-1}$)	Experimental Conditions	Ref.
$CaMn_2O_4 \cdot H_2O$	H_2O_2 HSO_5 Ce^{IV} Ru^{III}_{photo}	4.2 0.25 0.54 0.35	205	Catalyst particles suspended in water; (for Ru^{III}_{photo} λ> 400 nm and light intensity ~26500 lux.)	[44]
$CaMn_2O_4.H_2O$	Ce^{IV}	2.0	n.a. (nanoparticle)	Catalyst particles suspended in water	[69]
$CaMn_2O_4.4H_2O$	H_2O_2 HSO_5 Ce^{IV} Ru^{III}	>5.0 0.325 0.325 0.325	303	Catalyst particles suspended in water; (for Ru^{III}_{photo} λ> 400 nm and light intensity ~26500 lux.	[44]
$CaMn_2O_4$	H_2O_2 HSO_5 Ce^{IV} Ru^{III}	0.9 0.024 traces 0.012	2.62	Catalyst particles suspended in water; (for Ru^{III}_{photo} λ> 400 nm and light intensity ~26500 lux.)	[44]
$CaMn_3O_6$	H_2O_2 HSO_5 Ce^{IV} Ru^{III}	>0.2 0.006 0.046 0.002	2.53	Catalyst particles suspended in water; (for Ru^{III}_{photo} λ> 400 nm and light intensity ~10000 lux.)	[75]
$Ca_2Mn_3O_8$	Ce^{IV}	0.016	3.47	Catalyst particles suspended in water	[75]
$CaMn_4O_8$	H_2O_2 HSO_5 Ce^{IV} Ru^{III}	>0.2 0.006 0.035 0.0004	2.66	Catalyst particles suspended in water; (for Ru^{III}_{photo} λ> 400 nm and light intensity ~10000 lux.)	[75]
$CaMnO_3$	Ce^{IV}	0.012	2.54	Catalyst particles suspended in water	[75]

Table 2.3. (continued).

$CaMn_2O_x$	Ce^{IV}	0.011- 0.62	0.2-130	Catalyst particles suspended in water	[88]
K_p-$Ca_xMn_yO_z$	Ce^{IV}	0.006-0.83	1-275	Catalyst particles suspended in water	[68]
Ca_xMnO_y	Ce^{IV}	0.19-0.88	90-221	Catalyst particles suspended in water	[77]
Photosystem II [a]	Sunlight	25000			[69]

[a] based on a rate of 100 O_2 per second and PSII in full sunlight and 4 Mn per OEC.

From Table 2.3, it is evident that the catalytic efficiency or turn-over frequency (TOF) of artificial water splitting is very small compared to the natural system. In addition, a majority of the oxygen evolution experiments using calcium manganese oxides were performed by dispersing the catalyst in a solution in the presence of sacrificial chemical oxidants. Although some reports have described the electro-catalytic oxygen evolution performance of calcium manganese oxide compounds as immobilized particles on electrodes [41, 74, 80, 85, 109-113], applications of calcium manganese oxide as photo-electrodes have not been investigated.

2.5 Importance of Calcium

For developing an effective biomimetic photo-catalyst, it is important to understand the role of calcium in the natural OEC system. In the early investigation of the mechanisms of oxygen evolution by the OEC in PSII, only manganese was discussed as an active element and the role of calcium was neglected [114]. However, recent research supports that calcium plays an important role in the natural photosynthesis process [115-116]. Several ideas about the role of calcium have been proposed, including nucleophilic attack on terminal Mn(V)═O by a Ca^{2+} bound hydroxide ligand [117], and formation of the O─O bond through a nucleophilic attack

on Mn(V)═O species by calcium bound water [118]. Some reports have also demonstrated that calcium provides structural stability in the OEC cluster [115-116].

The role of calcium is not only unclear in the natural photo catalytic system but also in photo-induced water splitting by calcium-manganate ceramics. It has been observed that, compared to MnO_2 which has well-recognised water oxidation ability [119], $CaMnO_3$, $Ca_2Mn_3O_8$ and $CaMn_2O_4$ have higher water-oxidation efficiencies, even without light irradiation [120]. Wiechen *et al*. reported that, when calcium is replaced by other alkali earth metals (Sr, Mg), their water-oxidation activity decreased [67]. Thus, Najafpour and Kurz suggested the importance of calcium in the water-oxidation reaction [44]. Some reports highlighted the importance of calcium in stabilizing the high valence states of manganese, at high temperatures, in calcium-manganese oxides [75]. Elucidating the catalytic role of calcium in calcium-manganate ceramics is important, not only for optimising their water-oxidation activities but also for advancing our understanding of the mechanism of natural photosynthesis. For this, it is important to comparatively study the performance of manganese oxides and calcium manganese oxides in the artificial water oxidation system.

2.6 Manganese oxide-based OEC

Manganese oxides are an interesting class of compounds due to their ability to take various oxidation states (+2, +3, +4 being the most common ones) and various crystal structures. For most manganese oxides, their basic building block is MnO_6 octahedral units, which can be arranged in various structural assemblies by either sharing edges and / or corners. This gives rise to two major structural types: (a) chain, or tunnel, structures and (b) layer structures, as shown in Figure 2.10. [119]. These structures play an important role in allowing intercalation

of cations during catalytic reactions. Therefore, it is proposed that the catalytic activity of manganese oxides is strongly influenced by the crystal structure [121].

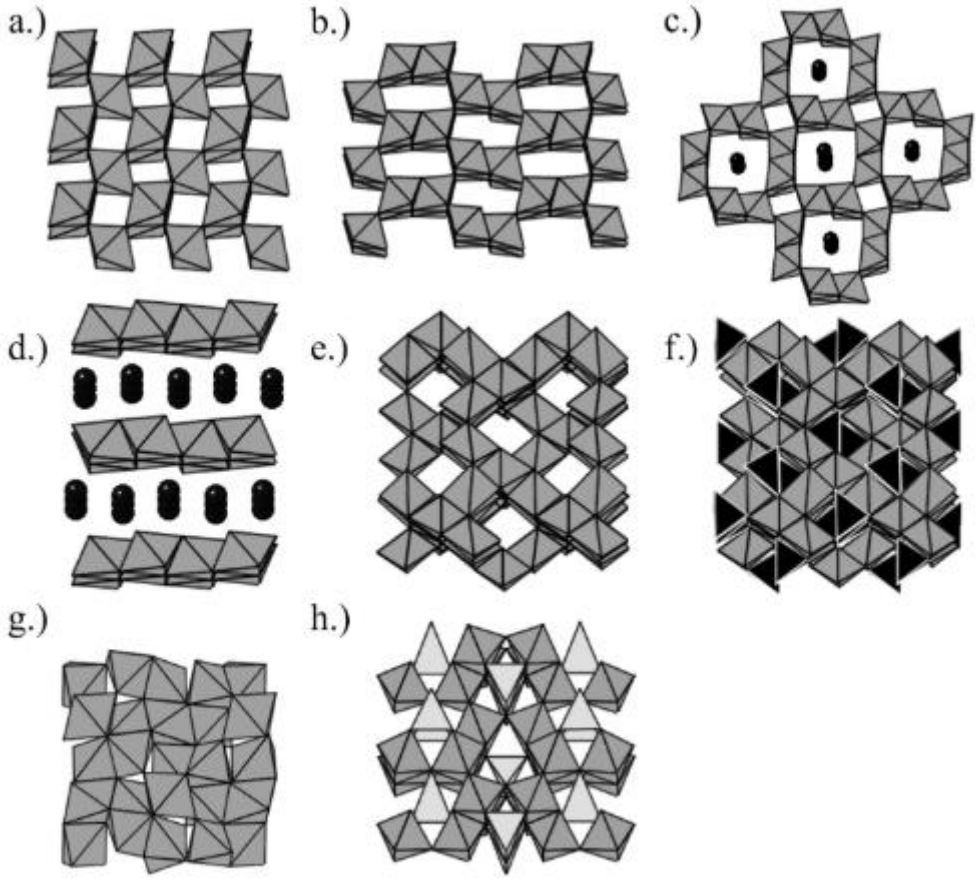

Figure 2.10. Polyhedral representation of the eight Mn oxides reported herein: (a) β-MnO_2, (b) R-MnO_2, (c) α-MnO_2, (d) δ-MnO_2, (e) λ-MnO_2, (f) $LiMn_2O_4$, (g) Mn_2O_3, and (h) Mn_3O_4. The light, dark, and black polyhedra represent Mn^{2+} tetrahedra, Mn^{3+} and Mn^{4+} octahedra, and Li^{1+} tetrahedra, respectively. Black spheres represent K^+ ions. Reprinted with permission from Ref [119]. Copyright (2013) American Chemical Society.

Although much research has been conducted on the catalytic properties of manganese oxides for water oxidation, the reported data are rather inconclusive. Several groups have demonstrated that various structures of MnO_2 act as efficient water oxidation catalysts [122-

127]. Boppana *et al.* demonstrated that α-MnO_2 nanowires showed higher photocatalytic activity than α-MnO_2 nanotubes followed by β-MnO_2 nanowire in strong acidic conditions, but the influence of crystal structure and morphology of MnO_2 on their photocatalytic activity was weak [122]. Excellent electrocatalytic water oxidation ability of β-MnO_2 was demonstrated by Fekete *et al*. at both neutral and high pH [124]. δ-MnO_2 (birnessite-type layered structure manganese dioxide) has been shown as an effective water oxidation catalyst by both, theoretical DFT (density functional theory) studies [125] and experimental work [67,126-127]. On the contrary, Robinson *et al.* found that β-MnO_2, γ-MnO_2, α-MnO_2, δ-MnO_2 and $LiMn_2O_4$ showed no OER activity in the photochemical water oxidation system [119]. They reported that Mn_2O_3 showed the highest OER activity followed by Mn_3O_4 [119]. Smith *et al*. found similar results with lowest water oxidation of MnO_2 among different tested samples and higher activities with Mn^{3+} in corner-sharing sites as catalytic centers for water oxidation [128]. Higher catalytic activity of Mn_2O_3 was also supported by the studies of Ramirez *et al*. [129]. Frey *et al*. found that, although Mn_2O_3 showed higher water oxidation ability than MnO_2, amorphous birnessite type manganese oxides were the best performing samples [130]. Amorphous manganese oxides also demonstrated significantly higher turnovers compared to tunnel structure and layered structure in water oxidation tests with Ce^{4+} in a study by Iyer *et al*. [131].

From the above discussion, it is clear that past investigations present uncertain results regarding the water oxidation abilities of manganese oxides. Since the data reported in various literatures were obtained under different experimental conditions, it could be understood that the water oxidation abilities are dependent on test conditions, as suggested by Pokhrel *et al.* [132]. They analysed nine crystalline MnO_x materials (α-MnO_2, β-MnO_2, R-MnO_2, λ-MnO_2, δ-MnO_2, γ-MnO_2, Mn_2O_3, Mn_3O_4, $LiMn_2O_4$) by chemical, photochemical and electrochemical assays, and reported that the identity of the "best" catalysis is dependent on the oxidation method used.

Their results showed that γ-MnO_2 performed the best in a ceric ammonium nitrate solution of pH 0.8 (a chemical oxidant method), Mn_2O_3 showed highest water oxidation during photochemical assay (pH 8) and the best catalysts was dependent on pH of the electrolyte used in electrochemical testing which was Mn_2O_3 (for acidic electrolyte), γ-MnO_2 (for neutral pH electrolyte) and α-MnO_2 (for alkaline electrolyte) [132]. Thus, it could be concluded that, although significant work has been undertaken to investigate the best crystal structure and valance state of manganese oxides as water oxidation catalysts, their water oxidation abilities are not clearly understood and are thought to be influenced by several external factors.

In this regard, the understanding about manganese oxidation states in natural water oxidizing system is of fundamental importance and has potential to provide important insights to the OER of manganese-based ceramic catalysts. Often in literature, two schemes, the low [133-134] and high [135-137] oxidation state schemes, of manganese within the natural catalytic cycle are reported. Mostly, experimental data from X-ray absorption near edge structure (XANES) spectra support the high valent oxidation scheme [138-142], although one study reinterpreted the data to be in better agreement with the low valent scheme [143]. The difference in opinion could be argued from the point that the XANES spectral shape depends on ligand and coordination environment, which results in ambiguities over determination of the edge position and subsequent interpretations [144]. To investigate the correct oxidation state, Krewald *et al*. studied a detailed computational comparison of the two schemes [144]. Their studies demonstrated that only the high-valent scheme leads to a formulation of the catalytic cycle that is consistent with spectroscopic observations and catalytic state progression. Thus, it is assumed that manganese with higher oxidation states could be a better choice for catalytic water splitting.

2.7 Chapter summary and gaps in knowledge

The idea of biological water splitting in the natural system has inspired researchers to produce hydrogen fuel by splitting water using sunlight, an abundant, renewable and carbon-neutral energy source. In order to realize efficient and practical 'artificial photosynthesis', photo-electrocatalytic water splitting is a permission approach to overcome challenges the conventional approaches face. However, the approach requires the use of OER catalysts that has high efficiency under natural sunlight and the ambient conditions. Recent research into the natural photosynthesis revealed that $CaMn_4O_5$ cluster with a cubane structure is the key catalyst to split water in plant cells. Inspired by this recent development in the understanding of this natural OEC, calcium manganese oxides have attracted great interest as a new class of catalysts in many energy-related applications in recent years.

To investigate the catalytic applications of Ca-Mn-O systems in the energy and environmental sectors, different synthesis methods with varying Ca-Mn ratios and morphologies have been explored. It was found that, in addition to the structural similarity to the natural water splitting catalyst, Ca-Mn-O catalysts have the following advantages over other photocatalysts: (1) optical bandgap energies are in the visible light range, allowing utilisation of a wider solar spectrum than TiO_2 and other wide-bandgap semiconductor photocatalysts where only a small portion of solar energy can be used; (2) they are made of earth-abundant non-toxic elements, rendering the material attractive from sustainability point of view; (3) they have high chemical stability in water, enabling the construction of durable devices for practical use.

However, the literature review identified that the investigation into the photocatalysis of calcium manganese oxides is in its infancy and that there still exist the following fundamental knowledge gaps:

1) Although studies have been conducted on the redox catalytic activities of calcium manganese oxides in the past, we are critically lacking the knowledge about *photo-induced* catalytic activities of calcium manganese oxides. In addition, green and scalable synthesis techniques of ultrafine calcium manganese oxides have seen little advancement.
2) Band energy positions, which are crucial for predicting a material's suitability for OER catalyst, of the calcium manganese oxide are not well known.
3) Water-splitting photo-electrochemical cells using Ca-Mn-O nano powders have not been optimised in their design. Most of the water splitting studies of calcium manganese oxide involved dispersion of free-standing catalyst particles. Although studies of photo-catalysts in dispersed forms are of significant interest, from a practical perspective it is crucial to study the immobilization of catalysts on conducting electrodes. Although a few reports have studied immobilization of calcium manganese oxide compounds as an anode in electrochemical cells, the studies were conducted without light irradiation. The issues associated with light is critical because, for practical applications, natural sunlight should be the photo- energy source and also, photocatalytic activities depend on the wavelength of irradiated light in the presence of light.
4) Much of the fundamental knowledge are yet to be developed, including structure-performance relationship, the role of calcium and the influence of manganese oxidation states.
5) Effect of size and morphology of the calcium manganese catalyst on photocatalytic properties have not been studied.

2.8 Research questions

Based on the critical literature review, the present work aims to answer if the nanoparticles of calcium manganese oxides and manganese oxides can be synthesised by an economical green method, what are their band gaps and band energy positions, how do they perform as an anode in PEC water splitting set up, how does structural similarity to natural cubane and morphology affect water splitting. The abovementioned knowledge gaps will be addressed by investigating the followings:

1) synthesis of high valence manganese dioxide (amorphous MnO_2 particles and crystalline α-MnO_2 nanowires) by mechanochemical processing, their photocatalytic activity on decolourization of aqueous solution of Rhodamine B, and mechanism of dye degradation through energy band diagrams evaluations.
2) synthesis of different calcium manganese oxides nanoparticles ($Ca_2Mn_3O_8$, $CaMn_2O_4$ and $CaMnO_3$) by mechanochemical processing and subsequent heat treatment, their photocatalytic activity on decolourization of aqueous solution of Rhodamine 6G, and mechanism of dye degradation through energy band diagrams evaluations.
3) photo-electrochemical water oxidation performance of as synthesized manganese oxides and calcium manganese oxides, and theoretical aspects of goodness-of-fit of the crystal structures of synthesized calcium manganese oxides against the natural calcium manganese cluster ($CaMn_4O_5$).
4) influence of morphology (nanowires and particles) and activity of exposed crystal planes on the photo-electrochemical water splitting of hydrothermally and mechanochemically synthesized $CaMn_2O_4$.

2.9 References

1. Xiong, J., Fischer, W.M., Inoue, K., Nakahara, M. and Bauer, C.E., 2000. *Molecular evidence for the early evolution of photosynthesis*. Science, 289, pp.1724-1730.
2. Najafpour, M.M., 2011. *Calcium-manganese oxides as structural and functional models for active site in oxygen evolving complex in photosystem II: lessons from simple model.* Journal of Photochemistry and Photobiology B: Biology, 104, pp.111-117.
3. Umena, Y., Kawakami, K., Shen, J.R. and Kamiya, N., 2011. *Crystal structure of oxygen-evolving photosystem II at a resolution of 1.9 Å*. Nature, 473, p.55-60.
4. Chua, N.H. and Gillham, N.W., 1977. *The sites of synthesis of the principal thylakoid membrane polypeptides in Chlamydomonas reinhardtii*. The Journal of cell biology 74, pp.441-452
5. Debus, R.J., 1992. *The manganese and calcium ions of photosynthetic oxygen evolution*. Biochimica et Biophysica Acta (BBA)-Bioenergetics, 1102, pp.269-352.
6. Debus, R.J., 2001. *Amino acid residues that modulate the properties of tyrosine YZ and the manganese cluster in the water oxidizing complex of photosystem II*. Biochimica et Biophysica Acta (BBA)-Bioenergetics, 1503, pp.164-186.
7. Nixon, P.J., Sarcina, M. and Diner, B.A., 2005. *The D1 and D2 core proteins*. Photosystem II, pp. 71-93.
8. Walter, M.G., Warren, E.L., McKone, J.R., Boettcher, S.W., Mi, Q., Santori, E.A. and Lewis, N.S., 2010. *Solar water splitting cells*. Chemical reviews, 110, pp.6446-6473.
9. Tachibana, Y., Vayssieres, L. and Durrant, J.R., 2012. *Artificial photosynthesis for solar water-splitting*. Nature Photonics, 6, pp.511-518.
10. Gust, D., Moore, T.A. and Moore, A.L., 2012. *Realizing artificial photosynthesis*. Faraday discussions, 155, pp.9-26.
11. Fujishima, A. and Honda, K., 1972. *Electrochemical photolysis of water at a semiconductor electrode*. Nature, 238, pp.37-38.
12. Maeda, K. and Domen, K., 2010. *Photocatalytic water splitting: recent progress and future challenges*. The Journal of Physical Chemistry Letters, 1, pp.2655-2661.
13. Bofill, R., García-Antón, J., Escriche, L. and Sala, X., 2015. *Chemical, electrochemical and photochemical molecular water oxidation catalysts*. Journal of Photochemistry and Photobiology B: Biology, 152, pp.71-81.
14. Wang, J., Cui, W., Liu, Q., Xing, Z., Asiri, A.M. and Sun, X., 2016. *Recent progress in cobalt-based heterogeneous catalysts for electrochemical water splitting*. Advanced materials, 28, pp.215-230.
15. Tian, J., Liu, Q., Asiri, A.M. and Sun, X., 2014. *Self-supported nanoporous cobalt phosphide nanowire arrays: an efficient 3D hydrogen-evolving cathode over the wide range of pH 0–14*. Journal of the American Chemical Society, 136, pp.7587-7590.
16. Lee, Y., Suntivich, J., May, K.J., Perry, E.E. and Shao-Horn, Y., 2012. *Synthesis and activities of rutile IrO_2 and RuO_2 nanoparticles for oxygen evolution in acid and alkaline solutions*. The journal of physical chemistry letters, 3, pp.399-404.
17. Ng, J.W.D., Gorlin, Y., Nordlund, D. and Jaramillo, T.F., 2014. *Nanostructured manganese oxide supported onto particulate glassy carbon as an active and stable oxygen reduction catalyst in alkaline-based fuel cells*. Journal of The Electrochemical Society, 161, pp.D3105-D3112.
18. Roger, I., Shipman, M.A. and Symes, M.D., 2017. *Earth-abundant catalysts for electrochemical and photoelectrochemical water splitting*. Nature Reviews Chemistry, 1, pp.0003.
19. Currao, A., 2007. *Photoelectrochemical water splitting*. CHIMIA International Journal for Chemistry 61, pp.815-819.

20. Ding, C., Qin, W., Wang, N., Liu, G., Wang, Z., Yan, P., Shi, J. and Li, C., 2014. *Solar-to hydrogen efficiency exceeding 2.5% achieved for overall water splitting with an all earth-abundant dual-photoelectrode*. Physical Chemistry Chemical Physics, 16, pp.15608-15614.
21. Bolton, J.R., Strickler, S.J. and Connolly, J.S., 1985. *Limiting and realizable efficiencies of solar photolysis of water*. Nature, 316, pp.495-500.
22. Idris, M.A., Jamal, Z.A.Z., Jamaludin, S.B., Nafarizal, N., Othman, A.K., Sahdan, M.Z., Zakaria, M.P., Ionescu, M. and Nowotny, J., 2014. *Oxide semiconductors for solar to chemical energy conversion: nanotechnology approach*. Ionics, 20, pp.581-592.
23. Andreiadis, E.S., Chavarot-Kerlidou, M., Fontecave, M. and Artero, V., 2011. *Artificial Photosynthesis: From Molecular Catalysts for Light-driven Water Splitting to Photoelectrochemical Cells*. Photochemistry and photobiology, 87, pp.946-964.
24. Blakemore, J.D., Crabtree, R.H. and Brudvig, G.W., 2015. *Molecular catalysts for water oxidation*. Chemical Reviews, 115, pp.12974-13005.
25. Karkas, M.D., Verho, O., Johnston, E.V. and Åkermark, B., 2014. *Artificial photosynthesis: molecular systems for catalytic water oxidation*. Chemical reviews, 114, pp.11863-12001.
26. Gorlin, Y. and Jaramillo, T.F., 2010. *A bifunctional nonprecious metal catalyst for oxygen reduction and water oxidation*. Journal of the American Chemical Society, 132, pp.13612-13614.
27. Mamaca, N., Mayousse, E., Arrii-Clacens, S., Napporn, T.W., Servat, K., Guillet, N. and Kokoh, K.B., 2012. *Electrochemical activity of ruthenium and iridium based catalysts for oxygen evolution reaction*. Applied Catalysis B: Environmental, 111, pp.376-380.
28. Reier, T., Oezaslan, M. and Strasser, P., 2012. *Electrocatalytic oxygen evolution reaction (OER) on Ru, Ir, and Pt catalysts: a comparative study of nanoparticles and bulk materials*. Acs Catalysis, 2, pp.1765-1772.
29. McCrory, C.C., Jung, S., Peters, J.C. and Jaramillo, T.F., 2013. *Benchmarking heterogeneous electrocatalysts for the oxygen evolution reaction*. Journal of the American Chemical Society, 135, pp.16977-16987.
30. Osterloh, F.E., 2013. *Inorganic nanostructures for photoelectrochemical and photocatalytic water splitting*. Chemical Society Reviews, 42, pp.2294-2320.
31. Doyle, R.L., Godwin, I.J., Brandon, M.P. and Lyons, M.E., 2013. *Redox and electrochemical water splitting catalytic properties of hydrated metal oxide modified electrodes*. Physical Chemistry Chemical Physics, 15, pp.13737-13783.
32. Galàn-Mascarós, J.R., 2015. *Water oxidation at electrodes modified with earth-abundant transition-metal catalysts*. ChemElectroChem, 2, pp.37-50.
33. Singh, A. and Spiccia, L., 2013. *Water oxidation catalysts based on abundant 1st row transition metals.* Coordination Chemistry Reviews, 257, pp.2607-2622.
34. Burke, M.S., Enman, L.J., Batchellor, A.S., Zou, S. and Boettcher, S.W., 2015. *Oxygen evolution reaction electrocatalysis on transition metal oxides and (oxy) hydroxides: activity trends and design principles*. Chemistry of Materials, 27, pp.7549-7558.
35. Lu, Z., Qian, L., Tian, Y., Li, Y., Sun, X. and Duan, X., 2016. *Ternary NiFeMn layered double hydroxides as highly-efficient oxygen evolution catalysts*. Chemical Communications, 52, pp.908-911.
36. Wang, F., Shifa, T.A., Zhan, X., Huang, Y., Liu, K., Cheng, Z., Jiang, C. and He, J., 2015. *Recent advances in transition-metal dichalcogenide based nanomaterials for water splitting.* Nanoscale, 7, pp.19764-19788.
37. Zhan, Y., Lu, M., Yang, S., Xu, C., Liu, Z. and Lee, J.Y., 2016. *Activity of Transition-Metal (Manganese, Iron, Cobalt, and Nickel) Phosphates for Oxygen Electrocatalysis in Alkaline Solution*. ChemCatChem, 8, pp.372-379.
38. Lu, X., Yim, W.L., Suryanto, B.H. and Zhao, C., 2015. *Electrocatalytic oxygen evolution at surface-oxidized multiwall carbon nanotubes*. Journal of the American Chemical Society, 137, pp.2901-2907.

39. Cheng, Y., Xu, C., Jia, L., Gale, J.D., Zhang, L., Liu, C., Shen, P.K. and Jiang, S.P., 2015. *Pristine carbon nanotubes as non-metal electrocatalysts for oxygen evolution reaction of water splitting*. Applied Catalysis B: Environmental, 163, pp.96-104.
40. Zaharieva, I., Najafpour, M.M., Wiechen, M., Haumann, M., Kurz, P. and Dau, H., 2011. *Synthetic manganese–calcium oxides mimic the water-oxidizing complex of photosynthesis functionally and structurally*. Energy & Environmental Science, 4, pp.2400-2408.
41. Ramírez, A., Bogdanoff, P., Friedrich, D. and Fiechter, S., 2012. *Synthesis of $Ca_2Mn_3O_8$ films and their electrochemical studies for the oxygen evolution reaction (OER) of water*. Nano Energy, 1, pp.282-289.
42. Najafpour, M.M., Heidari, S., Amini, E., Khatamian, M., Carpentier, R. and Allakhverdiev, S.I., 2014. *Nano-sized layered Mn oxides as promising and biomimetic water oxidizing catalysts for water splitting in artificial photosynthetic systems.* Journal of Photochemistry and Photobiology B: Biology, 133, pp.124-139.
43. Najafpour, M.M., 2011. *Amorphous manganese-calcium oxides as a possible evolutionary origin for the $CaMn_4$ cluster in photosystem II*. Origins of Life and Evolution of Biospheres, 41, pp.237-247.
44. Najafpour, M.M., Ehrenberg, T., Wiechen, M. and Kurz, P., 2010. *Calcium manganese (III) oxides ($CaMn_2O_4 \cdot x\ H_2O$) as biomimetic oxygen-evolving catalysts*. Angewandte Chemie International Edition, 49, pp.2233-2237.
45. Barber, J., 2016. *Mn_4Ca cluster of photosynthetic oxygen-evolving center: structure, function and evolution*. Biochemistry, 55, pp.5901-5906.
46. Nield, J., Kruse, O., Ruprecht, J., da Fonseca, P., Büchel, C. and Barber, J., 2000. *Thre edimensional structure of Chlamydomonas reinhardtii and Synechococcus elongates photosystem II complexes allows for comparison of their oxygen-evolving complex organization*. Journal of Biological Chemistry, 275, pp.27940-27946.
47. Ferreira, K.N., Iverson, T.M., Maghlaoui, K., Barber, J. and Iwata, S., 2004. *Architecture of the photosynthetic oxygen-evolving center*. Science, 303, pp.1831-1838.
48. Zouni, A., Witt, H.T., Kern, J., Fromme, P., Krauss, N., Saenger, W. and Orth, P., 2001. *Crystal structure of photosystem II from Synechococcus elongatus at 3.8 Å resolution*. Nature, 409, pp.739-743.
49. Kamiya, N. and Shen, J.R., 2003. *Crystal structure of oxygen-evolving photosystem II from Thermosynechococcus vulcanus at 3.7-Å resolution*. Proceedings of the National Academy of Sciences, 100, pp.98-103.
50. Biesiadka, J., Loll, B., Kern, J., Irrgang, K.D. and Zouni, A., 2004. *Crystal structure of cyanobacterial photosystem II at 3.2 Å resolution: a closer look at the Mn-cluster*. Physical Chemistry Chemical Physics, 6, pp.4733-4736.
51. Loll, B., Kern, J., Saenger, W., Zouni, A. and Biesiadka, J., 2005. *Towards complete cofactor arrangement in the 3.0 Å resolution structure of photosystem II*. Nature, 438, pp.1040-1044.
52. Guskov, A., Kern, J., Gabdulkhakov, A., Broser, M., Zouni, A. and Saenger, W., 2009. *Cyanobacterial photosystem II at 2.9-Å resolution and the role of quinones, lipids, channels and chloride*. Nature structural & molecular biology, 16, pp.334-342.
53. Kawakami, K., Umena, Y., Kamiya, N. and Shen, J.R., 2011. *Structure of the catalytic, inorganic core of oxygen-evolving photosystem II at 1.9 Å resolution*. Journal of Photochemistry and Photobiology B: Biology, 104, pp.9-18.
54. Giesber, H.G., Pennington, W.T. and Kolis, J.W., 2001. *Redetermination of $CaMn_2O_4$.* Acta Crystallographica Section C: Crystal Structure Communications, 57, pp.329-330.
55. Hadermann, J., Abakumov, A.M., Gillie, L.J., Martin, C. and Hervieu, M., 2006. *Coupled cation and charge ordering in the $CaMn_3O_6$ tunnel structure*. Chemistry of materials, 18, pp.5530-5536.
56. Ansell, G.B., Modrick, M.A., Longo, J.M., Poeppeimeler, K.R. and Horowitz, H.S., 1982. *Structure of calcium manganese oxide $Ca_2Mn_3O_8$.* Acta Crystallographica Section B: Structural Crystallography and Crystal Chemistry, 38, pp.1795-1797.

57. Park, Y.J. and Doeff, M.M., 2006. *Synthesis and electrochemical characterization of $M_2Mn_3O_8$ (M= Ca, Cu) compounds and derivatives*. Solid State Ionics, 177, pp.893-900.
58. Persson, K., 2016. *Materials Data on $Ca_2Mn_3O_8$ (SG:12) by Materials Project*, viewed 20 July 2017.
59. Persson, K., 2014. *Materials Data on $CaMn_2O_4$ (SG:160) by Materials Project*, viewed 20 July 2017.
60. Persson, K., 2016. *Materials Data on $CaMn_3O_6$ (SG:14) by Materials Project*, viewed 20 July 2017.
61. Persson, K., 2014. *Materials Data on $CaMnO_3$ (SG:62) by Materials Project*, viewed 20 July 2017.
62. Gupta, S., Kellogg, W., Xu, H., Liu, X., Cho, J. and Wu, G., 2016. *Bifunctional perovskite oxide catalysts for oxygen reduction and evolution in alkaline media.* Chemistry–An Asian Journal, 11, pp.10-21.
63. White, T.R., Glaunsinger, W.S., Horowitz, H.S. and Longo, J.M., 1979. *Magnetic properties of the layered compounds $Ca_2Mn_3O_8$ and $Cd_2Mn_3O_8$.* Journal of Solid State Chemistry, 29, pp.205-214.
64. Glaunsinger, W.S., Horowitz, H.S., Longo, J.M. and Chang, A., 1980. *Magnetic properties of the mixed-valence compounds $CaMn_3O_6$ and $CaMn_4O_8$.* Journal of Solid State Chemistry, 35, pp.187-191.
65. Ling, C.D., Neumeier, J.J. and Argyriou, D.N., 2001. *Observation of antiferromagnetism in Marokite $CaMn_2O_4$.* Journal of Solid State Chemistry, 160, pp.167-173.
66. Zhang, F.P., Zhang, X., Lu, Q.M., Zhang, J.X., Liu, Y.Q., Fan, R.F. and Zhang, G.Z., 2011. *Doping induced electronic structure and estimated thermoelectric properties of $CaMnO_3$ system.* Physica B: Condensed Matter, 406, pp.1258-1262.
67. Wiechen, M., Zaharieva, I., Dau, H. and Kurz, P., 2012. *Layered manganese oxides for water oxidation: alkaline earth cations influence catalytic activity in a photosystem II-like fashion.* Chemical Science, 3, pp.2330-2339.
68. Frey, C.E., Wiechen, M. and Kurz, P., 2014. *Water-oxidation catalysis by synthetic manganese oxides–systematic variations of the calcium birnessite theme*. Dalton Transactions, 43, pp.4370-4379.
69. Najafpour, M.M., Nayeri, S. and Pashaei, B., 2011. *Nano-size amorphous calcium–manganese oxide as an efficient and biomimetic water oxidizing catalyst for artificial photosynthesis: back to manganese.* Dalton Transactions, 40, pp.9374-9378.
70. Horowitz, H.S. and Longo, J.M., 1978. *Phase relations in the Ca-Mn-O system*. Materials Research Bulletin, 13, pp.1359-1369.
71. Jorge, M.M., dos Santos, A.C. and Nunes, M.R., 2001. *Effects of synthesis method on stoichiometry, structure and electrical conductivity of $CaMnO_{3-\delta}$.* International Journal of Inorganic Materials, 3, pp.915-921.
72. White, B.D., Dos Santos, C.A.M., Souza, J.A., McClellan, K.J. and Neumeier, J.J., 2008. *Crystal growth and characterization of Marokite $CaMn_2O_{4+\delta}$.* Journal of Crystal Growth, 310, pp.3325-3330.
73. White, B.D., Souza, J.A., Chiorescu, C., Neumeier, J.J. and Cohn, J.L., 2009. *Magnetic transport, and thermodynamic properties of $CaMn_2O_4$ single crystals.* Physical Review B, 79, pp.104427-104435.
74. Han, X., Zhang, T., Du, J., Cheng, F. and Chen, J., 2013. *Porous calcium–manganese oxide microspheres for electrocatalytic oxygen reduction with high activity*. Chemical Science, 4, pp.368-376.
75. Najafpour, M.M., Pashaei, B. and Nayeri, S., 2012. *Calcium manganese (IV) oxides: biomimetic and efficient catalysts for water oxidation*. Dalton Transactions, 41, pp.4799-4805.
76. de Muro, I.G., Insausti, M., Lezama, L. and Rojo, T., 2005. *Morphological and magnetic study of $CaMnO_{3-x}$ oxides obtained from different routes.* Journal of Solid State Chemistry, 178, pp.928-936.

77. Rong, F., Zhao, J., Chen, Z., Xu, Y., Zhao, Y., Yang, Q. and Li, C., 2016. *Highly active water oxidation on nanostructured biomimetic calcium manganese oxide catalysts*. Journal of Materials Chemistry A, 4, pp.6585-6594.
78. Zeng, Z., Greenblatt, M. and Croft, M., 1999. *Large magnetoresistance in antiferromagnetic $CaMnO_{3-\delta}$*. Physical Review B, 59, pp.8784-8788.
79. Liu, X.J., Li, Z.Q., Wu, P., Bai, H.L. and Jiang, E.Y., 2007. *The effect of Fe doping on structural, magnetic and electrical transport properties of $CaMn_{1-x}Fe_xO_3$ (x= 0–0.35)*. Solid state communications, 142, pp.525-530.
80. Kim, J., Yin, X., Tsao, K.C., Fang, S. and Yang, H., 2014. *$Ca_2Mn_2O_5$ as oxygen-deficient perovskite electrocatalyst for oxygen evolution reaction*. Journal of the American Chemical Society, 136, pp.14646-14649.
81. Han, X., Hu, Y., Yang, J., Cheng, F. and Chen, J., 2014. *Porous perovskite $CaMnO_3$ as an electrocatalyst for rechargeable Li–O_2 batteries*. Chemical Communications, 50, pp.1497-1499.
82. Wang, Z., Nie, J., Qin, W., Hu, Q. and Tang, B.Z., 2016. *Gelation process visualized by aggregation-induced emission fluorogens*. Nature communications, 7, pp.12033.
83. Arnold, D.C., Kazakova, O., Audoit, G., Tobin, J.M., Kulkarni, J.S., Nikitenko, S., Morris, M.A. and Holmes, J.D., 2007. *The synthesis and characterisation of ferromagnetic $CaMn_2O_4$ nanowires*. ChemPhysChem, 8, pp.1694-1700.
84. Spooren, J. and Walton, R.I., 2005. *Hydrothermal synthesis of the perovskite manganites $Pr_{0.5}Sr_{0.5}MnO_3$ and $Nd_{0.5}Sr_{0.5}MnO_3$ and alkali-earth manganese oxides $CaMn_2O_4$, 4H-$SrMnO_3$, and 2H-$BaMnO_3$*. Journal of Solid State Chemistry, 178, pp.1683-1691.
85. Du, J., Pan, Y., Zhang, T., Han, X., Cheng, F. and Chen, J., 2012. *Facile solvothermal synthesis of $CaMn_2O_4$ nanorods for electrochemical oxygen reduction*. Journal of Materials Chemistry, 22, pp.15812-15818.
86. Nakhowong, R., 2016. *Preparation and characterization of calcium manganese oxide ($CaMnO_3$) nanofibers by electrospinning.* Materials Letters, 163, pp.222-225.
87. Barrocas, B., Sério, S. and Melo Jorge, M.E., 2014. *Hierarchically grown $CaMn_3O_6$ nanorods by RF magnetron sputtering for enhanced visible-light-driven photocatalysis*. The Journal of Physical Chemistry C, 118, pp.24127-24135.
88. Baktash, E., Zaharieva, I., Schröder, M., Goebel, C., Dau, H. and Thomas, A., 2013. *Cyanamide route to calcium–manganese oxide foams for water oxidation*. Dalton Transactions, 42, pp.16920-16929.
89. Varela, A., Dios, S.D., Parras, M., Hernando, M., Fernández-Díaz, M.T., Landa-Cánovas, A.R. and González-Calbet, J.M., 2009. *Ordered rock-salt related nanoclusters in $CaMnO_2$.* Journal of the American Chemical Society, 131, pp.8660-8668.
90. Mazarío-Fernández, A., Torres-Pardo, A., Varela, A., Parras, M., Martínez, J.L., Fernández-Díaz, M.T., Hernando, M. and González-Calbet, J.M., 2017. *Atomically Resolved Short-Range Order at the Nanoscale in the Ca–Mn–O System.* Inorganic chemistry, 56, pp.11753-11761.
91. Fukabori, A., Awaka, J., Takahashi, Y., Kijima, N., Hayakawa, H. and Akimoto, J., 2008. *Single crystal growth of $CaMn_2O_4$ and $CaMn_3O_6$ in molten $CaCl_2$*. Chemistry letters, 37, pp.978-979.
92. Yu, J., Huang, K., Wu, H. and Li, P., 2012. *Synthesis and magnetic properties of manganite multiple heterostructure nanoribbons*. Dalton Transactions, 41, pp.10286-10291.
93. Mishra, A., Wernsdorfer, W., Abboud, K.A. and Christou, G., 2005. *The first high oxidation state manganese–calcium cluster: relevance to the water oxidizing complex of photosynthesis.* Chemical Communications, 1, pp.54-56.
94. Kanady, J.S., Tsui, E.Y., Day, M.W. and Agapie, T., 2011. *A synthetic model of the Mn_3Ca subsite of the oxygen-evolving complex in photosystem II.* Science, 333, pp.733-736.
95. Kotzabasaki, V., Siczek, M., Lis, T. and Milios, C.J., 2011. *The first heterometallic Mn–Ca cluster containing exclusively Mn (III) centers*. Inorganic Chemistry Communications, 14, pp.213-216.

96. Nayak, S., Nayek, H.P., Dehnen, S., Powell, A.K. and Reedijk, J., 2011. *Trigonal propeller-shaped [Mn III 3 M II Na] complexes (M= Mn, Ca): structural and functional models for the dioxygen evolving centre of PSII*. Dalton Transactions, 40, pp.2699-2702.
97. Park, Y.J., Ziller, J.W. and Borovik, A.S., 2011. *The effects of redox-inactive metal ions on the activation of dioxygen: isolation and characterization of a heterobimetallic complex containing a MnIII–(μ-OH)–CaII core*. Journal of the American Chemical Society, 133, pp.9258-9261.
98. Kanady, J.S., Lin, P.H., Carsch, K.M., Nielsen, R.J., Takase, M.K., Goddard III, W.A. and Agapie, T., 2014. *Toward models for the full oxygen-evolving complex of photosystem II by ligand coordination to lower the symmetry of the Mn_3CaO_4 cubane: Demonstration that electronic effects facilitate binding of a fifth metal*. Journal of the American Chemical Society, 136, pp.14373-14376.
99. Zhang, C., Chen, C., Dong, H., Shen, J.R., Dau, H. and Zhao, J., 2015. *A synthetic Mn_4Ca-cluster mimicking the oxygen-evolving center of photosynthesis*. Science, 348, pp.690-693.
100. Mukherjee, S., Stull, J.A., Yano, J., Stamatatos, T.C., Pringouri, K., Stich, T.A., Abboud, K.A., Britt, R.D., Yachandra, V.K. and Christou, G., 2012. *Synthetic model of the asymmetric $[Mn_3CaO_4]$ cubane core of the oxygen-evolving complex of photosystem II*. Proceedings of The National Academy of Sciences, 109, pp.2257-2262.
101. Kudo, A. and Miseki, Y., 2009. *Heterogeneous photocatalyst materials for water splitting.* Chemical Society Reviews, 38, pp.253-278.
102. Shinde, A., Suram, S.K., Yan, Q., Zhou, L., Singh, A.K., Yu, J., Persson, K.A., Neaton, J.B. and Gregoire, J.M., 2017. *Discovery of manganese-based solar fuel photoanodes via integration of electronic structure calculations, pourbaix stability modeling, and high-throughput experiments.* ACS Energy Letters, 2, pp.2307-2312
103. Khanahmadzadeh, S., Mikaeili, N. and Hasanpour, S., 2017. *Facile synthesis of $CaMn_2O_4$ nanoparticles and investigation of photocatalytic activity, optical and magnetic properties and its influence on the thermal stability of polymeric nanocomposite*. Journal of Materials Science: Materials in Electronics, 28, pp.4521-4529.
104. Akpan, U. and Hameed, B., 2009. *Parameters affecting the photocatalytic degradation of dyes using TiO_2-based photocatalysts: a review*. Journal of hazardous Materials, 170, pp.520-529.
105. Raabe, S., Mierwaldt, D., Ciston, J., Uijttewaal, M., Stein, H., Hoffmann, J., Zhu, Y., Blöchl, P. and Jooss, C., 2012. *In situ electrochemical electron microscopy study of oxygen evolution activity of doped manganite perovskites*. Advanced Functional Materials, 22, pp.3378-3388.
106. Gagrani, A. and Tsuzuki, T., 2019. *Calcium manganese oxides as biomimetic catalysts in energy applications: A short review*. Chemical Engineering Science, 194, pp.116-126.
107. Barrocas, B., Sério, S., Rovisco, A., Nunes, Y. and Jorge, M.M., 2016. *Removal of Rhodamine 6G dye contaminant by visible light driven immobilized $Ca_{1-x}Ln_xMnO_3$ (Ln=Sm, Ho; $0.1<x<0.4$) photocatalysts*. Applied Surface Science, 360, pp.798-806.
108. Najafpour, M. M., 2011. *Mixed-valence manganese calcium oxides as efficient catalysts for water oxidation*. Dalton Transactions, 40, pp.3793-3795.
109. Du, J., Zhang, T., Cheng, F., Chu, W., Wu, Z. and Chen, J., 2014. *Nonstoichiometric perovskite $CaMnO_{3-\delta}$ for oxygen electrocatalysis with high activity*. Inorganic Chemistry, 53, pp.9106-9114.
110. Lee, S.Y., González-Flores, D., Ohms, J., Trost, T., Dau, H., Zaharieva, I. and Kurz, P., 2014. *Screen-Printed Calcium–Birnessite Electrodes for Water Oxidation at Neutral pH and an "Electrochemical Harriman Series"*. ChemSusChem, 7, pp.3442-3451.
111. Zahran, Z.N., Mohamed, E.A. and Naruta, Y., 2017. *Electrocatalytic water oxidation at low energy cost by a highly active and robust calcium–manganese oxide thin film sintered on an FTO electrode with ethyl methyl imidazolium triflate ionic liquid*. Journal of Materials Chemistry A, 5, pp.15167-15174.
112. Han, X., Cheng, F., Zhang, T., Yang, J., Hu, Y. and Chen, J., 2014. *Hydrogenated uniform Pt clusters supported on porous $CaMnO_3$ as a bifunctional electrocatalyst for enhanced oxygen reduction and evolution*. Advanced Materials, 26, pp.2047-2051.

113. Hu, Y., Han, X., Zhao, Q., Du, J., Cheng, F. and Chen, J., 2015. *Porous perovskite calcium–manganese oxide microspheres as an efficient catalyst for rechargeable sodium–oxygen batteries*. Journal of Materials Chemistry A, 3, pp.3320-3324.
114. Hoganson, C.W. and Babcock, G.T., 1997. *A metalloradical mechanism for the generation of oxygen from water in photosynthesis*. Science, 277, pp.1953-1956.
115. Yocum, C.F., 2008. *The calcium and chloride requirements of the O_2 evolving complex.* Coordination Chemistry Reviews, 252, pp.296-305.
116. Vrettos, J.S., Stone, D.A. and Brudvig, G.W., 2001. *Quantifying the ion selectivity of the Ca^{2+} site in photosystem II: Evidence for direct involvement of Ca^{2+} in O_2 formation*. Biochemistry, 40, pp.7937-7945.
117. Pecoraro, V.L., Baldwin, M.J., Caudle, M.T., Hsieh, W.Y. and Law, N.A., 1998. *A proposal for water oxidation in photosystem II*. Pure and applied chemistry, 70, pp.925-929.
118. Limburg, J., Szalai, V.A. and Brudvig, G.W., 1999. *A mechanistic and structural model for the formation and reactivity of a MnV [double bond, length half m-dash] O species in photosynthetic water oxidation*. Journal of the Chemical Society, Dalton Transactions, 9, pp.1353-1362.
119. Robinson, D.M., Go, Y.B., Mui, M., Gardner, G., Zhang, Z., Mastrogiovanni, D., Garfunkel, E., Li, J., Greenblatt, M. and Dismukes, G.C., 2013. *Photochemical water oxidation by crystalline polymorphs of manganese oxides: structural requirements for catalysis*. Journal of the American chemical Society, 135, pp.3494-3501.
120. Najafpour, M.M., Rahimi, F., Aro, E.M., Lee, C.H. and Allakhverdiev, S.I., 2012. *Nano-sized manganese oxides as biomimetic catalysts for water oxidation in artificial photosynthesis: a review*. Journal of the Royal Society Interface, 9, pp.2383-2395.
121. Devaraj, S. and Munichandraiah, N., 2008. *Effect of crystallographic structure of MnO_2 on its electrochemical capacitance properties.* The Journal of Physical Chemistry C, 112, pp.4406-4417.
122. Boppana, V.B.R. and Jiao, F., 2011. *Nanostructured MnO_2: an efficient and robust water oxidation catalyst*. Chemical Communications, 47, pp.8973-8975.
123. Chen, S., Zhai, T., Lu, X.H., Zhang, M.Z., Li, Z.Y., Xu, C.W. and Tong, Y., 2012. *Large-area manganese oxide nanorod arrays as efficient electrocatalyst for oxygen evolution reaction*. International journal of hydrogen energy, 37, pp.13350-13354.
124. Fekete, M., Hocking, R.K., Chang, S.L., Italiano, C., Patti, A.F., Arena, F. and Spiccia, L., 2013. *Highly active screen-printed electrocatalysts for water oxidation based on β-manganese oxide*. Energy & Environmental Science, 6, pp.2222-2232.
125. Yang, J., An, H., Zhou, X. and Li, C., 2015. *Water Oxidation mechanism on alkaline-earth-cation containing birnessite-like manganese oxides*. The Journal of Physical Chemistry C, 119, pp.18487-18494.
126. Thenuwara, A.C., Shumlas, S.L., Attanayake, N.H., Cerkez, E.B., McKendry, I.G., Frazer, L., Borguet, E., Kang, Q., Zdilla, M.J., Sun, J. and Strongin, D.R., 2015. *Copper-intercalated birnessite as a water oxidation catalyst*. Langmuir, 31, pp.12807-12813.
127. Lucht, K.P. and Mendoza-Cortes, J.L., 2015. *Birnessite: A layered manganese oxide to capture sunlight for water-splitting catalysis.* The Journal of Physical Chemistry C, 119, pp.22838-22846.
128. Smith, P.F., Deibert, B.J., Kaushik, S., Gardner, G., Hwang, S., Wang, H., Al-Sharab, J.F., Garfunkel, E., Fabris, L., Li, J. and Dismukes, G.C., 2016. *Coordination geometry and oxidation state requirements of corner-sharing MnO_6 octahedra for water oxidation catalysis: An investigation of manganite (γ-MnOOH).* ACS Catalysis, 6, pp.2089-2099.
129. Ramírez, A., Hillebrand, P., Stellmach, D., May, M.M., Bogdanoff, P. and Fiechter, S., 2014. *Evaluation of MnO_x, Mn_2O_3, and Mn_3O_4 electrodeposited films for the oxygen evolution reaction of water*. The Journal of Physical Chemistry C, 118, pp.14073-14081.
130. Frey, C.E. and Kurz, P., 2015. *Water oxidation catalysis by synthetic manganese oxides with different structural motifs: a comparative study*. Chemistry–A European Journal, 21, pp.14958-14968.

131. Iyer, A., Del-Pilar, J., King'ondu, C.K., Kissel, E., Garces, H.F., Huang, H., El-Sawy, A.M., Dutta, P.K. and Suib, S.L., 2012. *Water oxidation catalysis using amorphous manganese oxides, octahedral molecular sieves (OMS-2), and octahedral layered (OL-1) manganese oxide structures*. The Journal of Physical Chemistry C, 116, pp.6474-6483.
132. Pokhrel, R., Goetz, M.K., Shaner, S.E., Wu, X. and Stahl, S.S., 2015. *The "best catalyst" for water oxidation depends on the oxidation method employed: a case study of manganese oxides*. Journal of the American Chemical Society, 137, pp.8384-8387.
133. Zheng, M. and Dismukes, G.C., 1996. *Orbital configuration of the valence electrons, ligand field symmetry, and manganese oxidation states of the photosynthetic water oxidizing complex: analysis of the S_2 state multiline EPR signals*. Inorganic chemistry, 35, pp.3307-3319.
134. Jin, L., Smith, P., Noble, C.J., Stranger, R., Hanson, G.R. and Pace, R.J., 2014. *Electronic structure of the oxygen evolving complex in photosystem II, as revealed by ^{55}Mn Davies ENDOR studies at 2.5 K*. Physical Chemistry Chemical Physics, 16, pp.7799-7812.
135. Kulik, L.V., Epel, B., Lubitz, W. and Messinger, J., 2007. *Electronic structure of the Mn_4O_xCa cluster in the S_0 and S_2 States of the oxygen-evolving complex of photosystem II based on pulse ^{55}Mn-ENDOR and EPR spectroscopy*. Journal of the American Chemical Society, 129, pp.13421-13435.
136. Peloquin, J.M., Campbell, K.A., Randall, D.W., Evanchik, M.A., Pecoraro, V.L., Armstrong, W.H. and Britt, R.D., 2000. *^{55}Mn ENDOR of the S_2-state multiline EPR signal of photosystem II: implications on the structure of the tetranuclear Mn cluster*. Journal of the American Chemical Society, 122, pp.10926-10942.
137. Peloquin, J.M. and Britt, R.D., 2001. *EPR/ENDOR characterization of the physical and electronic structure of the OEC Mn cluster*. Biochimica et Biophysica Acta (BBA)-Bioenergetics, 1503, pp.96-111.
138. Messinger, J., Robblee, J.H., Bergmann, U., Fernandez, C., Glatzel, P., Visser, H., Cinco, R.M., McFarlane, K.L., Bellacchio, E., Pizarro, S.A. and Cramer, S.P., 2001. *Absence of Mn-centered oxidation in the $S_2 \rightarrow S_3$ transition: implications for the mechanism of photosynthetic water oxidation*. Journal of the American Chemical Society, 123, pp.7804-7820.
139. Iuzzolino, L., Dittmer, J., Dörner, W., Meyer-Klaucke, W. and Dau, H., 1998. *X-ray absorption spectroscopy on layered photosystem II membrane particles suggests manganese-centered oxidation of the oxygen-evolving complex for the S_0-S_1, S_1-S_2, and S_2-S_3 transitions of the water oxidation cycle*. Biochemistry, 37, pp.17112-17119.
140. Roelofs, T.A., Liang, W., Latimer, M.J., Cinco, R.M., Rompel, A., Andrews, J.C., Sauer, K., Yachandra, V.K. and Klein, M.P., 1996. *Oxidation states of the manganese cluster during the flash-induced S-state cycle of the photosynthetic oxygen-evolving complex*. Proceedings of the National Academy of Sciences, 93, pp.3335-3340.
141. Yachandra, V.K., DeRose, V.J., Latimer, M.J., Mukerji, I., Sauer, K. and Klein, M.P., 1993. *Where plants make oxygen: a structural model for the photosynthetic oxygen-evolving manganese cluster*. Science, 260, pp.675-679.
142. Haumann, M., Müller, C., Liebisch, P., Iuzzolino, L., Dittmer, J., Grabolle, M., Neisius, T., Meyer-Klaucke, W. and Dau, H., 2005. *Structural and oxidation state changes of the photosystem II manganese complex in four transitions of the water oxidation cycle ($S_0 \rightarrow S_1$, $S_1 \rightarrow S_2$, $S_2 \rightarrow S_3$, and $S_{3,4} \rightarrow S_0$) characterized by X-ray absorption spectroscopy at 20 K and room temperature*. Biochemistry, 44, pp.1894-1908.
143. Pace, R.J., Jin, L. and Stranger, R., 2012. *What spectroscopy reveals concerning the Mn oxidation levels in the oxygen evolving complex of photosystem II: X-ray to near infra-red*. Dalton Transactions, 41, pp.11145-11160.
144. Krewald, V., Retegan, M., Cox, N., Messinger, J., Lubitz, W., DeBeer, S., Neese, F. and Pantazis, D.A., 2015. *Metal oxidation states in biological water splitting*. Chemical science, 6, pp.1676-1695.

Chapter 3

Mechanochemical synthesis of MnO_2 and its photocatalytic dye degradation activities

Remarks:

The publication relevant to this chapter is "Ankita Gagrani, Jingwei Zhou, Takuya Tsuzuki, "*Solvent free mechanochemical synthesis of MnO_2 for the efficient degradation of Rhodamine-B*", **Ceramics International**, 44, 4694-4698, **2018**". The abstract, introduction and conclusion section of the chapter slightly differ from the publication to meet the coherency needs of the thesis. The chapter also contains an additional discussion on the mechanism of dye degradation.

Abstract

This chapter reports the experimental investigation of the synthesis of amorphous and crystalline MnO_2 and their dye decolourization abilities under dark and light conditions at different pH levels. A solid-state redox reaction $2KMnO_4 + MnCl_2 \rightarrow 3MnO_2 + 2KCl + O_2$ was activated during mechanical milling. Excess KCl salt was added in the starting powder mixture to prevent agglomeration of MnO_2 nanoparticles. The milling resulted in the production of amorphous MnO_2 nanoparticles with a high surface area of 204 $m^2\ g^{-1}$. Crystalline MnO_2 nanorods of diameters about 15 nm – 20 nm were produced by heating the as-milled powder at 350°C for 1 h in air. Both amorphous and crystalline MnO_2 demonstrated potential for photocatalysis at pH 7, whereas dissolution of manganese occurred at pH 3. This work demonstrates the potential for cost effective, green and scalable synthesis of MnO_2 nano-catalysts for environmental applications.

3.1 Introduction

Visible-light photocatalytic reaction is one of the promising ways to address many energy and environmental challenges using sunlight. Therefore, developing visible light photocatalyst and evaluating their photocatalytic activities have gained significant importance [1]. A common method to evaluate the photocatalytic activities of catalysts is photocatalytic degradation of dyes under light. Historically, the aim of photocatalytic dye degradation was to treat large amounts of dye effluents released from textile, paper and cosmetic industries [2]. However later, with the introduction of self-cleaning surfaces, dye degradation under light became a common tool for demonstrating potential photocatalytic properties instead of serving as an actual contaminant [3], despite some drawbacks [4-5]. This chapter reports the experimental investigation of the synthesis of MnO_2 photocatalysts and evaluation of photocatalytic abilities using dye as a model compound.

Manganese dioxide has been of significant practical interest as a photocatalyst due to its considerable redox activity, low cost and earth-abundant composition [6]. Several efforts have been made for the development of various morphologies of MnO_2 to enhance the catalytic performance [7-9]. Dang's group investigated the decolourization of methylene blue and methyl orange with a MnO_2-coated diatomite composite prepared using a wet-chemical method [10]. Combariza's group reported the removal of indigo carmine dye by a bio-nano composite produced by in situ synthesis of nanostructured MnO_2 onto natural fique fibers [11]. Fathy *et al*. prepared a γ-MnO_2/MWCNT nanocomposite catalyst using a co-precipitation approach and evaluated the oxidative degradation of RB19 dye [12]. Cui *et al*. employed a refluxing process to synthesize manganese oxides with different crystal types (α-MnO_2, β-MnO_2, and δ-MnO_2) and reported decolourization of Rhodamine-B (RhB) dye at various pH levels [13]. These

studies focused on evaluating catalytic degradation and adsorption of dyes using MnO_2. Yin *et al*. reported a simple hydrothermal synthesis of MnO_2 nanorods and studied their photocatalytic performance on the degradation of congo red, eosin red and methyl orange under UV-light irradiation [14].

From the analysis of past work, significant research gaps have been identified. Although many research groups have studied the catalytic properties of manganese dioxide, no study has focused on evaluating photocatalytic properties of MnO_2 synthesized using environmentally friendly methods. Since photocatalytic activities of catalysts are dependent on synthesis methods [3], the green production of MnO_2 nanoparticles and their photocatalysis requires further research. Furthermore, the effect of crystallinity on the photocatalytic activities of MnO_2 nanoparticles has not been fully understood. The present study addresses these research gaps by investigating photocatalytic properties of amorphous and crystalline MnO_2 synthesized by a solvent-free mechanochemical method.

Mechanochemical processing (MCP) is a unique bottom-up approach to synthesise a variety of nanomaterials [15-17]. It is a scalable technique utilising mechanical energy to trigger chemical reactions in a ball mill. Previously, a report by Liu *et al*. demonstrated the mechanochemical synthesis of MnO_2 using $KMnO_4$ and $Mn(CH_3COO)_2$ and employed H_2SO_4 to remove K^+ to study the charge-discharge properties of MnO_2 supercapacitor [18]. However, the use of H_2SO_4 during synthesis is a considerable drawback for environment. Synthesizing a catalyst using a solvent free method is of utmost importance for environmental sustainability. Moreover, the particle size of resulting MnO_2 was not reported. Another report by Yang *et al*. demonstrated the synthesis of MnO_x via a redox reaction between Mn^{7+} and Mn^{2+} in a ball mill [19]. However, the end product consisted of highly agglomerated particles.

In this work, amorphous MnO_2 particles and crystalline MnO_2 nanorods were synthesized via a low cost, solvent free and scalable mechanochemical route for the first time and their photocatalytic activities to degrade dyes were investigated. A mixture of $KMnO_4$ and $MnCl_2$ was milled to initiate a solid-state redox reaction $2KMnO_4 + MnCl_2 \rightarrow 3MnO_2 + 2KCl + O_2$. Excess KCl was introduced in the starting powder mixture to control the particle size of MnO_2 in the product phase. RhB dye was chosen as a model dye for the evaluation of photocatalytic activity based on its popularity for studying visible light photocatalysis [3].

3.2 Experimental Procedure

3.2.1 Preparation of MnO_2 nanoparticles

All chemicals were used without further purification. Stoichiometric amounts of $KMnO_4$ (analytical grade, Univar) and $MnCl_2$ (99.9%, Sigma Aldrich) powders were mixed in the molar ratio of 2:1. KCl (Analar NORMAPUR, VWR) powder was added to this mixture as an inert diluent to ensure that the volume fraction of MnO_2 is 10% in the product phase in order to limit the agglomeration of MnO_2 [20]. All three chemicals were sealed in a steel vial with hardened steel balls of 9.2 mm in diameter. The ball to powder ratio of 10:1 was used for all milling operations. The mixture was milled for 4h in a SPEX 8000M mill (Spex, USA). The as-milled powder was heated at 350° C for 1 h in air to crystallize amorphous MnO_2. The powder was washed thrice to remove KCl, with Millipore Milli-Q ultrapure water (18 MΩ cm) using an ultrasonic bath and a centrifuge. The remaining black powder was collected and dried in an oven at 50°C for 9 h.

3.2.2 Physical characterization

The composition of the powder was examined at room temperature using a D_2 Phaser X-ray diffraction system (XRD, Bruker, USA) with Cu-Kα radiation. The average crystallite sizes were estimated from the diffraction peak using the Scherrer equation [21]. The nanostructure and surface morphology of the powder was investigated using a CM 300 transmission electron microscope (TEM, FEI, USA) at 300 kV and an Ultra Plus field-emission scanning electron microscope (FESEM, Zeiss, Germany) at 3 kV. The specific surface area of nanopowders was measured by the Brunauer-Emmett-Teller (BET) N_2-gas adsorption method using a TriStar 3020 (Micromeritics, USA). Prior to BET measurements, the powders were degassed at 150 °C for 24 h. UV-vis absorption spectra were collected using a Varian Cary 60 spectrometer (Agilent, USA). Optical band gap energies were estimated by converting UV-Vis absorption spectra into Tauc plots [22].

3.2.3 Band edge position

To investigate the mechanism of photocatalytic dye degradation, photocurrent measurements were carried out. The results were used to estimate the band edge positions [23] and charge separation efficiencies of the catalysts [24].

Band-edge positions of manganese oxides were determined using a photocurrent onset technique [23]. Manganese oxide electrodes were prepared in the following manner. First, 15 mg of powder was dispersed in 15 mL ethanol using an ultrasonic bath. Then, 4 mL of the solution was gradually dropped on a rectangular piece (1.5 x 3 cm) of cleaned glass coated with fluorine-doped tin oxide, on a hot plate at 200°C. After deposition, the electrodes were kept on

the hotplate for another 5 min. An electrochemical cell was constructed with a manganese dioxide electrode as a working electrode, platinum as a counter electrode, Ag/AgCl as a reference electrode and 0.1 M KCl solution as an electrolyte. The electrolyte was bubbled with nitrogen gas for 3 h prior to measurements to remove any dissolved oxygen. Photo-electrochemical measurements were carried out using a potentiostat (Bio-Logic VMP3) and a set of light emitting diodes (220 V,100 W). The irradiation spectrum measured using a silicone-based charge-coupled device, is shown in Figure 3.1. The light source was placed 10 cm away from the working electrode.

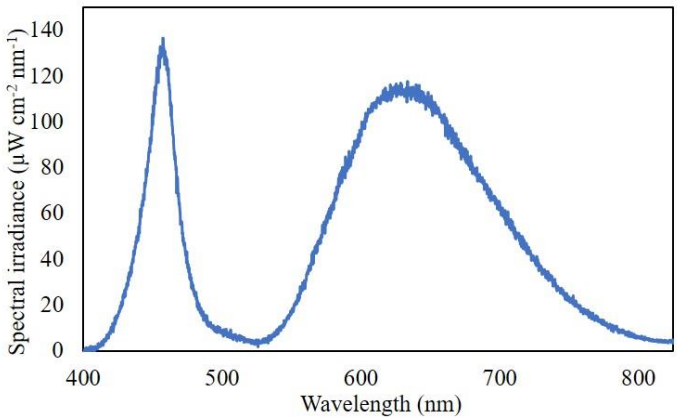

Figure 3.1. Spectrum of LED light.

For the analysis of charge separation efficiency, the same experimental setup as for the determination of band-edge positions was used, except replacing KCl electrolyte with 0.1 M sodium sulphite. In practice, water oxidation photocurrent (J_{H2O}) of catalysts is always less than maximum photocurrent (J_{max}) due to limited light absorption efficiency (η_{abs}), charge separation efficiency (η_{sep}), and charge transfer efficiency (η_{trans}), and can be expressed by the following equation:

$$J_{H2O} = J_{max} \cdot \eta_{abs} \cdot \eta_{sep} \cdot \eta_{trans} \quad (3.1).$$

η_{sep} was estimated from the measured values of J_{max}, η_{abs}, η_{trans}, and J_{H2O}, using equation 3.1. J_{max} was determined by integrating the incident spectral irradiance (as shown in Figure 3.1) over all wavelengths. η_{abs} was determined by integrating the product of the incident spectral irradiance and the light harvesting efficiency (LHE) at each wavelength and dividing by J_{max}. LHE of the electrodes was calculated using following equation:

$$\text{LHE}\ (\lambda)\ (\%) = 100\% - \text{R}(\lambda)\ (\%) - \text{T}(\lambda)\ (\%) \qquad (3.2),$$

where R is the total reflection and T is the total transmission. Charge transfer efficiency (η_{trans}) is nearly equal to 100% in the presence of sodium sulphite electrolyte, which acts as a hole scavenger, and undergoes fast oxidation [24]. J_{H2O} was obtained experimentally by subtracting dark current from light current at selected voltage points.

3.2.4 Photocatalytic activity evaluation by degradation of Rhodamine B

Photocatalytic degradation of RhB dye was studied to evaluate the photocatalytic activity of MnO_2 samples. A small amount of MnO_2 (8 mg) was dispersed in 50 mL of an aqueous RhB solution with a concentration of 0.0096 mg mL^{-1}. The pH of the solution was adjusted with HCl. A low-density polyethylene film (>85% transparent to UVA and UVB) was tightly wrapped to seal the mouth of the silica beaker for preventing the evaporation of water. Subsequently, the suspension was irradiated with simulated sunlight using a Suntest CPS+ instrument (Atlas, USA) equipped with a 1,500 W xenon lamp and a daylight reduced IR filter. The irradiation intensity was 65 W m^{-2} over the wavelength range of 300–800 nm. The aliquots (4 mL) were collected at various irradiation times and immediately centrifuged at 12,000 rpm for 10 min to remove catalyst nanoparticles from the RhB solution. The Optical

absorption of the RhB solution was measured using a Cary 60 spectrophotometer (Agilent, USA) to observe the photocatalytic degradation of RhB. The degradation of RhB was also investigated without light irradiation otherwise under the same conditions for both amorphous and crystalline samples.

3.3 Result and discussions

3.3.1 MnO_2 nanoparticles

Figure 3.2(a) shows the XRD pattern of the powder milled for 4 h. The pattern predominantly consists of peaks corresponding to KCl (JCPDS card No 73-0380) due to the presence of excess KCl in the powder mixture. Figure 3.2(b) represents the XRD pattern of the powder after washing to remove KCl. The lack of well-defined sharp peaks, except two broad peaks near 13° and 37°, can be attributed to the amorphous-like nature of the powder. Figure 3.2(c) represents the XRD pattern of the powder after heat treatment at 350°C for 1 h in air and subsequently washed, where the diffraction peaks can be indexed to α-MnO_2 (JCPDS card No 72-1982).

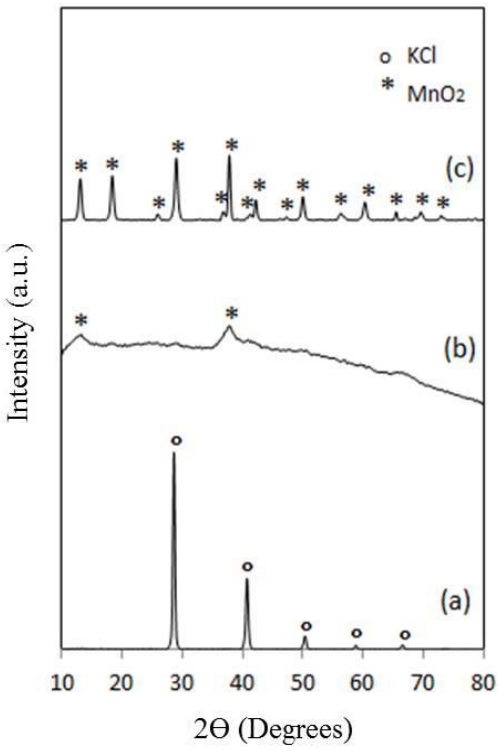

Figure 3.2. XRD patterns of (a) as-milled powder milled for 4 h, (b) after subsequent washing and drying, and (c) powder milled for 4 h followed by heat treatment at 350°C, washing and drying.

Figures 3.3 (a) and (c) show a typical SEM and TEM images of MnO_2 samples without heat treatment. The sample consisted of irregular-shaped particles and few needle-like structures of less than 10 nm in diameter. The inset in Figure 3.3(c) is a selected area electron diffraction pattern, showing narrow rings with only few spots. The result indicates poor crystalline nature of the MnO_2, consistent with the XRD data (Fig. 3.2b). The few spots on the diffraction rings may stem from the needle-like structure visible in the SEM image. The needle-like structure was not observed in TEM images, possibly due to the scarcity of the structure. Figures 3.3 (b) and (d) show the respective SEM and TEM images of crystalline MnO_2 that was obtained after heat treatment. The sample consisted of only nanorods of about 15 nm - 20 nm in diameter with varying lengths. The inset in Figure 3.3(d) shows lattice fringes running parallel to the

surface of a nanorod along the length direction. The lattice spacing between adjacent lattices was ~0.7 nm corresponding with the distance between two (110) crystal planes of α-MnO_2.

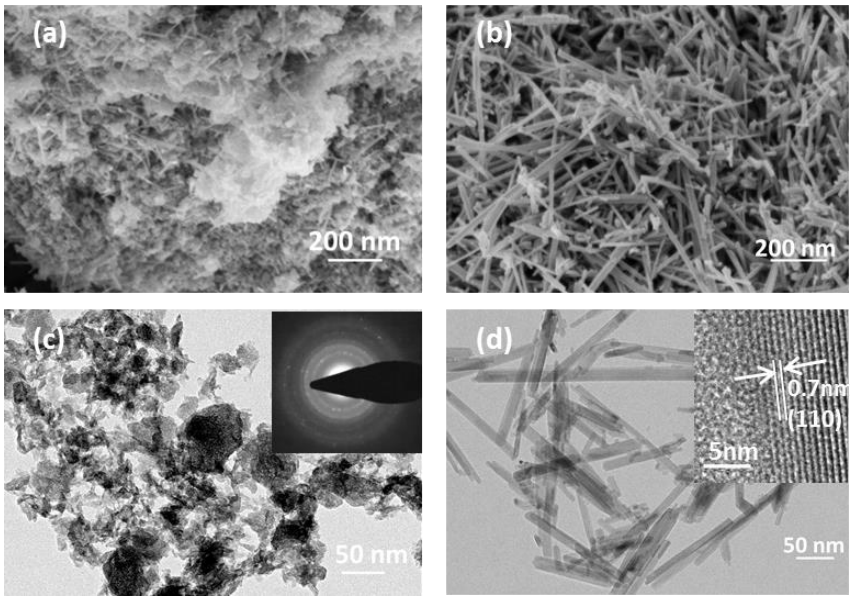

Figure 3.3. FESEM micrograph of (a) amorphous MnO_2 and (b) crystalline MnO_2; TEM micrograph of (c) amorphous MnO_2 and (d) crystalline MnO_2. The inset in image (c) shows a selected area electron diffraction pattern of the same area. The inset in image (d) shows lattice fringes running parallel to the surface of a nanorod along the length direction.

The average crystallite size estimated using the diffraction peak corresponding to (110) crystal plane at 13° was 16 nm. This value is in good agreement with the observed diameter of nanorods. The BET surface areas of the amorphous and crystalline MnO_2 powders were 204 $m^2 g^{-1}$ and 76 $m^2 g^{-1}$, respectively.

Figure 3.4 shows the Tauc plot in the form of $(\alpha h\nu)^2$ versus $h\nu$ for (a) amorphous and (b) crystalline MnO_2, where h is the Planck's constant, ν is the photon's frequency, and α is the absorption coefficient. The Tauc plot was made from the optical absorption spectra shown in

Figure 3.5. The intercept of the straight line with the x-axis (energy axis) suggests an optical band gap of 2.54 eV and 2.33 eV for amorphous and crystalline MnO_2, respectively.

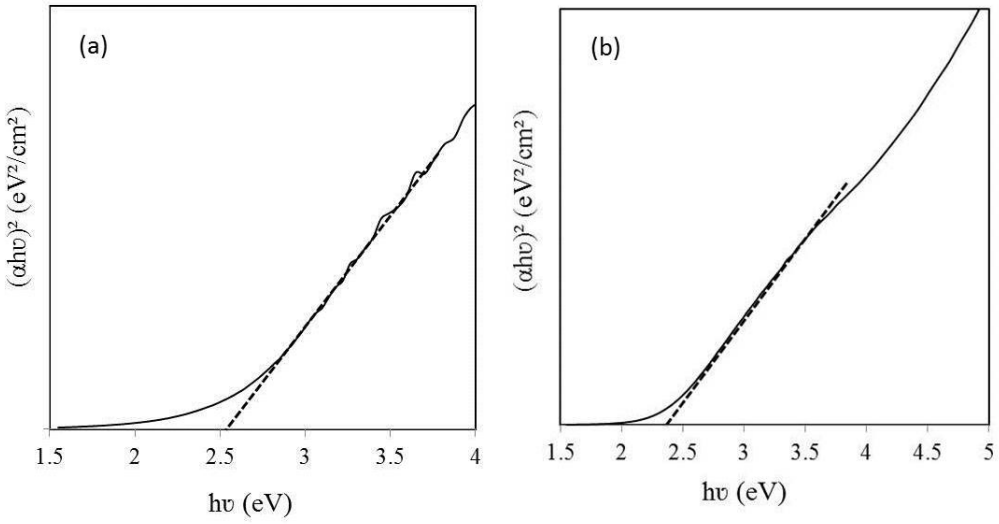

Figure 3.4. Tauc plot of (a) amorphous MnO_2 and (b) crystalline MnO_2 nanowires.

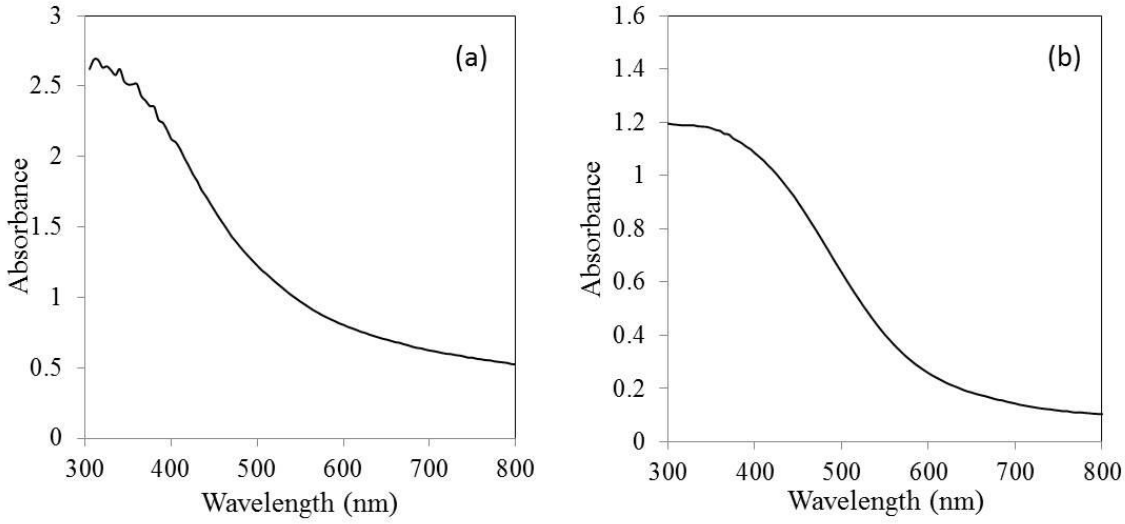

Figure 3.5. UV-Vis absorbance spectra of (a) amorphous MnO_2 and (b) Crystalline MnO_2.

3.3.2 Dye degradation

Figures 3.6 (a) and (b) show the dye degradation rates at different pH levels upon light irradiation for amorphous and crystalline MnO_2, respectively. The original optical absorption spectra of RhB dye solutions are shown in Figure 3.7. In the y-axis of Figure 3.6, C is the absorbance value of RhB at each irradiation time and C_0 is the absorbance value at the same wavelength before the irradiation.

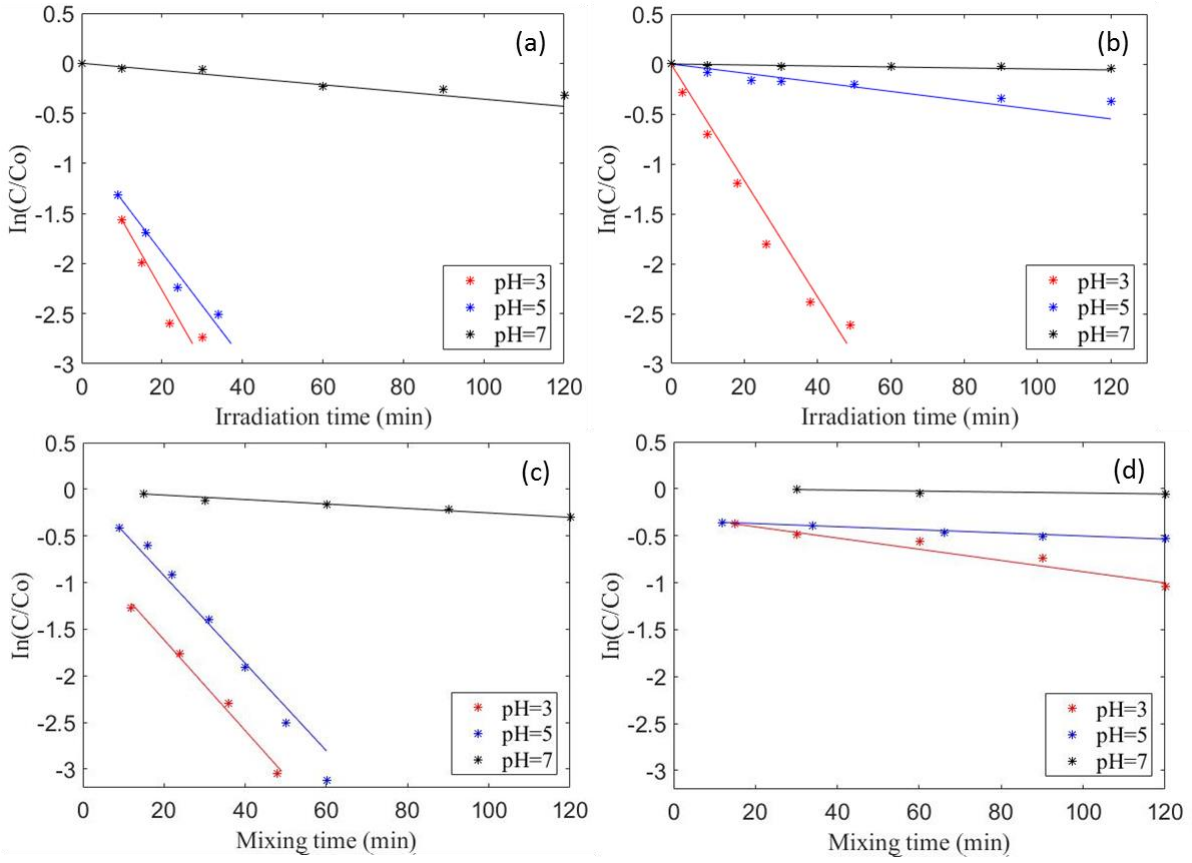

Figure 3.6. Pseudo-first order kinetic models for the degradation process at various pH values for (a) amorphous MnO_2, (b) crystalline MnO_2 upon irradiation of light, and (c) amorphous MnO_2 and (d) crystalline MnO_2 without light irradiation.

At pH 7, only 4 % of the dye was decolorized within 120 min by the crystalline sample. On the other hand, the amorphous sample degraded nearly 28 % of the dye within the same exposure time. For the crystalline sample, lowering the pH to 5 resulted in the degradation efficiency to reach above 47% in 120 min of irradiation. At this pH level, the amorphous sample degraded the dye almost completely in 34 min. At pH 3, the absorption peaks corresponding to the dye diminished in 30 min and 49 min with the amorphous and crystalline MnO_2, respectively. MnO_2 was responsible for dye degradation because the RhB dye does not decolorize in the absence of catalyst, even in the presence of light [25].

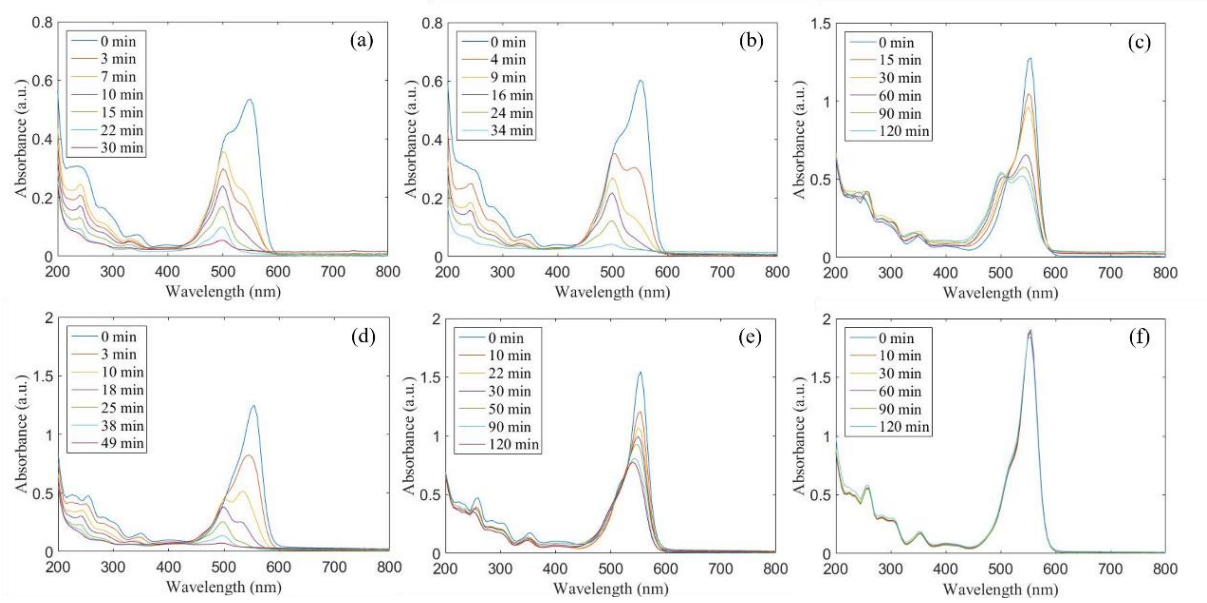

Figure 3.7. Exposure time profiles of UV-Vis absorbance spectra of Rhodamine-B solutions under simulated sunlight in the presence of amorphous MnO_2 at (a) pH 3 (b) pH 5 (c) pH 7 and crystalline MnO_2 at (d) pH 3 (e) pH 5 (f) pH 7.

Figures 3.6 (c) and (d) show the dye degradation rates at different pH levels in the dark without light irradiation, for amorphous and crystalline MnO_2, respectively. The original optical absorption spectra of RhB dye solutions are shown in Figure 3.8. The changes in peak shape and peak position at 450 – 600 nm indicate the removal of RhB by degradation, not by

adsorption alone. At pH 7, after 120 min of mixing time, only 2% of RhB was degraded by the crystalline sample. In contrast, 26% of the dye was degraded by the amorphous sample. Further lowering the pH to 5 resulted in 40% degradation of the dye by crystalline sample. At this pH, the amorphous sample degraded almost entire dye in just 60 min. At pH 3, the amorphous sample degraded 95% of the dye in 48 min, which is a significantly higher degradation rate than that of the crystalline MnO_2 which could only degrade 73% of the dye in 120 min.

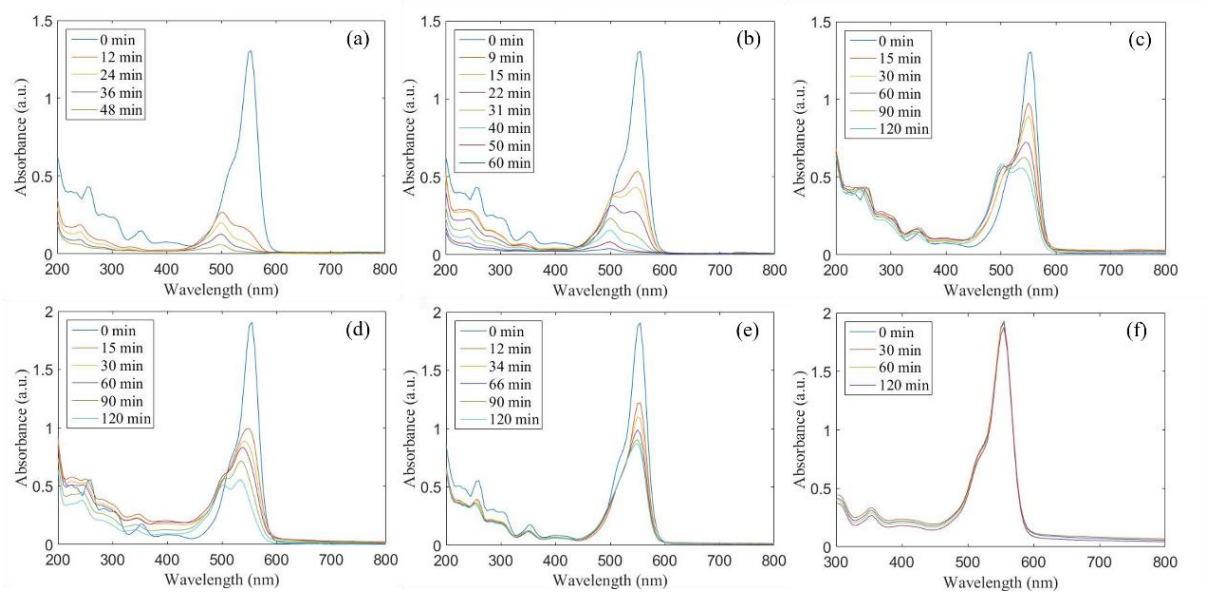

Figure 3.8. Exposure time profiles of UV-Vis absorbance spectra of Rhodamine-B solutions under the dark condition in the presence of amorphous MnO_2 at (a) pH 3 (b) pH 5 (c) pH 7 and crystalline MnO_2 at (d) pH 3 (e) pH 5 (f) pH 7.

From the above data, it is observed that at pH 7, the dye decolorization was higher for amorphous sample in both dark and light than crystalline sample. Increased dye degradation for amorphous sample could be attributed to higher adsorption due to higher surface area. The adsorption of dye species on the catalyst surfaces is enhanced within a pH range where the dye and catalyst have opposite electrostatic charges. RhB is a cationic dye. The Iso-electric point

of MnO_2 is reported to be <5.1 above which the particle surface is negatively charged due to de-protonation. As such, once can expect that the adsorption of RhB on the MnO_2 surfaces is stronger above pH 5 [26]. At pH 7, the effect of light was not significant (only 2% increase in dye decolorization with light). For understanding the photocatalytic effect, knowledge of energy levels of conduction and valence band is crucial. Figure 3.10 shows the band-edge positions of the manganese dioxides, estimated using the photocurrent onset method, as shown in Figure 3.9. The lower edge of the conduction band at pH 7 was determined for amorphous and crystalline MnO_2 as 0.42 and 0.45 eV, respectively. By using the measured band-edge positions and bandgap energies, the schematic energy-level diagram of MnO_2 is drawn in Figure 3.10, with respect to the electro-chemical potentials of $O_2 + e^- = O_2^{\bullet -}$, $Mn^{4+}+2e^-=Mn^{2+}$ and $OH^- + h^+ = OH^\bullet$ at pH 7. The highest occupied molecular orbital (HOMO) and lowest unoccupied molecular orbital (LUMO) energy levels of RhB are also given in Figure 3.10 [25].

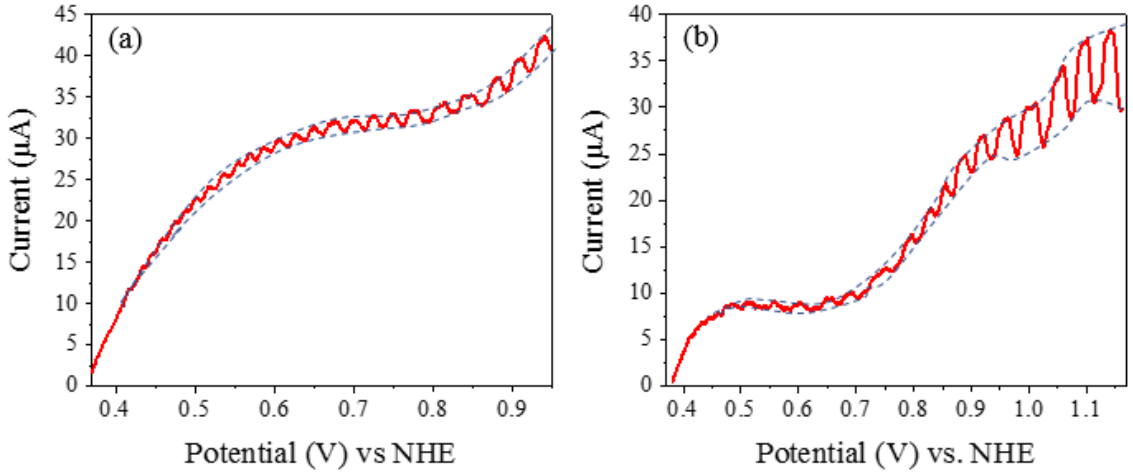

Figure 3.9. Current potential curve (at 0.1 mV/s) of (a) amorphous MnO_2, (b) crystalline MnO_2 under chopped illumination. The potential vs NHE at pH 7 is shown.

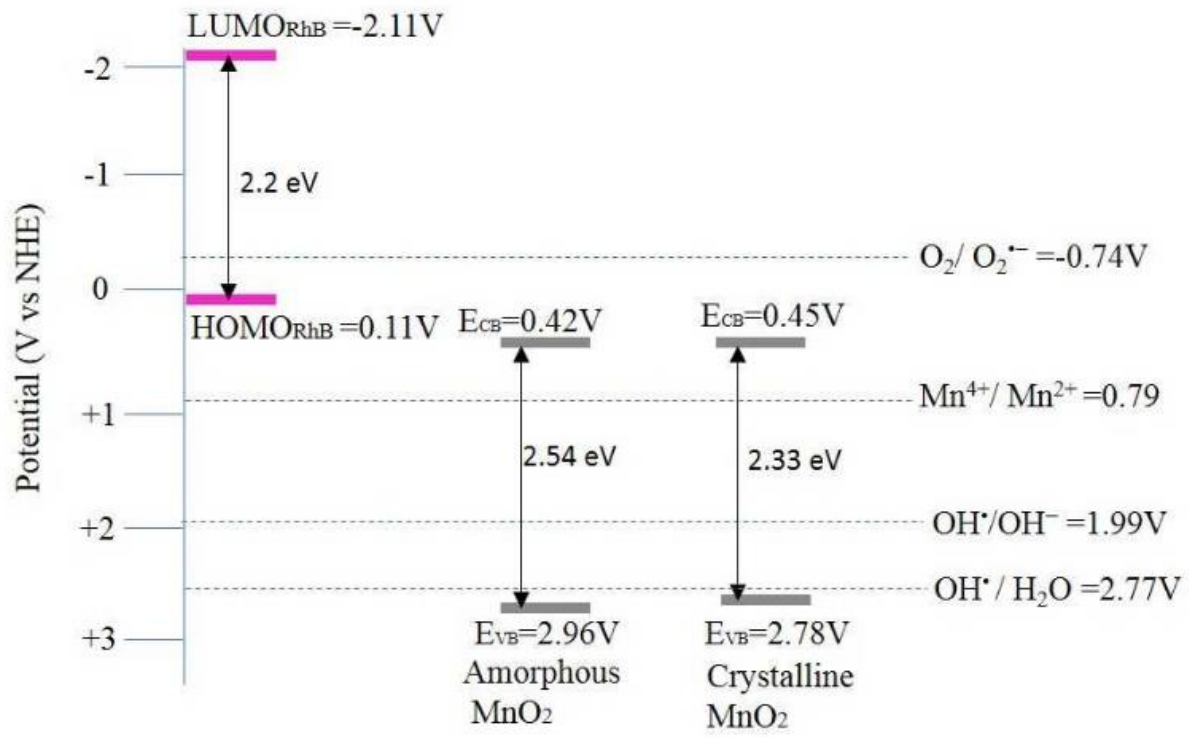

Figure 3.10. Schematic energy level diagram of amorphous and crystalline MnO_2 with respect to the electrochemical potentials of $OH^{\bullet}/H_2O$, $O_2/ O_2^{\bullet-}$ and $OH^{\bullet}/OH^{-}$ at pH 7.

As shown in Figure 3.10, the valence band of MnO_2 is more positive than the potential required for formation of hydroxyl free radicals from water. Hence theoretically speaking, MnO_2 will form hydroxyl free radicals by light absorption. However, experimental data showed poor ability of RhB MnO_2 to degrade RhB in the presence of light. This may be due to the following three reasons:

Firstly, RhB is shielding the light from reaching MnO_2. Since RhB has a narrower bandgap energy than MnO_2, RhB acts as an effective light-shade to MnO_2. One can speculate that the relatively high absorption of light by free dye molecules might have reduced the number of photons absorbed by MnO_2, resulting in reduced rate of photocatalytic degradation of dye [27]. This is a typical drawback of using coloured dyes for the study of visible-light photocatalysis.

However, the concentration of dyes used in the present study was very low to avoid this light-shielding effects [28].

Secondly, the combination of RhB and MnO_2 does not form a dye-sensitisation of MnO_2, so that photo-exited electrons and holes are not effectively separated from each other. At pH 7, MnO_2 and RhB have opposite electrostatic charges [26], which causes a strong electrostatic interaction between RhB and MnO_2, resulting in the coating of RhB molecules on the surface of MnO_2. However, the HOMO and LUMO of RhB and band edge position of MnO_2 do not allow efficient charge transfer between MnO_2 and RhB. The absence of photolysis in RhB dye indicates that, the photo-excited electrons in RhB are not used to generate superoxide free radicals via transfer from LUMO to the electro-chemical potentials of $O_2 + e^- = O_2^{\bullet -}$ even if it is energetically possible [25]. This indicates that most of the photo-generated charges in RhB recombine within the dye molecule. Since the conduction band edge of MnO_2 is lower than the electrochemical potential of superoxide free radical formation, photo-exited electrons in MnO_2 does not contribute to the dye degradation. In MnO_2, photo-exited holes would be used to generate hydroxyl free radicals which in turn degrade RhB. Yin *et al*. showed that the efficiency of photocatalytic dye degradation was in the order of methyl orange < eosin red (96%) < congo red, in the presence of MnO_2 [14]. Their study also demonstrates that the absorption of light by dyes, band gap of dyes and band edge positions of dyes and catalysts, play a crucial role in evaluating photocatalytic properties of a novel semiconductor material.

Thirdly, MnO_2 has a poor charge-separation efficiency. Figure 3.13 shows the charge separation efficiency of the MnO_2 catalyst at different voltage. The charge separation efficiency was calculated using Equation (3.1). The measured J_{max} value was 9.8 mA cm^{-2}. η_{abs} calculated using LHE curves (as shown in Figure 3.11) were 83% and 96% for amorphous and crystalline

MnO_2, respectively. In Figure 3.13, charge separation efficiency is only defined at 4 voltage points, because the signal-to-noise ratio in observed photocurrent (as shown in Figure 3.12) was relatively poor, making it difficult to calculate photocurrent across a wide range of voltage. To take into consideration the errors in photocurrent measurements, error bars are indicated in Figure 3.13. It is evident that charge separation efficiency of amorphous and crystalline MnO_2 was nearly the same at low voltages, which was three orders of magnitude smaller than TiO_2 [29-31]. It is important to note that J_{H_2O} was in the range of $\mu A\ cm^{-2}$ (Figure 3.12), even when the charge transfer efficiency was close to 100% and absorption efficiency was reasonable, demonstrating poor charge separation efficiency of MnO_2 photocatalyst.

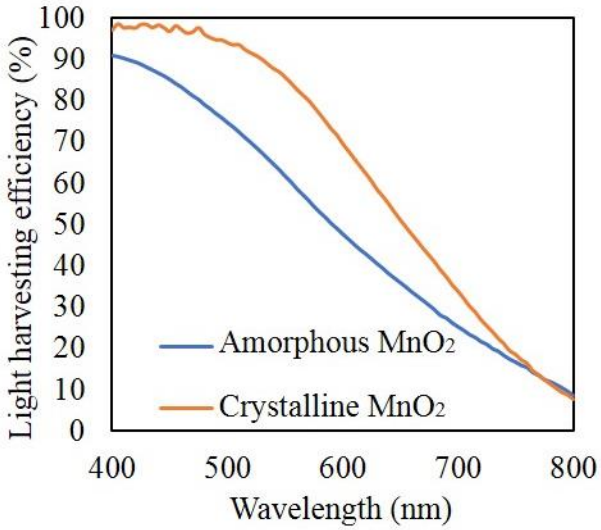

Figure 3.11. Light harvesting efficiency of amorphous MnO_2 and crystalline MnO_2.

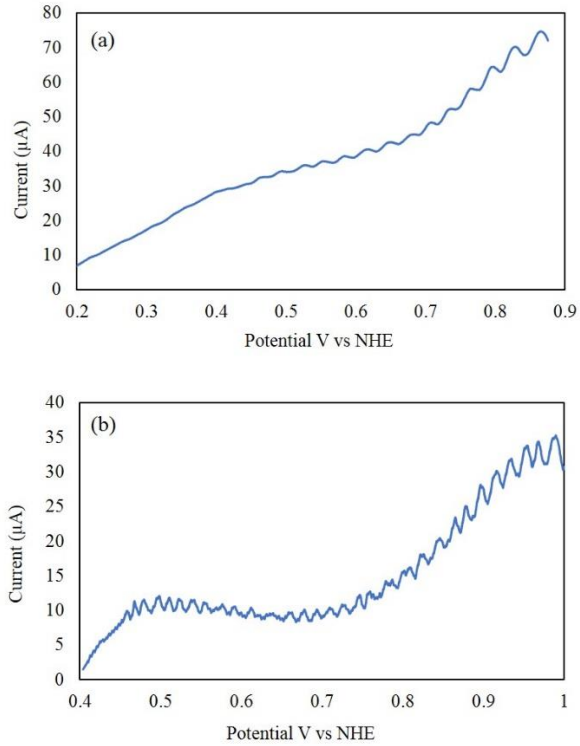

Figure 3.12. Current potential curve (at 0.1 mV/s) of (a) amorphous MnO_2 and (b) crystalline MnO_2 under chopped illumination (at pH 7) in the presence of sodium sulphite electrolyte.

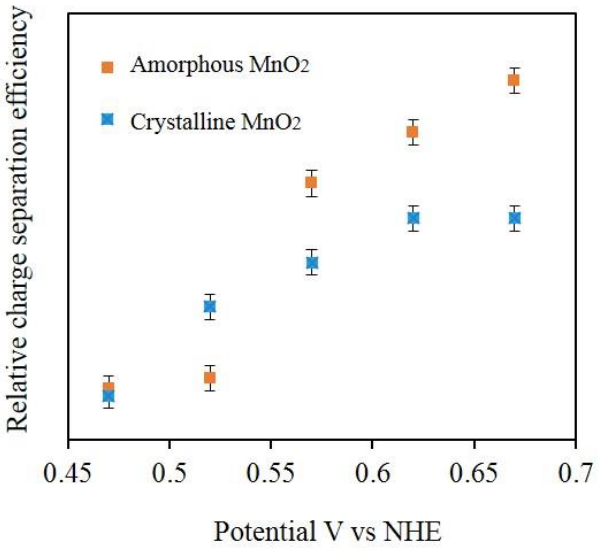

Figure 3.13. Relative charge separation efficiency of amorphous MnO_2 and crystalline MnO_2.

In contrast, at pH 3, excellent dye decolourization was observed for both amorphous and crystalline MnO_2 both under dark and illumination conditions, with an improved photo-catalysis. One possible explanation of this behaviour is reductive dissolution of Mn^{4+} in Mn^{2+} in aqueous solution under pH less than 7, where Mn^{4+} can change to Mn^{2+} to form strongly oxidizing hydroxyl radicals with help from H^+ ions [11]. Light irradiation further accelerated the degradation rate for both amorphous and crystalline MnO_2, due to the photo-induced free radical generation and photo-dissolution [32] of MnO_2, as evidenced in Figure 3.6.

From the Figure 3.6, it is also evident that the dye degradation in the presence of crystalline and amorphous MnO_2 showed linear relationships between $\ln(C/C_0)$ and irradiation time, indicating pseudo-first order kinetic models for the degradation process [33]. Under the dark condition, the dye removal proceeded quickly in the short time span after the mixing of MnO_2 into the dye solution and then afterwards followed pseudo first order kinetics throughout the degradation process (Figure 3.10). Similar behaviours in the initial stage of mixing MnO_2 with dye solutions were reported previously [34, 35]. One possible explanation for this behaviour is the high rate of adsorption of dye molecules on the surface of MnO_2 nanoparticles after mixing [36, 37]. This phenomenon was more pronounced for amorphous samples than crystalline samples (Figure 3.6), due mainly to the higher specific surface area of the amorphous samples.

The pseudo first order degradation rate constant (k, min^{-1}) at each pH value was calculated by fitting the data in Figure 3.6 with the following equation [27];

$$\ln (C/C_0) = - k \cdot t \qquad (3.3),$$

where t (min) is the irradiation time under light or mixing time under the dark condition. Due to the fast adsorption of the dye during the initial stage of mixing, $\ln(C/C_0)$ values are fitted only to the data points with t > ~10 min.

Figure 3.14 depicts the rate constants in the presence of amorphous and crystalline MnO_2 as a function of pH. To elucidate the effect of crystallinity, the rate constants in Figure 3.14 are normalised with the specific surface areas of the samples.

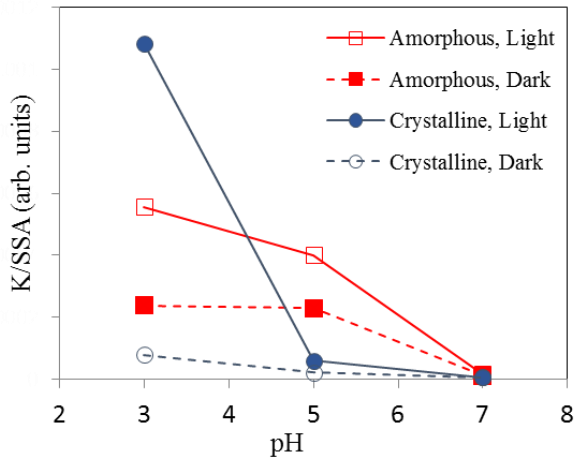

Figure 3.14. Dye-degradation rate constant (K) normalised with specific surface area (SSA) at various pH levels for amorphous and crystalline MnO_2 with and without light irradiation.

Under pH 3 condition, light illumination enhanced the dye-degradation ability significantly more for crystalline samples than for amorphous samples. This difference can be attributed to the fact that amorphous samples have a higher number of defects that act as recombination sites for photo-generated charges to suppress photo-corrosion [38].

It is interesting to note that, under the dark condition, amorphous MnO_2 showed much higher catalytic ability than crystalline MnO_2. Even under pH 5 condition, where crystalline MnO_2

showed almost no catalytic effect, amorphous MnO_2 exhibited strong ability to decompose RhB. The outstanding catalytic activity of amorphous MnO_2 was also reported by Iyer *et al*. on the selective photo-oxidation of 2-propanol, destruction of toxic organic compounds and water-oxidation [39]. They attributed the high activity to the ease of lattice oxygen mobility and excess surface oxygen in the amorphous structure. Robinson *et al*. compared the photo-oxidation of water by various manganese oxides with different crystal structures and argued that weaker and flexible Mn-O bonds are more catalytically reactive whereas stronger and rigid Mn-O bonds such as in crystalline MnO_2 do not foster the high oxidation potential for O_2 formation [40]. One can hypothesise that, amorphous MnO_2 is catalytically more reactive than crystalline MnO_2 due to the higher number of defects such as dangling bonds and oxygen vacancy sites [41] as well as weaker Mn-O bonds on the surface. Nonetheless, only few reports have been published on the catalysis of amorphous MnO_2 to date and further efforts are required to gain a full understanding of its mechanism [39].

3.4 Chapter summary

The chapter discussed the green synthesis and photocatalytic activities of MnO_2 at different pH values. The chapter also highlighted the drawbacks of using coloured dyes in evaluating visible-light photocatalysis of novel semiconductors. MnO_2 nanorods were successfully synthesized using a mechanochemical solid-state displacement reaction for the first time. During the ball milling of a $2KMnO_4 + MnCl_2 + KCl$ starting powder mixture, amorphous MnO_2 nanoparticles were formed. After subsequent calcination at 350° C for 1 hour in air, the amorphous MnO_2 was transformed into crystalline MnO_2 nanorods with diameters of less than 20 nm. In the presence of light, both amorphous and crystalline MnO_2 generated electron hole pairs. However, at pH 7, RhB dye degradation was insignificant, due to the absorption of light

by the dye, electrochemical energy mismatch between the dye and MnO_2, and poor charge separation efficiency of MnO_2. At pH 3, under the dark condition, both amorphous and crystalline phases exhibited catalytic activities to degrade the model dye pollutant, due to reductive dissolution of MnO_2 [42]. Irradiation of simulated sunlight accelerated the decomposition reaction of both amorphous and crystalline MnO_2 at pH 3, because photo-corrosion accelerated the reductive dissolution.

Along with MnO_2, it is significantly important to investigate the green synthesis and photocatalytic properties of bioinspired catalysts such as calcium manganese oxides, which is discussed in the next chapter.

.

3.5 References

1. Fujishima, A. and Honda, K., 1972. *Electrochemical Photolysis of Water at a Semiconductor Electrode.* Nature, 238, pp.37-38.
2. Lazar, T., 2005. *Color Chemistry: Synthesis, Properties, and Applications of Organic Dyes and Pigments, 3rd revised edition.* Color Research & Application, 30, pp.313-314.
3. Rochkind, M., Pasternak, S. and Paz, Y., 2015. *Using dyes for evaluating photocatalytic properties: a critical review*. Molecules, 20, pp.88-110.
4. Ohtani, B., 2010. *Photocatalysis A to Z—What we know and what we do not know in a scientific sense*. Journal of Photochemistry and Photobiology C: Photochemistry Reviews, 11, pp.157-178.
5. Ohtani, B., 2008. *Preparing articles on photocatalysis—beyond the illusions, misconceptions, and speculation*. Chemistry letters, 37, pp.216-229.
6. Ge, J. and Qu, J., 2003. *Degradation of azo dye acid red B on manganese dioxide in the absence and presence of ultrasonic irradiation.* Journal of Hazardous Materials, 100, pp.197-207.
7. Saputra, E., Muhammad, S., Sun, H., Ang, H.M., Tade, M.O. and Wang, S., 2013. *Different Crystallographic One-dimensional MnO_2 Nanomaterials and Their Superior Performance in Catalytic Phenol Degradation.* Environmental Science & Technology, 47, pp.5882-5887.
8. Liu, C., Pan, D., Tang, X., Hou, M. Zhou, Q. and Zhou, J., 2016. *Degradation of Rhodamine B by the α-MnO_2/Peroxymonosulfate System.* Water, Air, & Soil Pollution, 227, pp. 92.
9. Zhang, W., Yang, Z., Wang, X., Zhang, Y., Wen, X. and Yang, S., 2006. *Large-scale synthesis of β-MnO_2 nanorods and their rapid and efficient catalytic oxidation of methylene blue dye.* Catalysis. Communications,7, pp.408-412.
10. Dang, T.D., Banerjee, A.N., Tran, Q.T. and Roy, S., 2016. *Fast degradation of dyes in water using manganese-oxide-coated diatomite for environmental remediation.* Journal of Physics and Chemistry of Solids, 98, pp.50-58.
11. Chacón-Patiño, M.L., Blanco-Tirado, C., Hinestroza, J.P. and Combariza, M.Y., 2013. *Biocomposite of nanostructured MnO_2 and fique fibers for efficient dye degradation.* Green Chemistry, 15, pp.2920-2928.
12. Fathy, N.A., El-Shafey, S.E., El-Shafey, O.I. and Mohamed, W.S., 2013. *Oxidative degradation of RB19 dye by a novel γ-MnO_2/MWCNT nanocomposite catalyst with H_2O_2.* Journal of Environmental Chemical Engineering, 1, pp.858-864.
13. Cui, H.J., Huang, H.Z., Yuan, B. and Fu, M.L., 2015. *Decolorization of RhB dye by manganese oxides: effect of crystal type and solution pH.* Geochemical Transactions, 16, pp.10.
14. Yin, B., Zhang, S., Jiao, Y., Liu, Y., Qu, F. and Wu, X., 2014. *Facile synthesis of ultralong MnO_2 nanowires as high performance supercapacitor electrodes and photocatalysts with enhanced photocatalytic activities.* CrystEngComm, 16, pp.9999-10005.
15. Tsuzuki, T., Pethick, K. and McCormick, P.G., 2000. *Synthesis of $CaCO_3$ Nanoparticles by Mechanochemical Processing.* Journal of Nanoparticle Research, 2, pp.375-380.
16. Ding, J., Tsuzuki, T. and McCormick, P., 1997. *Mechanochemical synthesis of ultrafine ZrO_2 powder.* Nanostructured Materials, 8, pp.75-81.
17. Ding, J., Tsuzuki, T., McCormick, P.G. and Street, R., 1996. *Ultrafine Co and Ni particles prepared by mechanochemical processing.* Journal of Physics D: Applied Physics, 29, pp.2365-2369.
18. Liu, K.Y., Zhang, Y., Zhang, W., Zheng, H. and Geng, S.U., 2007. *Charge-discharge process of MnO_2 supercapacitor.* Transactions of Nonferrous Metals Society of China, 17, pp.649-653.
19. Yang, Y., Zhang, S., Wang, S., Zhang, K., Wang, H., Huang, J., Deng, S., Wang, B., Wang, Y. and Yu, G., 2015. *Ball Milling Synthesized MnO_x as Highly Active Catalyst for Gaseous POPs Removal: Significance of Mechanochemically Induced Oxygen Vacancies.* Environmental Science & Technology, 49, pp.4473-4480.
20. Tsuzuki, T. and McCormick, P.G., 2004. *Mechanochemical synthesis of nanoparticles.* Journal of Materials Science, 39, pp.5143-5146.

21. Muniz, F.T.L., Miranda, M.A.R., Morilla dos Santos, C. and Sasaki, J.M., 2016. *The Scherrer equation and the dynamical theory of X-ray diffraction.* Acta Crystallographica Section A, 72, pp.385-390.
22. Viezbicke, B.D., Patel, S., Davis, B.E. and Birnie III, D.P., 2015. *Evaluation of the Tauc method for optical absorption edge determination: ZnO thin films as a model system.* physica status solidi (b), 252, pp.1700-1710.
23. Pinaud, B.A., Chen, Z., Abram, D.N. and Jaramillo, T.F., 2011. *Thin films of sodium birnessite-type MnO_2: optical properties, electronic band structure, and solar photoelectrochemistry*. The Journal of Physical Chemistry C, 115, pp.11830-11838.
24. Zhou, L., Zhao, C., Giri, B., Allen, P., Xu, X., Joshi, H., Fan, Y., Titova, L.V. and Rao, P.M., 2016. *High light absorption and charge separation effeciency at low applied voltage from Sb- doped $SnO_2/BiVO_4$ core/shell nanorod-array photoanodes*, Nano Letters, 16, pp. 3463-3474.
25. Zhao, H., Zhang, Y., Li, G., Tian, F., Tang, H. and Chen, R., 2016. *Rhodamine B-sensitized BiOCl hierarchical nanostructure for methyl orange photodegradation*. RSC Advances, 6, pp.7772-7779.
26. Morimoto, T. and Kittaka, S., 1974. *Isoelectric point of manganese oxide*. Bulletin of the Chemical Society of Japan, 47, pp.1586-1588.
27. Konstantinou, I.K. and Albanis, T.A., 2004. *TiO_2-assisted photocatalytic degradation of azo dyes in aqueous solution: kinetic and mechanistic investigations: a review*. Applied Catalysis B: Environmental, 49, pp.1-14.
28. Tsuzuki, T., He, R., Dodd, A. and Saunders, M., 2019. *Challenges in Determining the Location of Dopants, to Study the Influence of Metal Doping on the Photocatalytic Activities of ZnO Nanopowders*. Nanomaterials, 9, p.481.
29. Kroeze, J.E., Savenije, T.J., Vermeulen, M.J. and Warman, J.M., 2003. *Contactless determination of the photoconductivity action spectrum, exciton diffusion length, and charge separation efficiency in polythiophene-sensitized TiO_2 bilayers.* The Journal of Physical Chemistry B, 107, pp.7696-7705.
30. Pesci, F.M., Wang, G., Klug, D.R., Li, Y. and Cowan, A.J., 2013. *Efficient suppression of electron–hole recombination in oxygen-deficient hydrogen-treated TiO_2 nanowires for photoelectrochemical water splitting.* The Journal of Physical Chemistry C, 117, pp.25837-25844.
31. Tang, J., Durrant, J.R. and Klug, D.R., 2008. *Mechanism of photocatalytic water splitting in TiO_2. Reaction of water with photoholes, importance of charge carrier dynamics, and evidence for four-hole chemistry*. Journal of the American Chemical Society, 130, pp.13885-13891.
32. Han, J., Qiu, W. and Gao, W., 2010. *Potential dissolution and photo-dissolution of ZnO thin films*. Journal of Hazardous Materials, 178, pp.115-122.
33. Barka, N., Qourzal, S., Assabbane, A., Nounah, A. and Ait-Ichou, Y., 2010. *Photocatalytic degradation of an azo reactive dye, Reactive Yellow 84, in water using an industrial titanium dioxide coated media.* Arabian Journal of Chemistry, 3, pp.279-283.
34. Cao, G., Su, L., Zhang, X. and Li, H., 2010. *Hydrothermal synthesis and catalytic properties of α- and β-MnO_2 nanorods.* Materials Research Bulletin, 45, pp.425-428.
35. Han, J., Wang, M., Cao, S., Fang, P., Lu, S., Chen, R. and Guo, R., 2013. *Reactive template strategy for fabrication of MnO_2/polyaniline coaxial nanocables and their catalytic application in the oxidative decolorization of rhodamine B.* Journal of Materials Chemistry A, 1, pp.13197-13202.
36. Bernard, S., Chazal, P. and Mazet, M., 1997. *Removal of organic compounds by adsorption on pyrolusite (β-MnO_2).* Water research, 31, pp.1216-1222.
37. Liu, Y., Luo, C., Sun, J., Li, H., Sun, Z. and Yan, S., 2015. *Enhanced adsorption removal of methyl orange from aqueous solution by nanostructured proton-containing δ-MnO_2.* Journal of Materials Chemistry A, 3, pp.5674-5682.
38. Wu, J., Lü, X., Zhang, L., Xia, Y., Huang, F. and Xu, F., 2010. *Crystallinity control on photocatalysis and photoluminescence of TiO_2-based nanoparticles.* Journal of Alloys and Compounds, 496, pp.234-240.
39. Iyer, A., Del-Pilar, J., King'ondu, C.K., Kissel, E., Garces, H.F., Huang, H., El-Sawy, A.M., Dutta, P.K. and Suib, S.L., 2012. *Water Oxidation Catalysis using Amorphous Manganese Oxides, Octahedral Molecular Sieves (OMS-2), and Octahedral Layered (OL-1) Manganese Oxide Structures.* The Journal of Physical Chemistry C, 116, pp.6474-6483.

40. Robinson, D.M., Go, Y.B., Mui, M., Gardner, G., Zhang, Z., Mastrogiovanni, D., Garfunkel, E., Li, J., Greenblatt, M. and Dismukes, G.C., 2013. *Photochemical Water Oxidation by Crystalline Polymorphs of Manganese Oxides: Structural Requirements for Catalysis.* Journal of the American Chemical Society, 135, pp.3494-3501.
41. Zhang, Y., Deng, B., Zhang, T., Gao, D. and Xu, A.W., 2010. *Shape Effects of Cu_2O Polyhedral Microcrystals on Photocatalytic Activity.* The Journal of Physical Chemistry C, 114, pp.5073-5079.
42. Gagrani, A., Ding, B., Wang, Y. and Tsuzuki, T., 2019. *pH dependent catalytic redox properties of Mn_3O_4 nanoparticles*. Materials Chemistry and Physics, 231, pp.41-47.

Chapter 4

Green synthesis and photocatalytic activity of calcium manganese oxide catalysts

Remarks:

This chapter is based on the manuscript under preparation; "Ankita Gagrani, Sara Sousa, Olinda C. Monteiro, Takuya Tsuzuki, "*Green synthesis and photocatalytic activity of calcium manganese oxides catalysts*".

Abstract

This chapter reports the experimental investigation of the synthesis of different calcium manganese oxides nanoparticles ($Ca_2Mn_3O_8$, $CaMn_2O_4$ and $CaMnO_3$) by mechanochemical processing, a potentially green scalable method, and their photocatalytic activities on the decolourization of Rhodamine 6G aqueous solutions. Band gap energies of the three calcium manganese oxides showed their ability to absorb visible light. Valence bands of all the as-synthesized samples were more positive than the electrochemical potential required for the formation of hydroxyl free radicals from water. The photocatalytic activity of the prepared powders, per unit specific surface area, increased in the order $Ca_2Mn_3O_8$ < $CaMnO_3$ < $CaMn_2O_4$.

4.1 Introduction

Photocatalysis has been recognised as an effective tool for many applications in environmental remediation, including pollution reduction in water and air [1]. Among various photocatalytic materials, calcium manganese oxides have emerged as a new class of biomimetic redox catalysts, owing to their earth abundant and environmentally benign elemental constitutions, as well as their structural similarity to the μ-oxo-Mn_4Ca cluster in Photosystem-II protein that is responsible for water-splitting in natural photosynthesis [2-4].

Recently, Khanahmadzadeh *et al*. reported excellent photocatalytic properties of $CaMn_2O_4$ nanoparticles by demonstrating dye degradation under visible light irradiation [5]. Similarly, Barrocas *et al.* reported 83.1% degradation of Rhodamine-6G in 4 hours under visible light irradiation in the presence of $CaMn_3O_6$ nanorods, higher than 63.7% degradation in the presence of immobilized TiO_2 [6]. The photocatalytic properties of doped calcium manganese oxides have also been the subject of recent investigations [7]. However, photocatalytic activity of other calcium manganese oxides, including $CaMnO_3$ and $Ca_2Mn_3O_8$, has not been studied. $Ca_2Mn_3O_8$ is structurally similar to natural OEC [8], and perovskite type materials (ABO_3) have been reported to exhibit excellent photocatalytic abilities [9]. Therefore, it is important to study their photocatalytic properties. In addition, the information critical to these light-driven applications, such as band edge position, is currently lacking.

Further, the reported calcium manganese oxides are often synthesized using solution-based methods such as sol gel [10, 11], hydrothermal [12, 13] and electrospinning [14]. However, the use of organic solutions can pose environmental and health risks. As such, the development of solvent-free chemical processes is imperative for commercial applications of calcium

manganese oxides. The so-called ceramic methods are one of the most commonly used dry synthesis techniques, where nitrates, carbonates, acetates or oxides of calcium and manganese are mixed in stoichiometric quantities to obtain solid solution precursors before heating at elevated temperatures [15-17]. In a recent report, Han *et al.* demonstrated the synthesis of $CaMnO_3$, $Ca_2Mn_3O_8$, $CaMn_2O_4$ and $CaMn_3O_6$ by firing the corresponding $Ca_{1-x}Mn_xCO_3$ (x = 0.5, 0.6, 0.67, and 0.75) solid–solution precursors in air, which resulted in microspheres consisting of aggregated nanoparticles [18]. Similarly, Najafpour *et al.* synthesized spherical $Ca_2Mn_3O_8$ with a typical diameter of 600 nm, by heating the intimately ground mixture of $CaCO_3$ and $MnCO_3$ [19]. It is reported that, in order to achieve high catalytic efficiency, materials with a large surface area and small particle sizes are highly desired, as they provide more active sites to the catalytic process [20]. Therefore, for the photocatalytic applications of calcium manganese oxide, it is of significant importance to develop a solvent free, economical and scalable fabrication method of calcium manganese oxide nanostructures.

Another critical requirement for the commercially viable technology is the scalability of material production processes. Mechanochemical processing has been demonstrated as suitable for the scalable industrial production of novel nanomaterials in a green and economical manner [21]. The key feature of this synthesis approach is to reduce the size of precursor particles in an inert salt matrix to achieve a nanoscopically uniform reaction environment, that in turn enables the formation of uniform nanoparticles within a dry solid matrix while avoiding the involvement of any solvents [22]. The solid phase acts as a physical barrier between nanoparticles during the particle-growth stage, which limits the formation of particle agglomeration. The resulting nanoparticles can be further heat treated while embedded in the solid matrix so as to avoid particle agglomeration.

The present study demonstrates the photocatalytic properties of three different calcium manganese oxides, $Ca_2Mn_3O_8$, $CaMn_2O_4$ and $CaMnO_3$ that are synthesized by mechanochemical processing using a solid-state displacement reaction and subsequent heat treatment. Their bandgap and band-edge positions were also studied to understand their photocatalytic process during dye degradation at neutral pH. The pH was kept neutral in order to avoid reductive dissolution of the samples, as evidenced in the results of Chapter 3.

4.2 Experimental Procedure

4.2.1 Synthesis of $Ca_2Mn_3O_8$

All the chemicals were used without further purification. $Ca_2Mn_3O_8$ nanoparticles were synthesized by first producing $Ca_2Mn_3(CO_3)_5$ nanoparticles by mechanochemical processing and subsequently thermally decomposing the $Ca_2Mn_3(CO_3)_5$ nanoparticles into $Ca_2Mn_3O_8$. $Ca_2Mn_3(CO_3)_5$ nanoparticles were produced via the following reaction:

$$2CaCl_2 + 3MnCl_2 + 5K_2CO_3 + 29KCl \rightarrow Ca_2Mn_3(CO_3)_5 + 39KCl \quad (4.1).$$

Excess KCl salt was added to reduce the volume fraction of $Ca_2Mn_3(CO_3)_5$ in the product phase so as to minimize particle agglomeration [22].

First, a stoichiometric amount of the starting materials $MnCl_2$ (99.9% Sigma Aldrich, 0.996g) and $CaCl_2$ (>93%, granular, anhydrous, Sigma Aldrich, 0.586g) were mixed together in a hardened steel vial for 2 h using a SPEX 8000M mill. Subsequently, 1.823 g of K_2CO_3 (AnalaR NORMAPUR,VWR) and 5.8 g KCl (AnalaR NORMAPUR, VWR) were added in the same

milling vial along with hardened steel balls of 9.2 mm in diameter. The mass ratio of balls-to-powder mass ratio of 10:1 was used. The milling was performed for 4 h in a SPEX 8000M mill to obtain $Ca_2Mn_3(CO_3)_5$ nanoparticles embedded in a KCl salt matrix. The as-milled powders were calcined at 600°C for 1 h in air. Upon cooling the powder, KCl was removed by washing with deionised water (18 MΩ cm), using an ultrasonic bath and a centrifuge, until the total dissolved solid in the supernatant became less than 100 ppm. The powder was dried in an oven at 50°C for several hours.

4.2.2 Synthesis of $CaMnO_3$ and $CaMn_2O_4$

A methodology similar to the one used for the synthesis of $Ca_2Mn_3O_8$ nanoparticles was adopted to produce $CaMnO_3$ and $CaMn_2O_4$ ultrafine particles. The precursor nanoparticles, $CaMn_2(CO_3)_3$ and $CaMn(CO_3)_2$, were mechanochemically produced via the following reactions:

$$CaSO_4 + 2MnSO_4 + 3K_2CO_3 + 11K_2SO_4 \rightarrow CaMn_2(CO_3)_3 + 14K_2SO_4 \quad (4.2),$$

$$CaSO_4 + MnSO_4 + 2K_2CO_3 + 7K_2SO_4 \rightarrow CaMn(CO_3)_2 + 9K_2SO_4 \quad (4.3).$$

During the heat treatment of the as-milled powders, it is crucial for salt matrix to stay in a solid form to avoid particle agglomeration. In reactions (4.2) and (4.3), sulfate salts were used instead of chloride salts (reaction 1), because K_2SO_4 has a higher melting point (1,069°C) than KCl (770°C) and the thermal decomposition of $CaMn_2(CO_3)_3$ and $CaMn(CO_3)_2$ required heat treatment at higher than 770°C.

All chemicals, except $MnSO_4 \bullet 4H_2O$ (99%, metals basis, Alfa Aesar), were used without further purification. $MnSO_4 \bullet 4H_2O$ was dehydrated according to the procedure mentioned elsewhere [23]. First, a stoichiometric amount of $CaSO_4$ (anhydrous, 99%, Alfa Aesar) and $MnSO_4$ were agitated for 2 h. Then, K_2CO_3 (AnalaR NORMAPUR, VWR) and K_2SO_4 (ACS,99.0% min, Alfa Aesar) were added and ball-milled for 4 h. The as-milled powder was heat-treated at 800°C for 3 h, and 950°C for 1 h, for the production of $CaMnO_3$ and $CaMn_2O_4$, respectively. Heat treatment below these temperatures did not yield single phase $CaMnO_3$ and $CaMn_2O_4$. Subsequently, the powder was washed with deionised water and dried.

4.2.3 Physical characterization

The crystal structure of the powders was examined at room temperature using a D_2 Phaser X-ray diffractometer (XRD, Bruker, USA) with Cu-Kα radiation of 1.54059 Å wavelength. The nanostructure and surface morphology of the powder were investigated using a JEOL2100F field emission transmission electron microscope (TEM, JEOL, Japan) at 200 kV, and also an Ultra Plus field-emission scanning electron microscope (FESEM, Zeiss, Germany) at 1 kV. The specific surface area of the nanoparticles was measured by the Brunauer-Emmett-Teller (BET) N_2-gas adsorption method using a TriStar 3020 (Micromeritics, USA). Prior to BET measurements, the powders were degassed under vacuum at 150 °C for 24 h. The bandgap energy of nanoparticles was estimated from UV-Vis optical absorption spectra using a Cary 60 spectrophotometer (Agilent, USA) by measuring transmittance of the samples coated on a quartz plate. The absorption spectra were converted into the Tauc plot of $(h\nu\alpha)^2$ versus $h\nu$, where h is the Planck's constant, ν is the photon's frequency, and α is the optical absorption coefficient. The linear zone of the Tauc curve was extrapolated to the energy axis to estimate the direct bandgap [24].

4.2.4 Dye degradation

Rhodamine-6G (Rh6G) was used as a model organic pollutant to evaluate the photocatalytic free radical generation of calcium manganese oxides. Calcium manganese oxide powder (20 mg) was mixed in a Rh6G aqueous solution (150 mL, 5 ppm) and then stirred in the dark for 1 h to ensure that adsorption equilibrium is reached prior to light irradiation. The suspensions were irradiated with simulated sunlight for up to 3 h. The photocatalytic degradation experiments were conducted using a refrigerated photo-reactor (250 mL). A 450 W Hanovia medium-pressure mercury-vapor lamp was used as a radiation source and a Pyrex cut-off filter was used to remove UV radiation. Several aliquots of ~ 3 mL were taken after certain exposure times from 0 to 180 min. The aliquots were centrifuged, and the supernatant were analyzed by UV-Vis spectroscopy using a Shimadzu UV-2600PC UV−vis spectrophotometer.

4.2.5 Band edge position

To understand the mechanism of photocatalytic dye degradation, the band-edge position of the catalyst needs to be known. Photocurrent measurements were carried out to estimate the band edge positions [25] and charge separation efficiencies of the catalysts [26], according to the procedure mentioned in Chapter 3 (Section 3.2.3).

4.3 Results and Discussions

4.3.1 Synthesis and characterization

Figures 4.1 (a-c) show the XRD patterns of the three starting powder mixtures (Equations 1-3), after milling for 6 h and subsequent removal of the salt matrix phase.

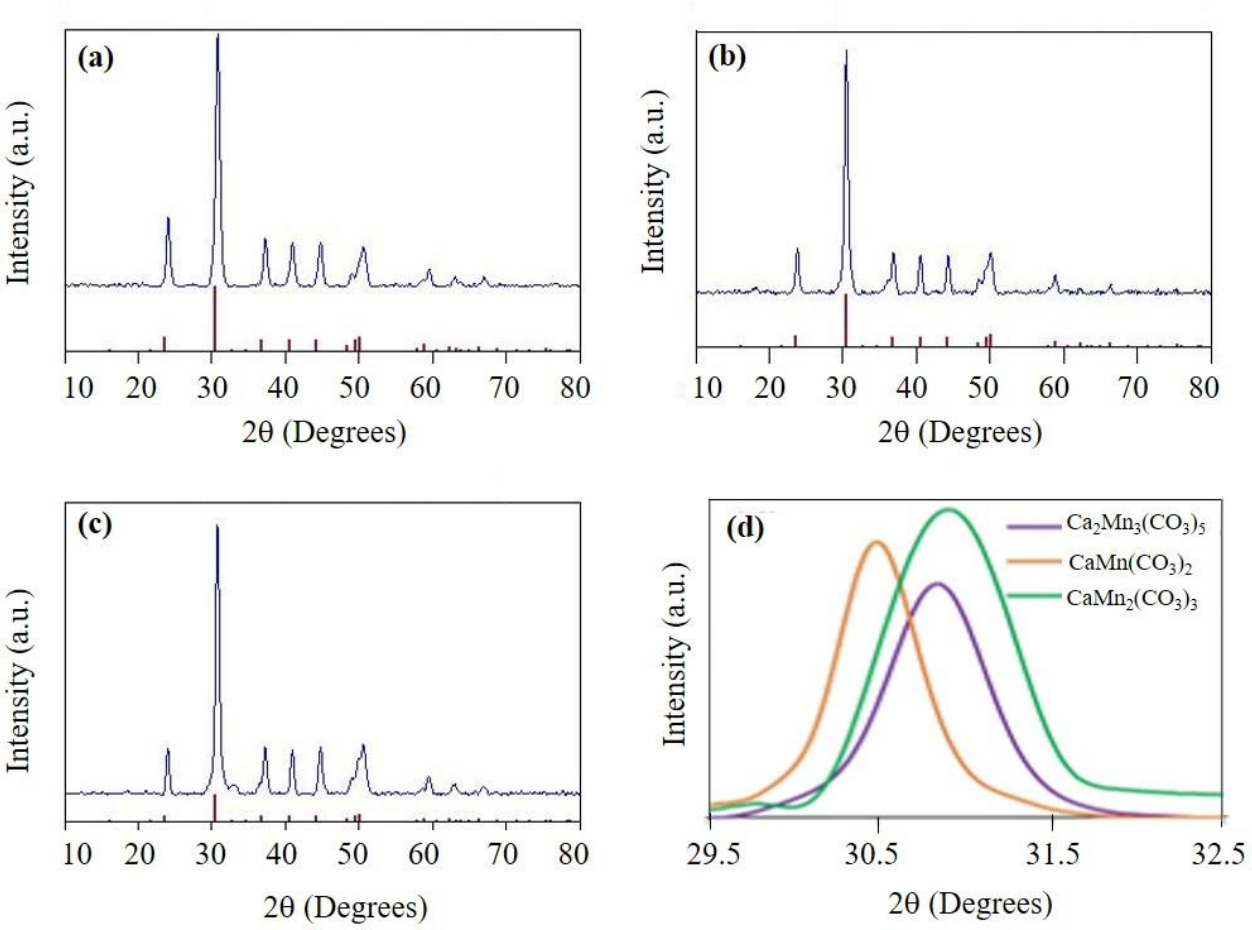

Figure 4.1. XRD patterns of the as-milled powder of (a) $Ca_2Mn_3(CO_3)_5$ precursor, (b) $CaMn(CO_3)_2$ precursor, (c) $CaMn_2(CO_3)_3$ precursor, and (d) comparison of their strongest peaks. The vertical lines at the bottom of (a-c) represent JCPDS # 84-1290 data.

The formation of crystalline $Ca_xMn_y(CO_3)_z$ (JCPDS # 84-1290) is evident, indicating the occurrence of the solid-state displacement reaction during milling. The slight difference in the position of the highest diffraction peak (Figure 4.1d) between $Ca_2Mn_3(CO_3)_5$, $CaMn_2(CO_3)_3$ and $CaMn(CO_3)_2$ could be attributed to different Mn/Ca ratios in the samples, due to the difference in ionic radii of Mn and Ca [18]. Figures 4.2 (a-c) show the XRD patterns of the powders after heat treatment and subsequent removal of the salt matrix phase. The diffraction peaks can be indexed to (a) $Ca_2Mn_3O_8$ (JCPDS # 73-2290), (b) $CaMnO_3$ (JCPDS # 89-0666) and (c) $CaMn_2O_4$ (JCPDS # 74-2293), respectively, confirming the formation of crystalline calcium manganese oxides.

Figures 4.3 (a-c) show the SEM images of $Ca_xMn_y(CO_3)_z$ precursor powders. It is evident in the image that precursor particles with primary particle sizes of 20-40 nm were produced. After heat treatment to decompose carbonate precursors into $Ca_2Mn_3O_8$, nano-scale particles of 30-100 nm in diameter were obtained (Figure 4.3g). The morphology of the particles became plate-like as shown in Figure 4.3d. On the other hand, $CaMnO_3$ particles had cuboidal shapes, with sizes ranging between 50 and 200 nm (Figures 4.3e, 4.3h). Compared to the direct calcination of a mixture of $CaCO_3$ and $MnCO_3$ [18, 19], mechanochemical processing and subsequent heat treatment resulted in significantly smaller particles sizes of $Ca_2Mn_3O_8$ and $CaMnO_3$. In contrast to $Ca_2Mn_3O_8$ and $CaMnO_3$, mechanochemical processing and subsequent heat treatment did not lead to the formation of nanoscale $CaMn_2O_4$ particles (Figures 4.3f, 4.3i). The resulting particles were irregular in shape with sizes from 200 nm to 2 μm. The large particle sizes of $CaMn_2O_4$ can be attributed to the higher temperature required to decompose the carbonate precursors. In high-resolution TEM images, all oxides showed high crystallinity with clear distinguished lattice fringes (Figures 4.3j-l).

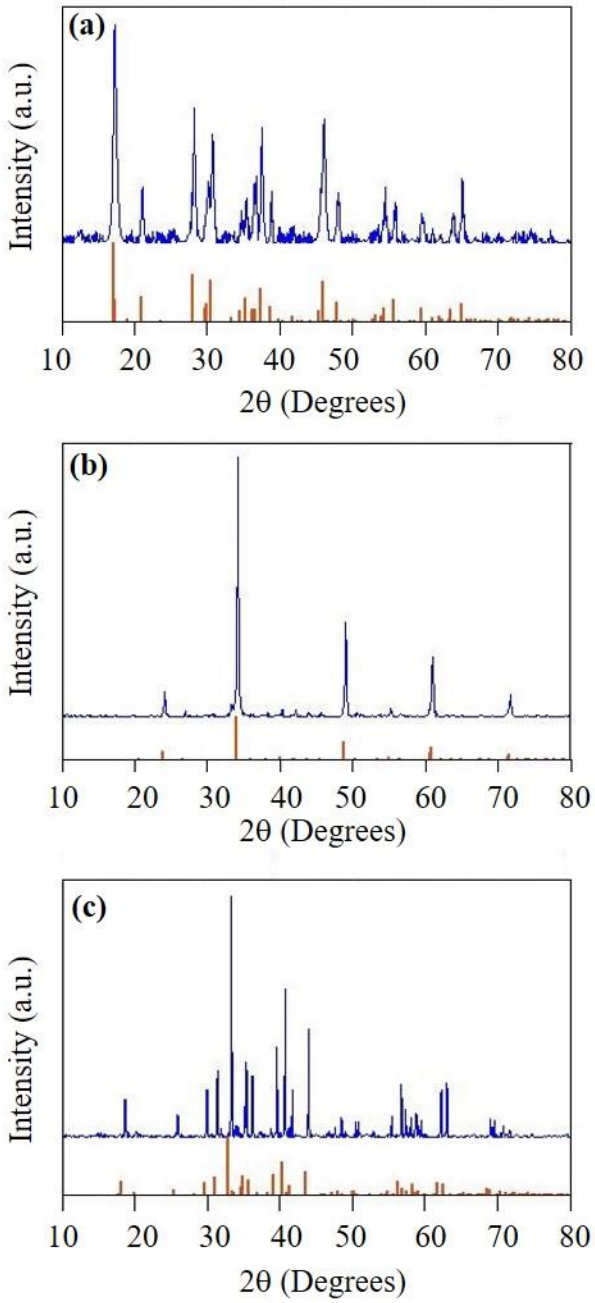

Figure 4.2. XRD patterns of (a) $Ca_2Mn_3O_8$, (b) $CaMnO_3$, and (c) $CaMn_2O_4$. The vertical lines at the bottom of (a-c) represent JCPDS #73-2290, #89-0666 and #74-2293 data, respectively.

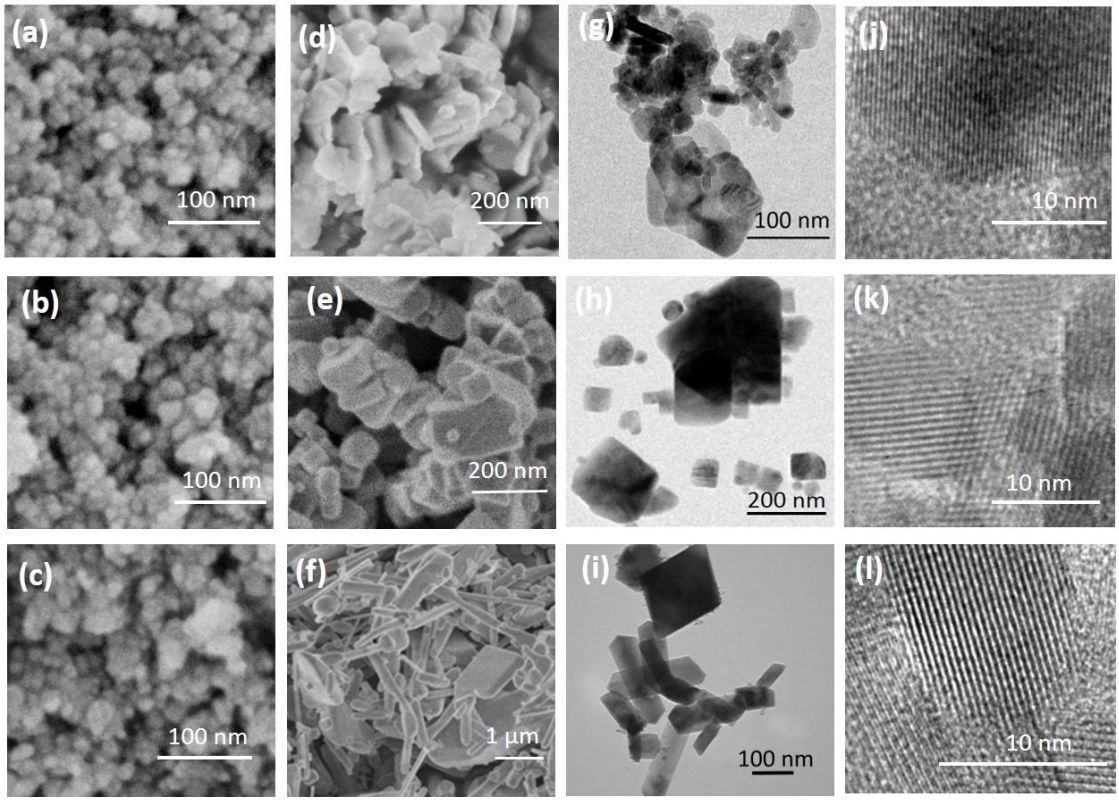

Figure 4.3. SEM micrographs of (a) $Ca_2Mn_3(CO_3)_5$ precursor, (b) $CaMn(CO_3)_2$ precursor, (c) $CaMn_2(CO_3)_3$ precursor, (d) $Ca_2Mn_3O_8$ powder, (e) $CaMnO_3$ powder, and (f) $CaMn_2O_4$ powder; high-resolution TEM micrographs of (g,j) $Ca_2Mn_3O_8$, (h,k) $CaMnO_3$, and (i,l) $CaMn_2O_4$.

The BET specific surface areas of the calcium manganese oxide powders are listed in Table 4.1, along with the theoretical densities estimated from the crystal structure and the corresponding average spherical particle sizes calculated using the following formula:

$$d = \frac{6000}{\rho \bullet S} \qquad (4.4),$$

where ρ is the density [gcm^{-3}] and S is the specific surface area [m^2g^{-1}]. Although the morphologies of $Ca_2Mn_3O_8$, $CaMnO_3$ and $CaMn_2O_4$ were not spherical, the average spherical particle sizes estimated from the specific surface area were in good agreement with the SEM and TEM studies, implying that the particles were not porous and had a low degree of agglomeration [27]. The BET specific surface areas of $Ca_2Mn_3O_8$ and $CaMnO_3$ powders were 14 times and 5 times higher than that of $Ca_2Mn_3O_8$ and $CaMnO_3$ powders synthesised using ceramic methods [19].

Table 4.1. BET specific surface area, theoretical density and corresponding average spherical particle size.

Compound	**Specific surface area (m^2g^{-1})**	**Theoretical density (gcm^{-3})**	**Corresponding average spherical particle size (nm)**
$Ca_2Mn_3O_8$	48.5	4.13	30.0
$CaMnO_3$	13.8	4.59	94.7
$CaMn_2O_4$	4.7	4.60	278

Figure 4.4 shows the Tauc plot in the form of $(\alpha hv)^2$ versus hv for $Ca_2Mn_3O_8$, $CaMnO_3$ and $CaMn_2O_4$. The Tauc plot was made from the transmittance spectra shown in Figure 4.5. The intercept of the straight line with the x-axis (energy axis) indicates an optical direct bandgap energy of 2.1 eV, 1.5 eV and 1.5 eV for $Ca_2Mn_3O_8$, $CaMnO_3$ and $CaMn_2O_4$, respectively. These values are in good agreement with the previously reported values: ~2.3 eV for $Ca_2Mn_3O_8$ [11, 28], ~1.4 eV for $CaMnO_3$ [27], and 1.94 eV and 1.4 eV for bulk and nano $CaMn_2O_4$, respectively [5].

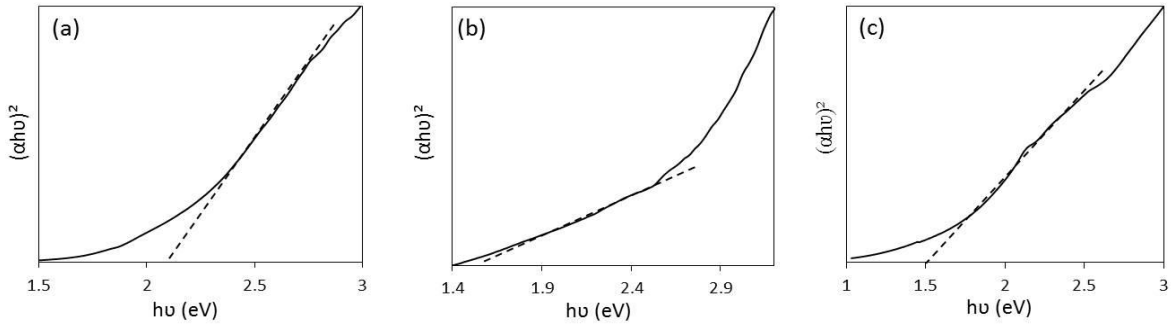

Figure 4.4. Tauc plots of (a) $Ca_2Mn_3O_8$, (b) $CaMnO_3$ and (c) $CaMn_2O_4$.

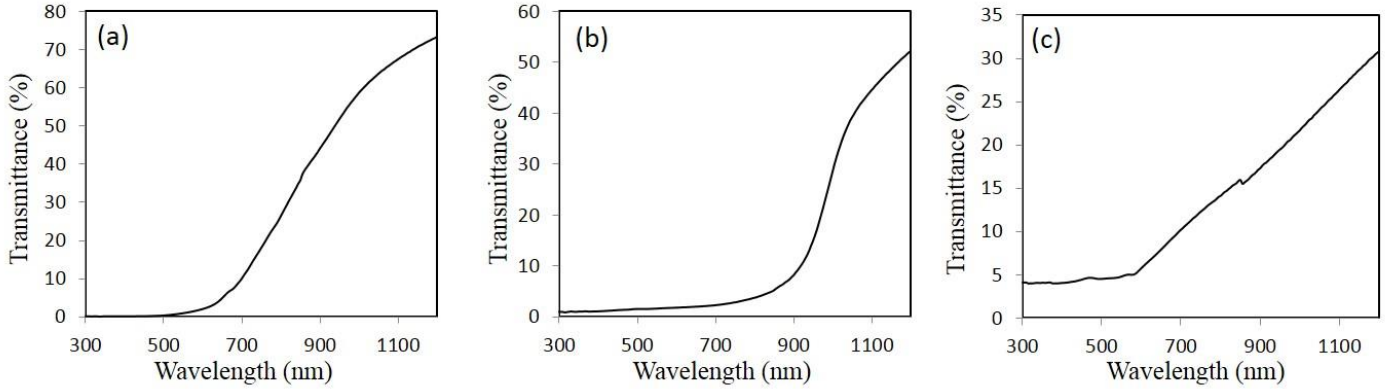

Figure 4.5. UV-vis transmittance spectra of (a) $Ca_2Mn_3O_8$, (b) $CaMnO_3$, and (c) $CaMn_2O_4$.

4.3.2 Photocatalytic degradation of Rh6G

The optical absorption spectra of the Rh6G solutions during light irradiation (Figure 4.6) showed that $CaMn_2O_4$ and $CaMnO_3$ induced photocatalytic decomposition of Rh6G decomposition, while $Ca_2Mn_3O_8$ did not. Without addition of any catalytic powder, 32% of the dye was decolorized within 3 h. The addition of $Ca_2Mn_3O_8$ did not increase the dye decolourization upon 3 h of light irradiation. On the other hand, the presence of $CaMn_2O_4$ and $CaMnO_3$ resulted in 61% and 62% degradation of the dye, respectively, within the same irradiation time.

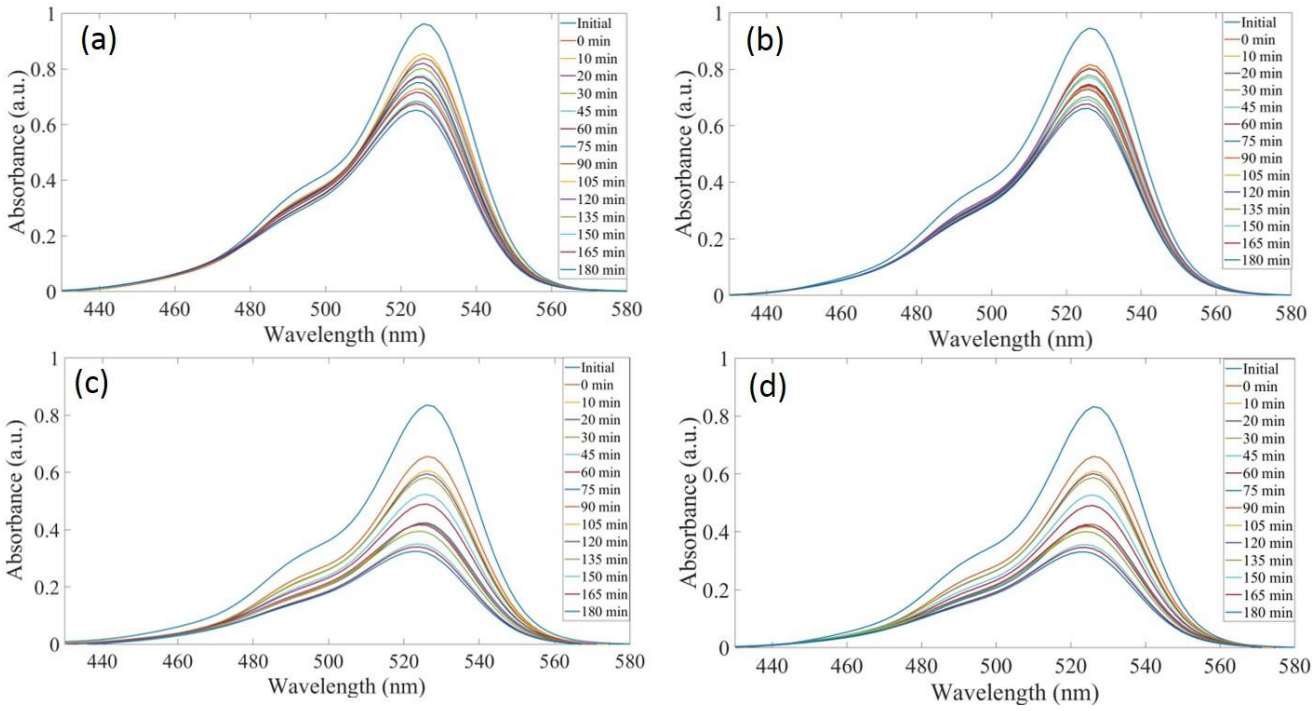

Figure 4.6. Exposure time profiles of UV-Vis absorbance spectra of Rhodamine-6G solutions under simulated sunlight in the presence of (a) no catalyst (photolysis) (b) $Ca_2Mn_3O_8$, (c) $CaMnO_3$, and (d) $CaMn_2O_4$.

The kinetic of this catalytic process followed the first order process. Figures 4.7a shows the Rh6G degradation rates upon light irradiation in the presence of $Ca_2Mn_3O_8$, $CaMn_2O_4$ and $CaMnO_3$ and direct photolysis without oxides. In the y-axis of Figure 4.7a, C is the absorbance value of the dye solution at each irradiation time at the wavelength of 526 nm, and C_0 is the absorbance value at the same wavelength before irradiation. The errors on data points in Figure 4.7a, +2.2% and -0.7%, were estimated by repeating measurements 3 times.

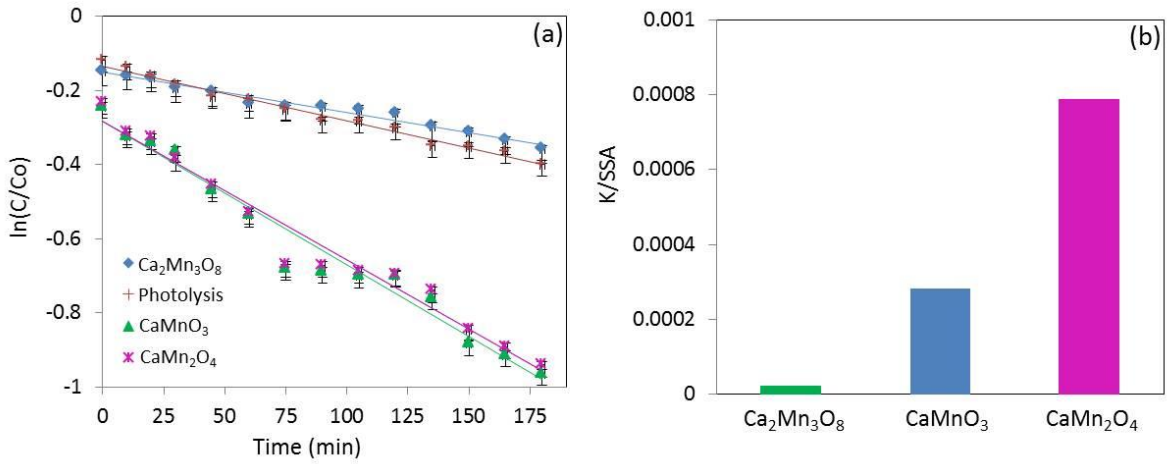

Figure 4.7. (a) Rh6G degradation rates under light irradiation with and without catalysts; (b) Dye-degradation rate constant normalised with specific surface area.

The results confirm that $Ca_2Mn_3O_8$ exhibited no photocatalytic activity for Rh6G degradation. The photocatalytic activities of $CaMn_2O_4$ and $CaMnO_3$ were nearly identical to each other. However, $CaMn_2O_4$ and $CaMnO_3$ powders have different specific surface areas, 4.7 and 13.8 m^2g^{-1}, respectively. In order to separate the effect of surface area from other factors in the photocatalytic activity, dye-degradation rate constants per unit specific surface area, *K*, were calculated using the following equation:

$$K = \frac{k}{S} = \frac{-\ln\frac{C}{C_0}}{t \cdot S} \qquad (4.5),$$

where *k* (min^{-1}) is the first-order degradation rate constant, *t* (min) is the irradiation time and *S* ($m^2 \cdot g^{-1}$) is the BET specific surface area. As shown in Figure 4.7b, $CaMn_2O_4$ showed a much higher *K* value than $CaMnO_3$, indicating that, as a material, $CaMn_2O_4$ is superior to $CaMnO_3$ as a photocatalyst for Rh6G degradation.

To better understand the role of the catalyst during photo-activated dye degradation, the species involved in the dye degradation process were investigated using $CaMnO_3$. The usual photo-generated oxidant radicals, active in the photocatalytic degradation reactions, are the hydroxyl radical ($^{\bullet}OH$), superoxide radical ($O_2^{\bullet-}$) and positive holes (h^+). In order to identify the dominant radical species that is photo-generated to participate in the dye degradation process, scavengers of such species were added to the reaction media before light irradiation. The radical scavengers used were ethanol as a $^{\bullet}OH$ scavenger, potassium oxalate as a hole scavenger and *p*-benzoquinone as a $O_2^{\bullet-}$ scavenger.

The effect of these scavengers in the Rh6G photo-degradation process, after 90 min of irradiation, is shown in Figure 4.8. When $^{\bullet}OH$ scavenger was introduced into the system together with the catalyst, the amount of degraded dye was comparable with that of direct photolysis without catalysts. A similar result was obtained with the hole scavenger. The results demonstrate that photo-induced hydroxyl radicals and holes were responsible for the dye degradation, thus showing the photocatalytic nature of $CaMnO_3$. It is understood that holes are not directly involved in the decomposition of the dye, but holes induced the generation of hydroxyl radicals through the reaction $H_2O/OH^- + h^+ = {}^{\bullet}OH$ [29]. The addition of $O_2^{\bullet-}$ scavenger resulted in a higher amount of dye degradation. This may be attributed to the oxidizing nature of *p*-benzoquinone [30]; the addition of oxidizing species has been known to increases the rate of photo-oxidation [31]. Nonetheless, the result suggests that superoxide is not the main species responsible for the photo-induced Rh6G degradation by calcium manganese oxides.

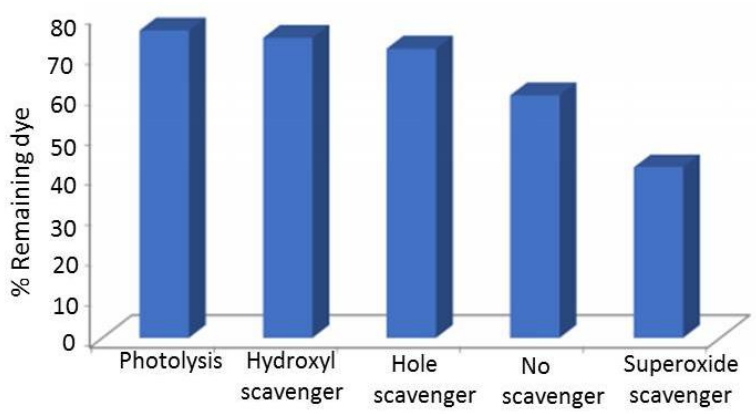

Figure 4.8. The magnitude of photo-degradation of Rh6G after 90 min of irradiation, in the presence of several radical scavengers and $CaMnO_3$ photocatalyst.

In order to photo-generate $^{\bullet}OH$ free radicals, the top of the valence band should be more positive than the electrochemical potential of the reaction $OH^- + h^+ = {}^{\bullet}OH$ (+1.99 V *vs* NHE at pH =7). To confirm this, the band-edge positions of the $Ca_xMn_yO_z$ materials were estimated using the photocurrent onset method, as shown in Figure 4.9. The lower edge of the conduction band at pH 7 was determined for $Ca_2Mn_3O_8$, $CaMn_2O_4$ and $CaMnO_3$ as 0.47, 0.6 and 0.51 eV, respectively. By using the measured band-edge positions and bandgap energies, the schematic energy-level diagram of $Ca_xMn_yO_z$ is presented in Figure 4.10, with respect to the electrochemical potentials of $O_2 + e^- = O_2^{\bullet-}$ and $OH^- + h^+ = {}^{\bullet}OH$ at pH 7. The highest occupied molecular orbital (HOMO) and lowest unoccupied molecular orbital (LUMO) energy levels of Rh6G are also given in Figure 4.10 [32].

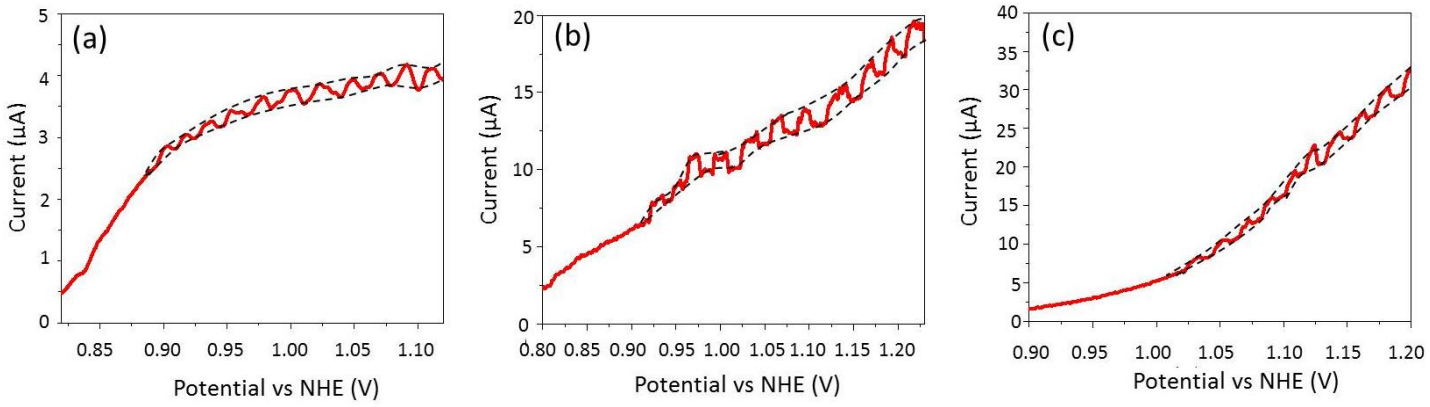

Figure 4.9. Current potential curve (at 0.1 mV/s) of (a) $Ca_2Mn_3O_8$, (b) $CaMnO_3$, (c) $CaMn_2O_4$ under chopped illumination. The potential vs NHE at pH 0 is shown.

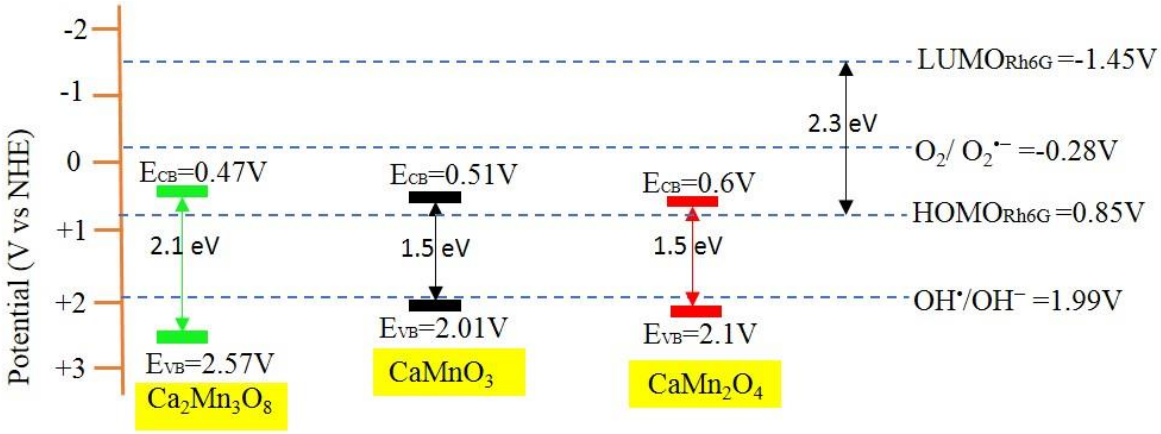

Figure 4.10. Schematic energy level diagram of $Ca_2Mn_3O_8$, $CaMn_2O_4$ and $CaMnO_3$ with respect to the electrochemical potentials of O_2/ $O_2^{\bullet-}$ and $OH^{\bullet}/OH^-$ at pH 7.

It is evident that the position of conduction band edge is more positive in electrochemical potential than that of $O_2/O_2^{\bullet-}$ for $Ca_2Mn_3O_8$, $CaMn_2O_4$ and $CaMnO_3$, so that the photo-generation of $O_2^{\bullet-}$ was not possible. On the other hand, the positions of the valence band edge of all three catalysts are more positive in electrochemical potential than that of $OH^{\bullet}/OH^-$ (1.99 eV), implying the formation of $^{\bullet}OH$ radicals through hole donation. This configuration makes hydroxyl radicals

responsible for the dye degradation. This is in good agreement with the study of the species involved in the R6G degradation process (Figure 4.8).

The bandgap energy and valence band position indicate that all the three compounds should act as photo-catalysts for the dye degradation reaction. However, the photocatalytic activity of $Ca_2Mn_3O_8$ was almost negligible, despite its highest surface area among all tested $Ca_xMn_yO_z$ powders.

To explain the reason for negligible photocatalysis in the presence of $Ca_2Mn_3O_8$, charge separation efficiencies of all the catalysts were calculated using Equation (3.1). The measured J_{max} value was 9.8 mA cm^{-2}. η_{abs} calculated using LHE curves (as shown in Figure 4.11) were 87%, 87% and 64% for $Ca_2Mn_3O_8$, $CaMnO_3$ and $CaMn_2O_4$, respectively. J_{H_2O} was in the range of µA cm^{-2} (Figure 4.12), even when the charge transfer efficiency was close to 100% and absorption efficiency was reasonable, demonstrating poor charge separation efficiency of all the three photocatalyst. Figure 4.13 shows the charge separation efficiency of the three catalyst at different voltage. In the figure, charge separation efficiency is only defined at 4 voltage points, because the signal-to-noise ratio in observed photocurrent (as shown in Figure 4.12) was relatively poor, making it difficult to calculate photocurrent across a wide range of voltage. To take into consideration the errors in photocurrent measurements, error bars are indicated in Figure 4.13. As evident in Figure 4.13, among three catalysts, $Ca_2Mn_3O_8$ demonstrated lowest charge separation efficiency, explaining its poor photocatalysis during dye degradation.

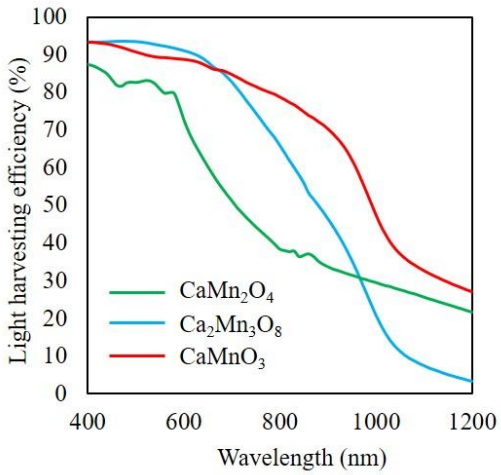

Figure 4.11. Light harvesting efficiency of (a) $Ca_2Mn_3O_8$, (b) $CaMnO_3$, and (c) $CaMn_2O_4$.

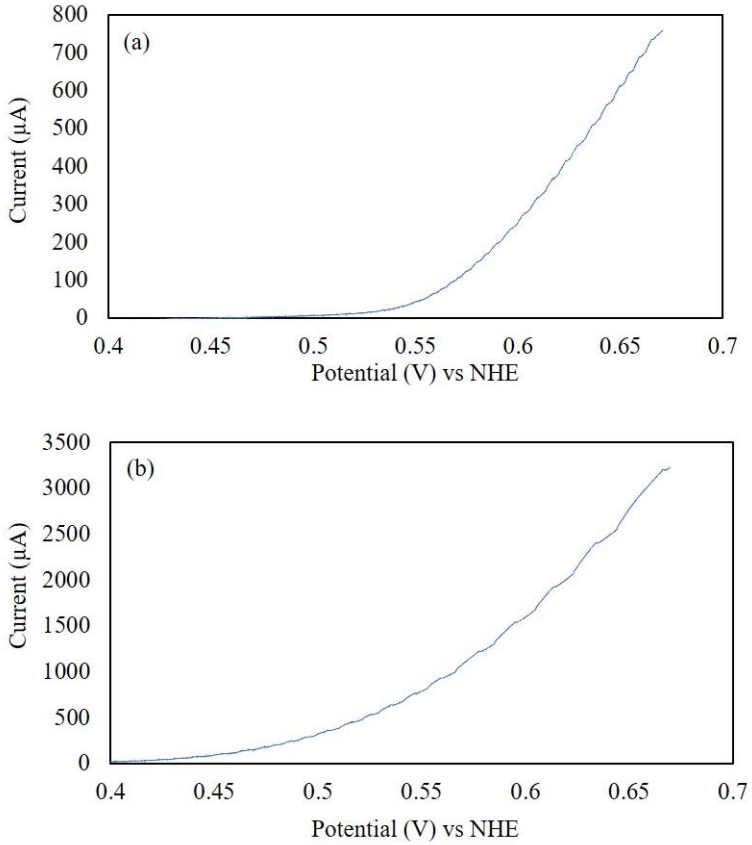

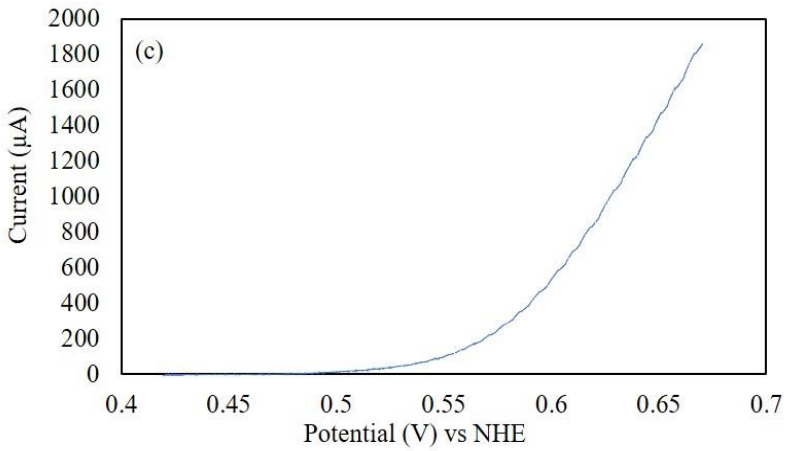

Figure 4.12. Current potential curve (at 1 mV/s) of (a) $Ca_2Mn_3O_8$, (b) $CaMnO_3$, (c) $CaMn_2O_4$ under chopped illumination (at pH 7) in the presence of sodium sulphite electrolyte.

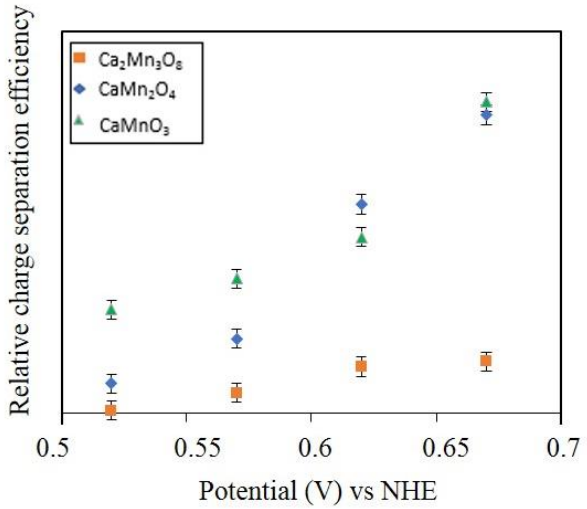

Figure 4.13. Relative charge separation efficiency of $Ca_2Mn_3O_8$, $CaMn_2O_4$ and $CaMnO_3$.

Another reason for the lower photocatalytic activity of $Ca_2Mn_3O_8$ could be due to the large bandgap energy of $Ca_2Mn_3O_8$ compared to $CaMn_2O_4$ and $CaMnO_3$, leading to lower photon-capture efficiency of $Ca_2Mn_3O_8$ than that of $CaMn_2O_4$ and $CaMnO_3$ and in turn contributing to the lower photocatalytic activity of $Ca_2Mn_3O_8$.

In Figure 4.10, the positions of HOMO and LUMO of Rh6G suggest that Rh6G will photo-sensitise calcium manganese oxides. In this situation, the dye could be involved in its own degradation, by forming photo-activated electrons and holes then injecting electrons from LUMO of the dye to the conduction band of calcium manganese oxides, which creates unstable dye molecules subjected to direct oxidation/reduction by the excited catalyst [33]. Despite this, different calcium manganese oxide showed different abilities to degrade the dye. This could be attributed to the type of interaction between the dye and the catalysts [34]. The fact that sensitization or direct oxidation/reduction involves charge transfer from dye molecules to the catalysts or vice-versa, implies that adsorption of dye molecules on the surface of catalyst particles plays a significant role in the process [34]. In the past, theoretical density functional theory (DFT) studies have shown that different Ca–Mn–O compounds have different adsorption configurations and strength, possibly resulting in different photocatalytic strength [18]. Therefore, the variation in the strength and type of interaction between the dye and Ca-Mn-O compounds may be also a reason for different efficiency of the dye degradation process.

Nonetheless, all the three calcium manganese oxides demonstrated the potential to absorb visible light and act as a photocatalyst, with band edge positions suitable for oxygen generation through water splitting. Only few reports have been published on the catalysis, surface chemistry and role of calcium, in calcium manganese oxides to date and further efforts are required to gain a full understanding of their photocatalytic mechanism.

4.4 Chapter summary

In the present chapter, $Ca_2Mn_3O_8$, $CaMn_2O_4$ and $CaMnO_3$ ultrafine particles were successfully synthesized in two steps, mechanochemical processing and subsequent heat treatment. In the

first step, a solid-state displacement reaction resulted in the formation of $Ca_xMn_{1-x}CO_3$ nanoparticles. The second step involved the thermal decomposition of $Ca_xMn_{1-x}CO_3$ nanoparticles into $Ca_xMn_{1-x}O_y$. During the heat treatment, particles were embedded within the solid salt matrix that acted as a physical barrier between nanoparticles, which prevented particles from agglomerating, and resulted in an improved surface area of calcium manganese oxides particles.

For the different calcium manganese oxides, band position analysis demonstrated the suitability of all three Ca-Mn-O compounds in photo-assisted dye degradation. However, despite the low surface areas, $CaMn_2O_4$ and $CaMnO_3$ showed higher photocatalytic activity than $Ca_2Mn_3O_8$ due to difference in intrinsic properties of the compounds. The results are of particular importance to developing calcium manganese oxide photo-catalysts suitable for energy and environment related applications such as water splitting, which will be investigated in chapter 5.

4.5 References

1. Kabra, K., Chaudhary, R. and Sawhney, R.L., 2004. *Treatment of Hazardous Organic and Inorganic Compounds through Aqueous-Phase Photocatalysis: A Review*. Industrial & Engineering Chemistry Research, 43, pp.7683-7696.
2. Najafpour, M.M., 2011. *Mixed-valence manganese calcium oxides as efficient catalysts for water oxidation*. Dalton Transactions, 40, pp.3793-3795.
3. Rong, F., Zhao, J., Chen, Z., Xu, Y., Zhao, Y., Yang, Q. and Li, C., 2016. *Highly active water oxidation on nanostructured biomimetic calcium manganese oxide catalysts*. Journal of Materials Chemistry A, 4, pp.6585-6594.
4. Najafpour, M.M., Nayeri, S. and Pashaei, B., 2011. *Nano-size amorphous calcium-manganese oxide as an efficient and biomimetic water oxidizing catalyst for artificial photosynthesis: back to manganese*. Dalton Transactions, 40, pp.9374-9378.
5. Khanahmadzadeh, S., Mikaeili, N. and Hasanpour, S., 2017. *Facile synthesis of $CaMn_2O_4$ nanoparticles and investigation of photocatalytic activity, optical and magnetic properties and its influence on the thermal stability of polymeric nanocomposite*. Journal of Materials Science: Materials in Electronics, 28, pp.4521-4529.
6. Barrocas, B., Sério, S., and Jorge, M.M., 2014. *Hierarchically Grown $CaMn_3O_6$ Nanorods by RF Magnetron Sputtering for Enhanced Visible-Light-Driven Photocatalysis.* The Jounal of Physical Chemistry C, 118, pp.24127-24135.
7. Barrocas, B., Sério, S., Rovisco, A., Nunes, Y. and Jorge, M.M., 2016. *Removal of rhodamine 6G dye contaminant by visible light driven immobilized $Ca_{1-x}Ln_xMnO_3$ (Ln= Sm, Ho; 0.1< x< 0.4) photocatalysts*. Applied Surface Science, 360, pp.798-806.
8. Gagrani, A. and Tsuzuki, T., 2019. *Calcium manganese oxides as biomimetic catalysts in energy applications: A short review*. Chemical Engineering Science, 194, pp.116-126.
9. Gupta, S., Kellogg, W., Xu, H., Liu, X., Cho, J. and Wu, G., 2016. *Bifunctional perovskite oxide catalysts for oxygen reduction and evolution in alkaline media.* Chemistry–An Asian Journal, 11, pp.10-21.
10. Kim, J., Yin, X., Tsao, K.-C., Fang, S. and Yang, H., 2014. *$Ca_2Mn_2O_5$ as oxygen-deficient perovskite electrocatalyst for oxygen evolution reaction*. Journal of the American Chemical Society, 136, pp.14646-14649.
11. Ramírez, A., Bogdanoff, P., Friedrich, D. and Fiechter, S., 2012. *Synthesis of $Ca_2Mn_3O_8$ films and their electrochemical studies for the oxygen evolution reaction (OER) of water*. Nano Energy, 1, pp.282-289.
12. Najafpour, M.M., Ehrenberg, T., Wiechen, M. and Kurz, P., 2010. *Calcium Manganese(III) Oxides ($CaMn_2O_4 \cdot x\,H_2O$) as Biomimetic Oxygen-Evolving Catalysts*. Angewandte Chemie International Edition, 49, pp.2233-2237.
13. Arnold, D.C., Kazakova, O., Audoit, G., Tobin, J.M., Kulkarni, J.S., Nikitenko, S., Morris, M.A. and Holmes, J.D., 2007. *The Synthesis and Characterisation of Ferromagnetic $CaMn_2O_4$ Nanowires*. ChemPhysChem, 8, pp.1694-1700.
14. Nakhowong, R., 2016. *Preparation and characterization of calcium manganese oxide ($CaMnO_3$) nanofibers by electrospinning*. Materials Letters, 163, pp.222-225.
15. Hadermann, J., Abakumov, A.M., Gillie, L.J., Martin, C. and Hervieu, M., 2006. *Coupled Cation and Charge Ordering in the $CaMn_3O_6$ Tunnel Structure*. Chemistry of Materials, 18, pp.5530-5536.
16. White, B.D., dos Santos, C.A.M., Souza, J.A., McClellan, K.J. and Neumeier, J.J., 2008. *Crystal growth and characterization of Marokite $CaMn_2O_{4+\delta}$.* Journal of Crystal Growth, 310, pp.3325-3330.
17. Melo Jorge, M.E., Correia dos Santos, A. and Nunes, M.R., 2001. *Effects of synthesis method on stoichiometry, structure and electrical conductivity of $CaMnO_{3-\delta}$.* International Journal of Inorganic Materials, 3, pp.915-921.

18. Han, X., Zhang, T., Du, J., Cheng, F. and Chen, J., 2013. *Porous calcium-manganese oxide microspheres for electrocatalytic oxygen reduction with high activity*. Chemical Science, 4, pp.368-376.
19. Najafpour, M.M., Pashaei, B. and Nayeri, S., 2012, *Calcium manganese (IV) oxides: biomimetic and efficient catalysts for water oxidation*. Dalton Transactions, 41, pp.4799-4805.
20. Li, G.J., Zhang, X.H. and Kawi, S., 1999. *Relationships between sensitivity, catalytic activity, and surface areas of SnO_2 gas sensors*. Sensors and Actuators B: Chemical, 60, pp.64-70.
21. Tsuzuki, T. and McCormick, P.G., 2004. *Mechanochemical synthesis of nanoparticles*. Journal of Materials Science, 39, pp.5143-5146.
22. Tsuzuki, T. and McCormick, P., 2000. *Synthesis of Cr_2O_3 nanoparticles by mechanochemical processing*. Acta Materialia, 48, pp. 2795-2801.
23. Sinha, S.G., Deshpande, N.D. and Deshpande, D.A., 1987. *Dehydration of crystalline $MnSO_4 \cdot 4H_2O$*. Thermochimica Acta, 113, pp.95-104.
24. Viezbicke, B.D., Patel, S., Davis, B.E. and Birnie, D.P., 2015. *Evaluation of the Tauc method for optical absorption edge determination: ZnO thin films as a model system*. Physica Status Solidi B, 252, pp.1700-1710.
25. Pinaud, B.A., Chen, Z., Abram, D.N. and Jaramillo, T.F., 2011. *Thin films of sodium birnessite-type MnO_2: optical properties, electronic band structure, and solar photoelectrochemistry*. The Journal of Physical Chemistry C, 115, pp.11830-11838.
26. Zhou, L., Zhao, C., Giri, B., Allen, P., Xu, X., Joshi, H., Fan, Y., Titova, L.V. and Rao, P.M., 2016. *High light absorption and charge separation effeciency at low applied voltage from Sb- doped $SnO_2/BiVO_4$ core/shell nanorod-array photoanodes*, Nano Letters, 16, pp. 3463-3474.
27. Tsuzuki, T. and McCormick, P.G., 2001. *Synthesis of ultrafine ceria powders by mechanochemical processing*. Journal of the American Ceramic Society, 84, pp.1453-1458.
28. Shinde, A., Suram, S.K., Yan, Q., Zhou, L., Singh, A.K., Yu, J., Persson, K.A., Neaton, J.B. and Gregoire, J.M., 2017. *Discovery of manganese-based solar fuel photoanodes via integration of electronic structure calculations, pourbaix stability modeling, and high-throughput experiments*. ACS Energy Letters, 2, pp.2307-2312.
29. Ravelli, D., Dondi, D., Fagnoni, M. and Albini, A., 2009. *Photocatalysis. A multi-faceted concept for green chemistry.* Chemical Society Reviews, 38, pp.1999-2011.
30. March, J., 1992. *Advanced organic chemistry: reactions, mechanisms, and structure*. John Wiley & Sons.
31. Ajmal, A., Majeed, I., Malik, R.N., Idriss, H. and Nadeem, M.A., 2014. *Principles and mechanisms of photocatalytic dye degradation on TiO_2 based photocatalysts: a comparative overview*. Rsc Advances, 4, pp.37003-37026.
32. Deng, S., Xu, W., Wang, J., Ling, X., Wu, J., Xie, L., Kong, J., Dresselhaus, M.S. and Zhang, J., 2014. *Direct measurement of the Raman enhancement factor of rhodamine 6G on graphene under resonant excitation*. Nano Research,7, pp.1271-1279.
33. Pingmuang, K., Chen, J., Kangwansupamonkon, W., Wallace, G.G., Phanichphant, S. and Nattestad, A., 2017. *Composite photocatalysts containing $BiVO_4$ for degradation of cationic dyes*. Scientific reports, 7, p.8929.
34. Rochkind, M., Pasternak, S. and Paz, Y., 2015. *Using dyes for evaluating photocatalytic properties: a critical review*. Molecules, 20, pp.88-110.

Chapter 5

Photo-electrochemical oxygen evolution by manganese-based oxides

Remarks:

This chapter is based on the manuscript under preparation; "Ankita Gagrani, Mohammed Alsultan, Gerhard Swiegers, Takuya Tsuzuki, "*Photo-electrochemical oxygen evolution reaction by manganese-based oxides*".

Abstract

In recent years, manganese-based oxides, particularly calcium manganese oxides, have attracted significant practical interest as a new class of catalysts, due to their elemental and structural similarity to the natural oxygen evolving cluster (OEC) in plant cells. In Chapters 3 and 4, green synthesis of different manganese and calcium manganese oxides was demonstrated, and preliminary study of their photocatalytic activities was reported. In this chapter, oxygen evolution performance of these manganese-based materials has been investigated in a photo-electrochemical cell. The difference in their performance was discussed based on manganese oxidation state, crystal structure, specific surface area, presence of calcium and structural similarities to the natural OEC. The results indicate that there may be some possible importance of having a local structure similar to that of the natural OEC cubane including the presence of Ca, but the study also highlighted the problems in talking the simplistic approach in focusing on the local structure alone.

5.1 Introduction

Photosynthesis, nature's solar technology, is the most efficient water-splitting system known to date. Recently, it was identified that $CaMn_4O_5$ clusters, situated within the Photosystem-II proteins in plant cells, are the key structural component for the light-driven natural water-splitting [1]. The natural oxygen evolving cluster (OEC) has an asymmetrical cubane-like structure that, resembles a distorted chair [2]. In the cubane, a calcium and three manganese ions formed four corners and remaining four corners were occupied by four oxygen atoms. Fourth dangling manganese ion is outside the cubane and is linked to two manganese ions within the cubane by one oxygen, and the fifth oxygen by a di-μ-oxo bridge (Figure 5.1).

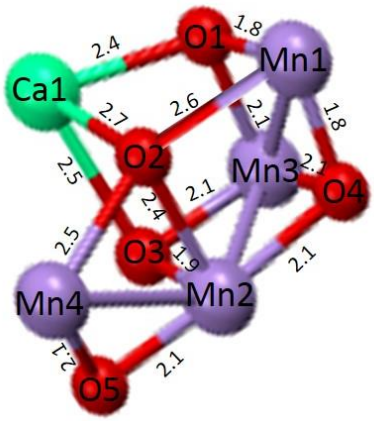

Figure 5.1. Structure the Mn_4CaO_5 cluster with distances (in ångströms) between different atoms. Calcium in green; manganese in blue; oxygen in red.

A computational study showed that two water molecules are bound to calcium and dangling manganese and play a key role in the water-splitting process; thus, the atomic arrangement of the Mn_4Ca cubane is thought to be critical to the natural water splitting [3]. This discovery inspired scientists to investigate the synthesis and water splitting efficiencies of several

manganese-based oxides, in particular calcium manganese oxides, in order to artificially split water using solar energy to produce a clean fuel, hydrogen [4].

For example, Baktash *et al.* reported the synthesis and chemical water oxidation of porous calcium-manganese oxides with a unique foam-like nanostructure [5]. They concluded that the catalytic activity was affected by the atomic arrangement and structural order within the calcium-manganese oxide [5]. Frey *et al.* investigated water oxidation properties of a series of calcium birnessites powders and found that water-oxidation rate is affected by Ca : Mn ratio [6]. Najafpour showed that, when the calcium manganese oxides have structural similarities to natural OEC, they tend to exhibit strong water oxidation ability [7].

Although these studies revealed significant insights about the redox properties of calcium-manganese oxides, they were conducted without light irradiation. In artificial photosynthesis, the use of light is important. Najafpour *et al.* reported light-driven water oxidation with several manganese and calcium manganese compounds powders such as MnO_2, $Ca_2Mn_3O_8$, $CaMnO_3$, $CaMn_2O_4$, but only in the presence of various sacrificial reagents [7]. Sacrificial oxidants, in particular Ce^{4+}, limit the useful operating pH and may over-estimate photocatalytic activities, due to their high oxidation power [8]. To the best of our knowledge, there is only one paper reporting the photocatalytic water splitting properties of Ca_xMnO_y as a sole catalyst, but the catalysts were tested in the form of free-standing nanoparticles [9]. For practical applications of artificial photosynthesis, it is crucial to immobilize the catalysts on conducting electrodes as an anode, instead of using the catalysts in a form of free powders. A small number of studies were published on the catalytic properties of Ca_xMnO_y as electrode materials, but water splitting was induced only electrocatalytically without light irradiation [10-14]. As such, it is still not

understood how Ca_xMnO_y systems would perform as water-oxidising catalysts when photochemical and electrochemical conditions are combined.

It has been reported that, when the Ca–Mn–O systems have structural similarities to natural OEC, they tend to show stronger water oxidation ability, however, calcium manganese oxides, including $CaMnO_3$ and $CaMn_4O_8$, which are not structurally similar to natural OEC, also showed some water oxidation ability [15-16]. Therefore, the correlation between structure and light driven catalytic water-splitting properties has not yet been elucidated.

It has been reported that $CaMnO_3$, $Ca_2Mn_3O_8$ and $CaMn_2O_4$ have higher water oxidation efficiencies compared to MnO_2 in the presence of various sacrificial reagents without light irradiation [15]. However, little is known about light driven water oxidation efficiencies of the immobilized calcium manganese oxides compounds compared to MnO_2.

In this chapter, for the first time, the light-driven water-splitting activity of different calcium manganese oxides and manganese oxides (amorphous MnO_2, crystalline MnO_2, $Ca_2Mn_3O_8$, $CaMnO_3$ and $CaMn_2O_4$ was studied as a photo-anode in a three electrodes cell. All the manganese compounds were synthesized using mechanochemical processing. Further, structural similarity of calcium manganese oxides to the natural OEC cluster were quantitatively analyzed. The difference in their water oxidation performance was discussed based on manganese oxidation state, crystal structure, specific surface area, presence of calcium and structural similarities to the natural OEC.

5.2 Experimental procedure

5.2.1 Synthesis of manganese and calcium manganese oxides

Manganese and calcium manganese oxides were synthesized according to the procedure mentioned in chapter 3 and 4, respectively.

5.2.2 Physical Characterisation of catalyst powders

X-ray photoelectron spectroscopy (XPS) was conducted using a SPECS PHOIBOS 100 Analyser installed in a high-vacuum chamber with the base pressure below 10–8 mbar. Al-Kα radiation with a photon energy of 1486.6 eV was used at a voltage of 12 kV and power of 144 W. XPS binding energy spectra were recorded at a pass energy of 20 eV and a step width of 0.05-0.1 eV in the fixed analyser transmission mode. To increase the signal/noise ratio, multi-scans were conducted, and the intensity of signals were accumulated. Broad survey scans were recorded at a pass energy of 60 eV and a step width of 0.5 eV. XPS data analysis was carried out using the commercial Casa XPS software package.

5.2.3 Photo-electrochemical water splitting

5.2.3.1 Preparation of electrodes

Working electrodes containing the catalyst powders were embedded in polypyrrole (PPy) and deposited on fluorine-doped tin-oxide (FTO) glass slides. PPy is a conductive polymer and was used to improve electronic conduction, to provide structural stability to the electrode by

preventing photodegradation of the semiconductor, and to improve charge separation efficiency of the catalysts [17]. In addition, PPy generates charges upon visible light illumination and therefore nanoparticles modified with PPy have been shown to improve photocurrents and better conversation efficiencies [18].

Prior to the deposition of electrode materials, FTO glass slides were first cleaned by sonicating (B2500R-MTH ultrasonic bath) in an acetone-filled chamber for 90 min, followed by washing with water and drying by blowing air over the slides. Organic contaminants were further removed using a DIG UV PSD PR SERIES digital ozone-UV cleaner for 20 min. Subsequently, the slides were cleaned in a PLAMAFLO PDC-FMG plasma cleaner, followed by drying using an IKA® RCT basic hotplate at 60 °C.

To prepare electrodes, iron (III) p-toluenesulfonate (Fe(III)-pTS) was used to assist in vapour phase polymerization of pyrrole [19]. First, 85 mg of Fe(III)-pTS (Sigma Aldrich) was dissolved in 1 mL ethanol and sonicated for 10 min. Subsequently, 8 mg of catalyst powder was added to the solution and sonicated for 1 h. 100 µL of the resulting solution was drop-casted onto the FTO glass slide and spun at 1500 revolutions per min (rpm) for 2 min using a WS-400B-6NPP/LITE spin-coater. The slide was kept on a hotplate and dried at 60°C for 15 min.

Vapour phase polymerisation of pyrrole was carried out in a separate conical flask (500 mL capacity), equipped with a rubber stopper containing a crocodile clip. Within the flask, 0.500 mL pyrrole (Sigma Aldrich) was placed and the spin-coated FTO glass substrates were suspended above the pyrrole solution. The flask was placed in an oven at 60°C for 25 min to

allow polymerization of pyrrole on the slide surface. The sample was washed with ethanol and dried.

A copper wire was attached to the FTO surface with conductive silver paint and epoxy resin. Later, the contact area of the wire was covered with epoxy glue. Control samples were also prepared without addition of catalytic particles.

5.3.2.2 OER photocatalysis

Working electrodes were placed within a fully-enclosed quartz cell (5 x 5 x 5 cm) inside a closed cabinet that comprised a Faraday cage. A Pt mesh (1 x 2 cm) and a BASi Ag/AgCl aqueous salt bridge (KCl, 3 M) were used as a counter electrode and a reference electrode, respectively. The cell was filled with a 0.2 M Na_2SO_4 aqueous solution electrolyte, adjusted to pH 12 by adding NaOH. Prior to experiment, the electrolyte was bubbled with N_2 gas. Chronoamperograms (CA) were performed using an EDAQ466 potentiostat. Where applicable, the sample was illuminated with a SoLux daylight MR16 halogen light bulb (12 V, 50 W, 24^o; ca. 0.25 sun intensity) with a stable output range of 275 - 750 nm. The light was placed 10 cm from the working electrode and a Thorlabs visible-light bandpass filter (315-710 nm) was placed 1.5 cm in front of the light source to remove any infra-red wavelengths.

5.2.4 Goodness of fit calculation

The local structures of $Ca_2Mn_3O_8$ and $CaMn_2O_4$ were quantitatively compared with that of natural calcium manganese cluster, by superimposition of their local atomic arrangements. The goodness of fit was calculated using a least square fitting method, in the following sequence.

First, the local structure of the natural OEC cubane, as shown in Figure 5.1, was oriented in a Cartesian coordinate system in the following manner: The coordinate of the calcium atom was chosen to be (0,0,0), one of the oxygen atoms was placed on the x-axis, and the plane consisting of Ca_1, O_1 and O_2 atoms (in the Figure 5.1) was adjusted to be on the x-y plane. Then, the coordinates of the rest of the atoms were calculated from the distance between two adjacent atoms, using the following equation:

$$D = \sqrt{(x_2 - x_1)^2 + (y_2 - y_1)^2 + (z_2 - z_1)^2} \qquad (5.1),$$

where (x_1, y_1, z_1) and (x_2, y_2, z_2) are the Cartesian coordinates of adjacent two atoms. The distances between different atoms of the natural OEC cubane was taken from the literature [2]. In order to solve the set of equations created using the formula above, Matlab was used.

Next, a section of the crystal structure which resembles that of natural water-oxidizing cubane was identified in the crystal structures of calcium manganese oxides. The selected local structure contained one calcium atom and three manganese atoms, as highlighted with yellow mesh in Figure 5.2 for $Ca_2Mn_3O_8$ and Figure 5.3 for $CaMn_2O_4$. The atomic coordinates in the selected local structure were collected from an internet source, Materials Project ([20] for $Ca_2Mn_3O_8$, [21] for $CaMn_2O_4$). Materials project, which is supported by the U.S. Department of Energy, provides computational data sets for various materials.

Materials Project provided fractional coordinates, which were converted into Cartesian coordinates. Using these coordinates, a section of the crystal structure was drawn using the

"Mercury" software. With the help of the coordinates, distances between different atoms were calculated using Equation (5.1).

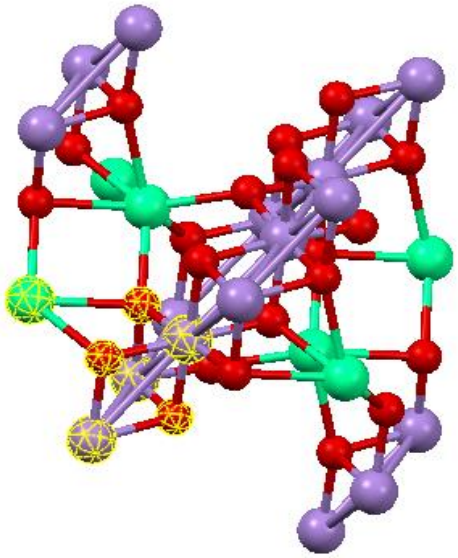

Figure 5.2. Crystal structure of $Ca_2Mn_3O_8$. A section highlighted in yellow mesh, resembles the structure of natural water-oxidizing cubane. Calcium in green; manganese in blue; oxygen in red.

The calcium atom in the selected local structure was placed at the origin of the Cartesian coordinate system. The orientation of the selected local structure was defined with the rotational angles around x, y and z axes, Θ_x, Θ_y and Θ_z. After calculating the coordinates of all atoms as a function of Θ_x, Θ_y and Θ_z, goodness-of-fit was assessed by calculating the ω-value using the following formula:

$$\omega^2 = \sum_i \left\{ (x_i - x_{ci})^2 + (y_i - y_{ci})^2 + (z_i - z_{ci})^2 \right\} \qquad (5.2),$$

where (x_i, y_i, z_i) are the Cartesian coordinates of the i^{th} atom in the natural OEC cubane and (x_{ci}, y_{ci}, z_{ci}) are the coordinates of the corresponding atom in the selected local structure of calcium manganese oxides.

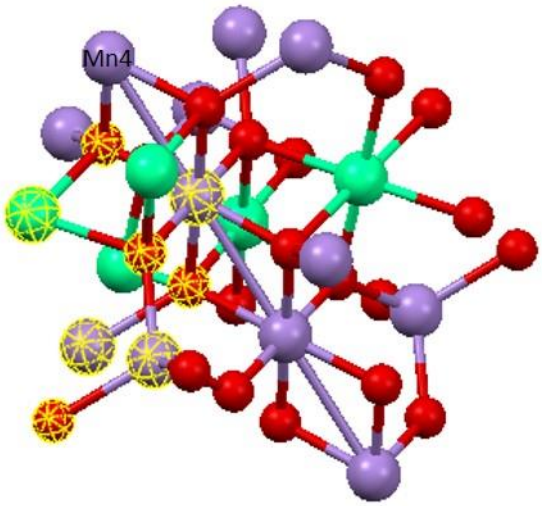

Figure 5.3. Crystal structure of $CaMn_2O_4$. A section highlighted in yellow mesh, resembles the structure of natural OEC cubane. Calcium in green; manganese in blue; oxygen in red.

5.3 Results and Discussion

5.3.1 Physical Characterisation of catalyst powders

XPS analysis was performed to characterize the surface oxidation states of the catalysts. XPS data are shown in Figure 5.4 and Table 5.1. Two strong peaks centred at approximately 641 and 653 eV were observed in the Mn2p spectra, which were attributed to Mn $2p_{3/2}$ and Mn $2p_{1/2}$ spin-orbit doublet respectively (Figure 5.4a). As shown in Table 5.1, Mn $2p_{3/2}$ peak for $CaMn_2O_4$ was observed at slightly lower binding energy as compared to other compounds due to the presence of Mn^{3+}. Although a qualitative reflection of manganese oxidation state could be seen due to the chemical shift of Mn 2p [22], quantitative determination of the manganese

valence state was difficult due to small magnitude. Therefore, an average oxidation state (AOS) of the compounds, presented in Table 5.1, was calculated using the energy difference between the two 3s-manganese peaks (Figure 5.4b) [23].

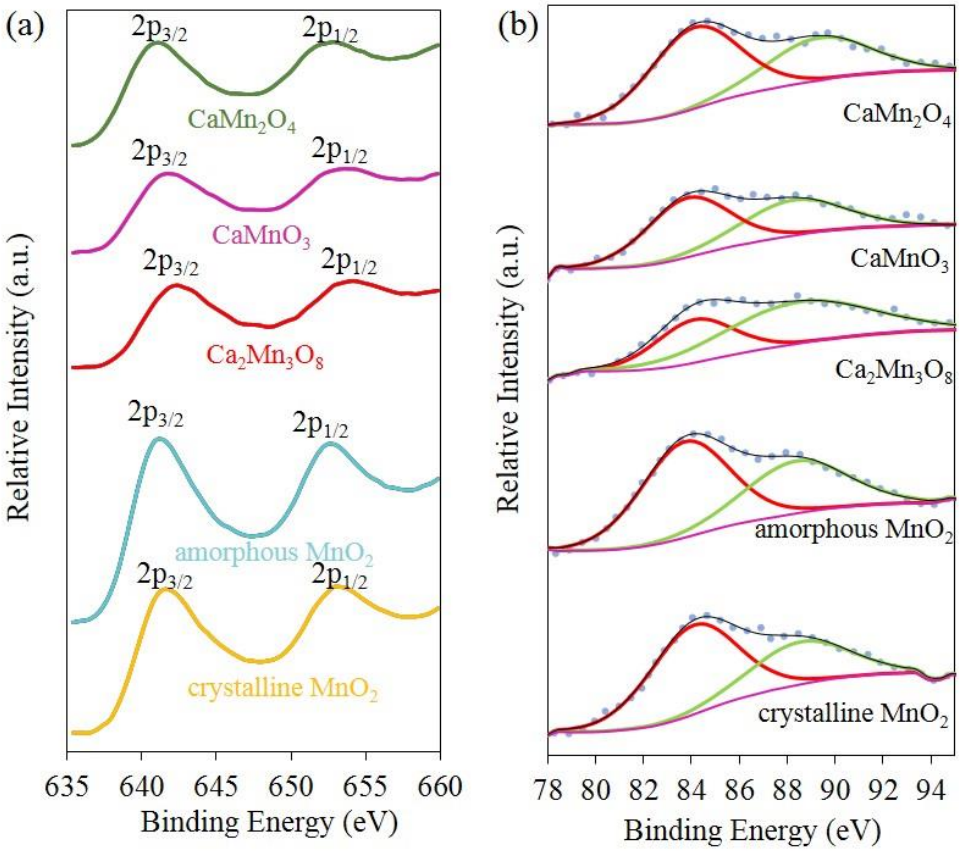

Figure 5.4. (a) Mn 2p and (b) Mn 3s XPS spectra of synthesized amorphous and crystalline MnO_2, $Ca_2Mn_3O_8$, $CaMnO_3$ and $CaMn_2O_4$.

AOS obtained through XPS analysis are in good agreement with the theoretical values of oxidation states in these compounds. AOS for amorphous MnO_2 was found slightly lower than crystalline MnO_2, possibly due to the presence of surface oxygen vacancies and dangling bonds.

Table 5.1. Mn $2p_{3/2}$ and Mn 3s XPS data of as synthesized compounds.

Sample	Mn $2p_{3/2}$ (eV)	Mn 3s (eV) Peak 1	Mn 3s (eV) Peak 2	ΔEs (eV)	Average Oxidation State (AOS)
Amorphous MnO_2	641.3	83.7	88.3	4.6	3.75
Crystalline MnO_2	641.8	84.1	88.5	4.4	3.97
$CaMnO_3$	641.8	83.8	88.2	4.4	3.97
$Ca_2Mn_3O_8$	642.3	84.1	88.4	4.3	4.09
$CaMn_2O_4$	640.8	84.1	89.3	5.2	3.07

[a] Calculated with the formula: AOS = 8.95–1.13 × ΔEs, where the ΔEs is the splitting energy of the Mn 3s [23].

5.3.2 OER Photocatalysis

5.3.2.1 Light and dark current densities

Figure 5.5 shows the current densities of the samples tested in a 0.2 M Na_2SO_4 aqueous solution (pH 12) at 1 V (vs Ag/AgCl) bias, with and without light illumination. The working electrode consisting of the oxide powder and PPy produced higher dark and light current, in comparison to the working electrode with PPy alone. Table 5.2 lists the average light and dark current densities exhibited by different samples. The working electrode with $CaMnO_3$ and amorphous MnO_2 produced highest and nearly the same dark and light current, whereas lowest dark current was produced by $CaMn_2O_4$/PPy. On the contrary, highest photocurrent (i.e. difference between light and dark current) was observed for $CaMn_2O_4$/PPy sample. Compounds with calcium produced higher photocurrent compared to MnO_2.

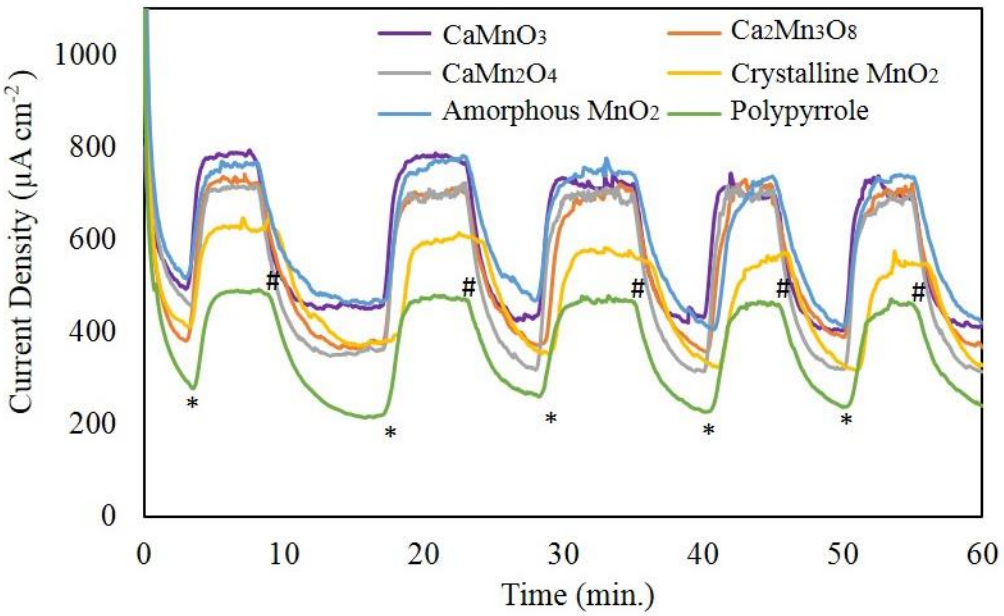

Figure 5.5. Chronoamperograms at 1 V (vs Ag/AgCl) in 0.2 M Na_2SO_4 (pH 12) over 1 h of operation, with and without light illumination (0.25 sun), of FTO glass slides coated with thin films of amorphous and crystalline MnO_2, $Ca_2Mn_3O_8$, $CaMnO_3$, $CaMn_2O_4$ and polypyrrole (control). (*='light on', #='light off').

Table 5.2. Average light and dark current densities.

Sample	Average light current density ($\mu A\ cm^{-2}$)	Average dark current density ($\mu A\ cm^{-2}$)	Average photo current density ($\mu A\ cm^{-2}$)
Amorphous MnO_2 / PPy	742	444	298
Crystalline MnO_2 / PPy	581	331	250
$CaMnO_3$ / PPy	746	440	306
$Ca_2Mn_3O_8$ / PPy	714	373	341
$CaMn_2O_4$ / PPy	701	326	375
PPy (control)	447	230	217

5.3.2.2 Mechanism of photo-induced OER

In Chapters 3 and 4, band gap values and band edge positions of different samples were determined experimentally, which are shown in Table 5.3. The band gap energy and, HOMO-LUMO levels of PPy were obtained from the literature [24].

Table 5.3. Band gap, conduction and valence band edges of manganese-based oxides.

Sample	Band gap (eV)	Conduction band (eV)	Valence band (eV)
Amorphous MnO_2	2.54	0.83	3.37
Crystalline MnO_2	2.33	0.86	3.19
$CaMnO_3$	1.5	0.92	2.42
$Ca_2Mn_3O_8$	2.1	0.88	2.98
$CaMn_2O_4$	1.5	1.01	2.51
PPy	2.5	-0.47 (LUMO)	2.03 (HOMO)

Using the values in Table 5.3, a schematic diagram of the energy levels of the PPy/oxides electrodes are drawn in Figure 5.6. PPy itself is a semiconductor that can absorb visible light to generate electrons and holes, and hence photocurrent generation as in Figure 5.5. MnO_2 and calcium manganese oxides are also semiconductors that absorb visible light to generate electrons and holes, but their photocurrent without PPy was very small (Figures 3.9, 4.9). When the oxides and PPy were combined, a significant increase in current was observed (Figure 5.5). As shown in Figure 5.6, polypyrrole provides a pathway to prevent direct recombination of photo-generated holes and electrons, by forming a type-II (staggered type) heterojunction with the valence and conduction bands of the oxides. Since the valence band edges of oxide particles

are more positive than the HOMO level of PPy, the holes photo-generated at the oxides are injected into the HOMO of PPy, which has sufficient electrochemical energy to produce oxygen from water via the following reaction:

$$2H_2O + 4h+ \rightarrow O_2 + 4H^+ \quad (5.3).$$

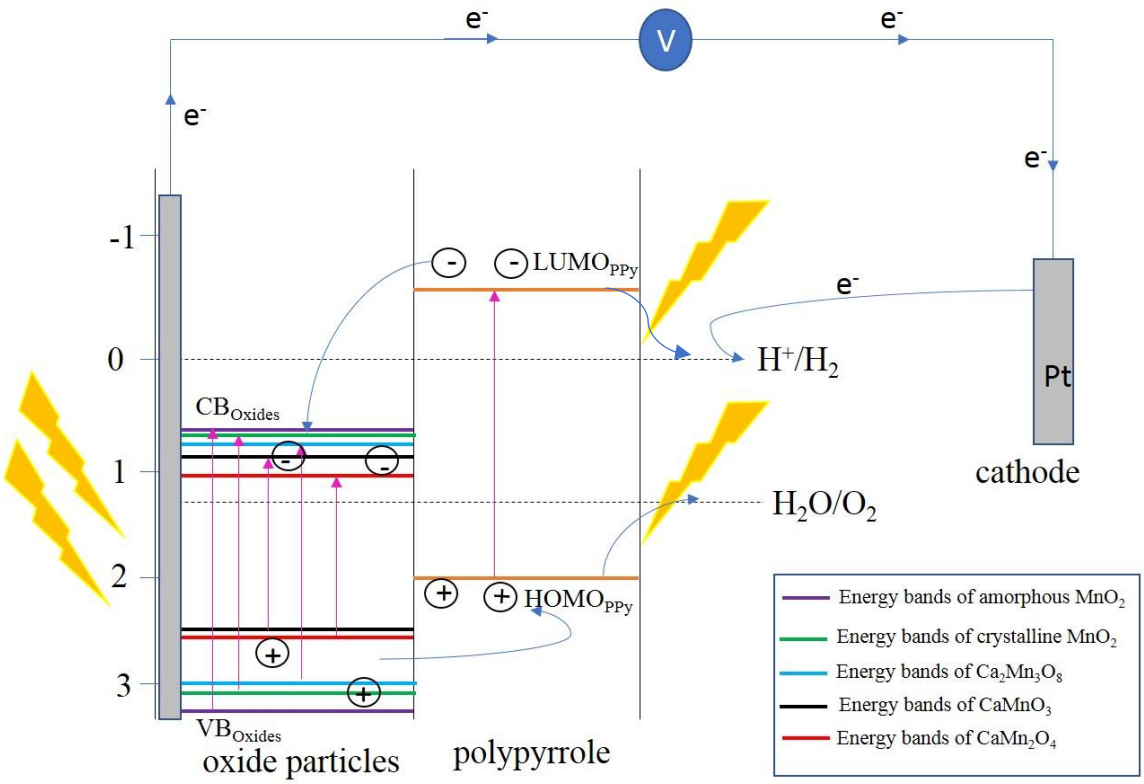

Figure 5.6. Proposed mechanism through schematic diagram of the energy levels of the PPy-oxide particles electrodes.

The holes photo-generated at PPy also contribute to the production of oxygen from water. On the other hand, photo-exited electrons at PPy are either transferred to the conduction band of oxides and then to the FTO electrode to contribute to the photocurrent, or are used to generate hydrogen via the following reaction:

$$2H^+ + 2e^- \rightarrow H_2 \quad (5.4).$$

Photo-exited electrons at the oxides can also contribute to the photocurrent but cannot be used to generate H_2 via the reaction 5.4, because their valence band edge energies are higher than the electrochemical potential of the reaction 5.4.

5.3.3 Similarity in local atomic arrangement

In order to study the similarity of the local atomic arrangement of calcium manganates and the natural OER cubane, structural goodness-of-fit analysis was conducted. In the crystal of $Ca_2Mn_3O_8$, there is no manganese atom having a location equivalent to Mn4 in the natural OEC cubane (Figure 5.1). Also, one oxygen is missing from the cube (Figures 5.7 b-d). Therefore, for the structural goodness-of-fit analysis, there are three possible ways to orient the local structure of $Ca_2Mn_3O_8$ and $CaMn_2O_4$ with that of the natural OEC cubane, as shown in Figures 5.7(b-d) and Figures 5.8 (b-d), respectively. For comparison, the atomic configuration of the natural OEC cubane is also shown in Figures 5.7 (a) and 5.8 (a). In the crystal of $CaMn_2O_4$, there is a manganese atom having a location equivalent to Mn4 in the natural OEC cubane (Figure 5.3). If the direction of Mn4 is matched in the two structures, there is only one way to orient the local structure of $CaMn_2O_4$ for the goodness-of-fit analysis (Figure 5.8c). If the location of Mn4 is ignored, there are three possible ways to orient the local structure of $CaMn_2O_4$ as shown in Figure 5.8(b-d). The structural goodness of fit was calculated for each orientation and expressed with ω as in Table 5.4. For $Ca_2Mn_3O_8$, the orientation in Figure 5.7d gave much smaller ω values than other two orientations. For $CaMn_2O_4$, the ω values of the three orientations gave similar ω value but the orientation in Figure 5.8 (d) gave a slightly

smaller ω value than the other two orientations. Overall $Ca_2Mn_3O_8$ gave significantly smaller ω values than $CaMn_2O_4$.

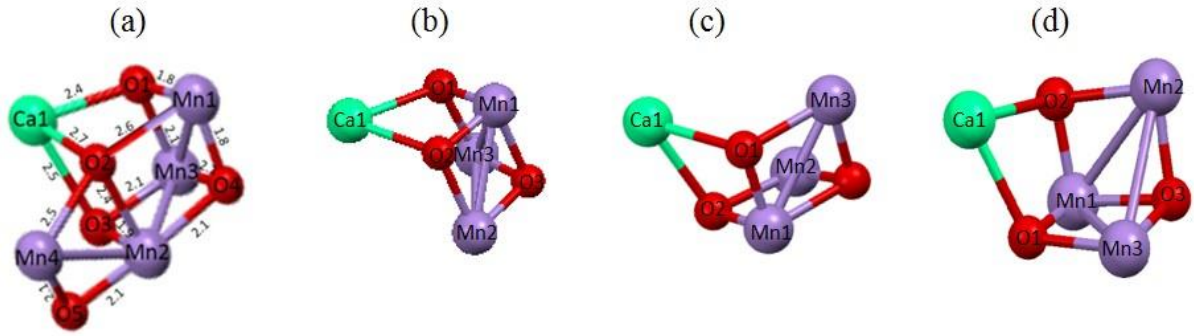

Figure 5.7. Ball and stick model of (a) natural cubane, (b-d) three orientations of cubane like part of $Ca_2Mn_3O_8$ crystal.

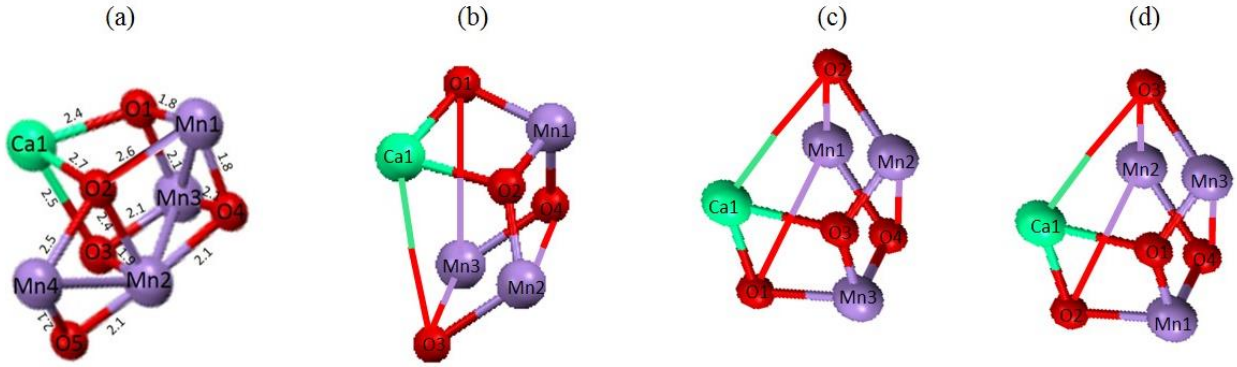

Figure 5.8. Ball and stick model of (a) natural cubane, (b-d) three orientations of cubane like part of $CaMn_2O_4$ crystal.

Table 5.4. Calculated ω values for different orientations.

Compound	Orientation	ω value
$Ca_2Mn_3O_8$	1 (Figure 5.8b)	1.16
	2 (Figure 5.8c)	1.13
	3 (Figure 5.8d)	0.81
$CaMn_2O_4$	1 (Figure 5.9b)	2.77
	2 (Figure 5.9c)	2.65
	3 (Figure 5.9d)	2.61

5.3.4 Overall comparison

In the past, studies of the catalytic activities of calcium manganates was motivated by their structural similarity to the natural OEC cubane. However, there are many factors that potentially affect the water oxidation activities of the oxide catalysts. The factors include specific surface area, light absorption efficiency (bandgap energy), charge separation efficiency and charge transfer efficiency, in addition to the oxidation state of manganese ions and the structural similarity to the natural OEC cubane. In order to elucidate the effects of the oxidation state of manganese ions and the structural similarity to the natural OEC cubane, the photocurrent was converted to 'effective photocurrent', as shown in Table 5.5, where the effects of specific surface area, light absorption efficiency (bandgap energy) and charge separation efficiency are considered, using the following equation:

$$I_{eff} = I_{obs} / (S \cdot \eta_{charge} \cdot \eta_{abs}) \qquad (5.5),$$

where I_{eff} is the effective photocurrent density, I_{obs} is the raw current density observed in μA·cm^{-2}, S is the specific surface area in m^2·g^{-1}, η_{charge} is the charge separation efficiency, and η_{abs} is the light harvesting efficiency of the catalyst powders. This approach may be very simplistic but still provides some insight on the potential causes of the difference in the photo-induced OER of the compounds.

Table 5.5. Effective photo current.

Sample	Effective photo current density	Mn oxidation state	Structural similarity to natural OEC
Amorphous MnO_2	0.078	3.75	No
Crystalline MnO_2	0.258	3.97	No
$CaMnO_3$	0.339	3.97	No
$Ca_2Mn_3O_8$	0.511	4.09	Yes (ω=0.81)
$CaMn_2O_4$	1.478	3.07	Yes (ω=2.77)

Table 5.5 shows that, all the calcium manganese oxides produced overall higher effective photocurrent than manganese oxides. Although MnO_2 is one of the most studied photocatalysts among manganese-based materials, the present study showed that calcium manganese oxides are better photocatalysts than MnO_2. Under the dark condition, the research group of Najafpour and Kurz reported similar results in electrochemical water splitting; calcium manganese oxides produced higher water-oxidation efficiency than MnO_2. Wiechem *et al.* report that, when Ca is replaced by other alkali earth metals (Sr, Mg) in birnessites-type manganese oxides, the electrochemical water-oxidation activity decreased under the dark condition [25]. Based on their studies, Najafpour and Kurz argued the importance of calcium in the water-oxidation reaction, hypothesising that Ca will activate the O-O bond between water and oxide catalysts [26]. Rong *et al*. changed the Ca-to-Mn ratio in the birnessite structure and found that Ca-to-Mn ratio affects the efficiency of catalytic oxygen evolution reaction [9]. As explained in Chapter 2, in the natural OEC cubane, Ca plays a similar and essential role in water splitting. Although the detailed structural and functional roles of Ca are still not fully understood, if Ca

assist the interaction between water and catalyst surface, the presence of Ca would be equally beneficial for water splitting both under light and dark conditions. However, the influence of the presence of Ca in the crystal structure of manganese-based catalysts should be discussed in conjunction with other effect that the presence of Ca will bring to the materials, including the change in crystal structure that leads to the change in bandgap energy, band edge position, charge diffusion length and charge separation efficiency.

Among the three calcium manganese oxides, the compounds with better structural similarity ($Ca_2Mn_3O_8$ and $CaMn_2O_4$) to the natural OEC cubane demonstrated higher effective photocurrent. Table 5.6 compares the local structure and manganese valence number of $Ca_2Mn_3O_8$ and $CaMn_2O_4$. Although the structural similarity to the natural OEC cubane is higher for $Ca_2Mn_3O_8$ than $CaMn_2O_4$, $Ca_2Mn_3O_8$ showed lower effective photocurrent than $CaMn_2O_4$. One possible reason for the better structural goodness-of-fit of $Ca_2Mn_3O_8$ with the natural OEC than $CaMn_2O_4$, is the smaller number of atoms used for the goodness-of-fit calculation; an oxygen atom is absent from the cubane-like part of $Ca_2Mn_3O_8$ (Figure 5.7), obviously rendering the possibility of less mismatch with the natural OEC. On the other hand, the local crystal structure of $CaMn_2O_4$ has all the atoms at similar positions in the cubane. The results can be interpreted as that, having all atoms in the cubane-like structure may be more important than having close geometry to the natural OEC. In addition, the presence of Mn4 and/or oxidation state of Mn may be more important than the actual shape of cubane-like part of the crystal structure. In fact, in the natural OEC cubane, the fourth manganese ion plays a key role in the water-splitting process [3, 27] and that the three other manganese in the cube act as hole donors to the fourth manganese, as discussed in Chapter 2.

Table 5.6. Comparison of $Ca_2Mn_3O_8$ and $CaMn_2O_4$.

Compound	Presence of manganese equivalent to Mn4 in OEC cubane	Bulk Mn valence number	Mn valence number	Goodness of fit (ω)	Photocatalysis
$Ca_2Mn_3O_8$	No	+4	4.09	0.81	lower than $CaMn_2O_4$
$CaMn_2O_4$	Yes	+3	3.07	2.77	higher than $Ca_2Mn_3O_8$

Han *et al*. [28], Rong *et al*. [9] and Zaharieva *et al*. [29] reported similar observations in the electrochemical water splitting under dark conditions; the compounds with better structural similarity ($Ca_2Mn_3O_8$ and $CaMn_2O_4$) to the natural OEC cubane demonstrated higher effective photocurrent. It is tempting to speculate that the structural role similar to that in the natural cubane is present in the ceramic calcium manganates. However, the influence of the local crystal structure of manganese-based catalysts should be carefully discussed in conjunction with other effects that the local atomic structure will bring to the materials, including the change in bandgap energy, band edge position, charge diffusion length and charge separation efficiency, which is lacking in the past studies.

In Table 5.5, it is evident that crystalline MnO_2 showed higher effective photocurrent than amorphous MnO_2. From the results, it may be speculated that a higher manganese oxidation state may be favorable for photocatalytic water splitting. Experimental and computational studies conducted on manganese oxidation states in the natural OEC cubane also support the high valent oxidation scheme [30-32]. However, $CaMn_2O_4$ showed the highest effective photocurrent, despite the lowest manganese oxidation state among all the studied compounds.

Therefore, it is not conclusive if and to what extent the oxidation states of manganese influences the photo-induced water oxidation catalysis. The results of the past studies under the dark conditions in electrochemical water oxidation (i.e. non-photocatalytic) are also inconclusive: Frey *et al*. reported that calcium manganates with higher oxidation states of manganese gave higher catalytic performance in the dark [6], whereas Rong *et al*. [9] and Baktash *et al*. [5] reported that intermediate oxidation states of manganese between 3.5 and 4 are most active in water oxidation in the dark. It is prudent to point out that, in the past, the discussion of the effect of manganese oxidation states in water oxidation catalysis did not consider the overall effects of the change in the oxidation states, including the creation of intra-bandgap defect energy levels and charge separation efficiency.

In addition, investigation by Pokhrel *et al.* made an interesting observation that water oxidation abilities are dependent on test conditions. They tested nine crystalline MnO_x materials (α-MnO_2, β-MnO_2, R-MnO_2, λ-MnO_2, δ-MnO_2, γ-MnO_2, Mn_2O_3, Mn_3O_4, $LiMn_2O_4$) by chemical, photochemical and electrochemical assays, and reported that the identity of the "best" catalysis is dependent on the oxidation method. Their results showed that γ-MnO_2 performed the best in a ceric ammonium nitrate solution of pH 0.8 (chemical oxidant method), Mn_2O_3 showed highest water oxidation during photochemical assay (pH 8) and the best catalysts was dependent on the pH of electrolyte during electrochemical testing which was Mn_2O_3 (for acidic electrolyte), γ-MnO_2 (for neutral pH electrolyte) and α-MnO_2 (for alkaline electrolyte) [33]. Thus, it could be concluded that water splitting abilities of different oxidation state of manganese are also strongly dependent on experimental conditions.

Overall, the results suggest that, for the development of manganese-based water oxidation photocatalysts, there may be some possible importance of having a local structure similar to

that of the natural OEC cubane including the presence of Ca, but also highlighted the danger to take a simplistic approach in focusing on the local structure.

5.4 Chapter summary

In the present study, different calcium manganese oxides ($CaMnO_3$, $Ca_2Mn_3O_8$ and $CaMn_2O_4$) were investigated for their catalytic properties in photo-electrochemical water oxidation, in a photo-electrochemical cell for the first time. Manganese oxides (amorphous MnO_2 and crystalline α-MnO_2) were also studies for comparison. The results showed that the films with oxides powders produced higher dark and light current in comparison to the film without oxides. The highest photocurrent was observed for the anode containing $CaMn_2O_4$. It was found that the band edges of calcium manganese oxides are suitable for oxygen evolution through water splitting. Although MnO_2 has been known as one of the most promising redox catalysts and photocatalysts among manganese-based materials, the present study showed that calcium manganese oxides induced higher photocurrent than MnO_2. Hence this study signifies the importance of further research on calcium manganate ceramics as a new class of catalysts in photo-electrochemical water splitting.

The present study also demonstrated the effectiveness of a new anode design for manganese-based catalysts in photo-electrochemical cells. The catalyst materials were embedded within PPy to form an anode, which enabled high conductivity within the anode. The combination of calcium manganese oxides and PPy formed a type-II (staggered type) heterojunction, which increased charge separation efficiency within the anode and in turn improved oxygen evolution in the photo-electrochemical cell. The optimisation of the anode design including powder

loading and thickness was outside the scope of this investigation and is subject to further studies.

In the past, studies of the catalytic activities of calcium manganates was motivated by their structural similarity to the natural OEC cubane. However, the present study signals that much caution is required to this approach. Quantitative structural goodness-of-fit studies revealed that, although the structural similarity to the natural OEC cubane is higher for $Ca_2Mn_3O_8$ than $CaMn_2O_4$, $Ca_2Mn_3O_8$ showed lower effective photocurrent than $CaMn_2O_4$. The results imply that the role of other factors that potentially affect the water oxidation activities of the oxide catalysts, such as manganese oxidation states, presence of crystal defects, electron energy states (bandgap energy & band edge positions) and experimental conditions, must be carefully considered to conduct an overall assessment of the catalytic activities of calcium manganates. The discussions made in the literatures should be critically interpreted accordingly.

From a biomimetic perspective, the theoretical and experimental studies presented in this chapter were rather simplistic, but nevertheless provided a foundation for more sophisticated studies for better design of biomimetic photocatalysts in the future.

5.5 References

1. Najafpour, M.M., 2011. *Calcium-manganese oxides as structural and functional models for active site in oxygen evolving complex in photosystem II: Lessons from simple models.* Journal of Photochemistry and Photobiology B: Biology, 104, pp.111-117.
2. Umena, Y., Kawakami, K., Shen, J.-R., and Kamiya, N., 2011. *Crystal structure of oxygen-evolving photosystem II at a resolution of 1.9 Å.* Nature, 473, p.55.
3. Barber, J., 2016. *Mn_4Ca cluster of photosynthetic oxygen-evolving center: structure, function and evolution*. Biochemistry, 55, pp.5901-5906.
4. Gagrani, A. and Tsuzuki, T., 2018. *Calcium manganese oxides as biomimetic catalysts in energy applications: A short review.* Chemical Engineering Science, 194, pp.116-126.
5. Baktash, E., Zaharieva, I., Schröder, M., Goebel, C., Dau, H., and Thomas, A., 2013. *Cyanamide route to calcium–manganese oxide foams for water oxidation.* Dalton Transactions, 42, pp.16920-16929.
6. Frey, C.E., Wiechen, M., and Kurz, P., 2014. *Water-oxidation catalysis by synthetic manganese oxides–systematic variations of the calcium birnessite theme.* Dalton Transactions, 43, pp.4370-4379.
7. Najafpour, M.M., Pashaei, B., and Nayeri, S., 2012. *Calcium manganese (IV) oxides: biomimetic and efficient catalysts for water oxidation.* Dalton Transactions, 41, pp.4799-4805.
8. Parent, A.R., Crabtree, R.H. and Brudvig, G.W., 2013. *Comparison of primary oxidants for water-oxidation catalysis*. Chemical Society Reviews, 42, pp.2247-2252.
9. Rong, F., Zhao, J., Chen, Z., Xu, Y., Zhao, Y., Yang, Q., and Li, C., 2016. *Highly active water oxidation on nanostructured biomimetic calcium manganese oxide catalysts.* Journal of Materials Chemistry A, 4, pp.6585-6594.
10. Zahran, Z.N., Mohamed, E.A., and Naruta, Y., 2017. *Electrocatalytic water oxidation at low energy cost by a highly active and robust calcium–manganese oxide thin film sintered on an FTO electrode with ethyl methyl imidazolium triflate ionic liquid*. Journal of Materials Chemistry A, 5, pp.15167-15174.
11. Ramírez, A., Bogdanoff, P., Friedrich, D., and Fiechter, S., 2012. *Synthesis of $Ca_2Mn_3O_8$ films and their electrochemical studies for the oxygen evolution reaction (OER) of water*. Nano Energy, pp.282-289.
12. Du, J., Zhang, T., Cheng, F., Chu, W., Wu, Z., and Chen, J., 2014. *Nonstoichiometric Perovskite $CaMnO_{3-\delta}$ for Oxygen Electrocatalysis with High Activity*. Inorganic Chemistry, 53, pp.9106-9114.
13. Raabe, S., Mierwaldt, D., Ciston, J., Uijttewaal, M., Stein, H., Hoffmann, J., Zhu, Y., Blöchl, P., and Jooss, C., 2012. *In Situ Electrochemical Electron Microscopy Study of Oxygen Evolution Activity of Doped Manganite Perovskites.* Advanced Functional Materials, 22, pp. 3378-3388.
14. Lee, S.Y., González-Flores, D., Ohms, J., Trost, T., Dau, H., Zaharieva, I., and Kurz, P., 2014. *Screen-Printed Calcium–Birnessite Electrodes for Water Oxidation at Neutral pH and an "Electrochemical Harriman Series".* ChemSusChem, 7, pp.3442-3451.
15. Najafpour, M.M., 2011. *Mixed-valence manganese calcium oxides as efficient catalysts for water oxidation.* Dalton Transactions, 40, pp.3793-3795.
16. Najafpour, M.M. and Sedigh, D.J., 2013. *Water oxidation by manganese oxides, a new step towards a complete picture: simplicity is the ultimate sophistication*. Dalton Transactions, 42, pp.12173-12178
17. Frank, A.J. and Honda, K., 1985. *Polymer-modified electrodes, catalysis and water-splitting reactions.* Journal of Photochemistry, 29, pp.195-204.
18. Zhang, Z., Yuan, Y., Liang, L., Cheng, Y., Xu, H., Shi, G. and Jin, L., 2008. *Preparation and photoelectrochemical properties of a hybrid electrode composed of polypyrrole encapsulated in highly ordered titanium dioxide nanotube array*. Thin Solid Films, 516, pp.8663-8667.
19. Winther-Jensen, B., Chen, J., West, K. and Wallace, G., 2004. *Vapor phase polymerization of pyrrole and thiophene using iron (III) sulfonates as oxidizing agents*. Macromolecules, 37, pp.5930-5935.

20. https://materialsproject.org/materials/mp-18893/#, viewed 20 July 2017.
21. https://materialsproject.org/materials/mvc-6593/#, viewed 20 July 2017.
22. Jorge, M.M., dos Santos, A.C. and Nunes, M.R., 2001. *Effects of synthesis method on stoichiometry, structure and electrical conductivity of $CaMnO_{3-\delta}$*. International Journal of Inorganic Materials, 3, pp.915-921.
23. Sun, M., Zhang, B., Liu, H., He, B., Ye, F., Yu, L., Sun, C., Wen, H., 2017. *The effect of acid/alkali treatment on the catalytic combustion activity of manganese oxide octahedral molecular sieves*, RCS Advances,7, pp.3958-3965.
24. Wang, J. and Ni, X., 2008. *Photoresponsive polypyrrole-TiO_2 nanoparticles film fabricated by a novel surface initiated polymerization*. Solid State Communications,146, pp.239-244.
25. Wiechen, M., Zaharieva, I., Dau, H. and Kurz, P., 2012. *Layered manganese oxides for water-oxidation: alkaline earth cations influence catalytic activity in a photosystem II-like fashion.* Chemical Science, 3, pp.2330-2339.
26. Najafpour, M.M., Ehrenberg, T., Wiechen, M. and Kurz, P., 2010. *Calcium manganese (III) oxides ($CaMn_2O_4 \cdot xH_2O$) as biomimetic oxygen-evolving catalysts*. Angewandte Chemie International Edition, 49, pp.2233-2237.
27. Barber, J., 2009. *Photosynthetic energy conversion: natural and artificial*. Chemical Society Reviews, 38, pp.185-196.
28. Han, X., Zhang, T., Du, J., Cheng, F. and Chen, J., 2013. *Porous calcium–manganese oxide microspheres for electrocatalytic oxygen reduction with high activity*. Chemical Science, 4, pp.368-376.
29. Zaharieva, I., Najafpour, M.M., Wiechen, M., Haumann, M., Kurz, P. and Dau, H., 2011. *Synthetic manganese–calcium oxides mimic the water-oxidizing complex of photosynthesis functionally and structurally*. Energy & Environmental Science, 4, pp.2400-2408.
30. Messinger, J., Robblee, J.H., Bergmann, U., Fernandez, C., Glatzel, P., Visser, H., Cinco, R.M., McFarlane, K.L., Bellacchio, E., Pizarro, S.A. and Cramer, S.P., 2001. *Absence of Mn-centered oxidation in the $S_2 \rightarrow S_3$ transition: implications for the mechanism of photosynthetic water oxidation*. Journal of the American Chemical Society, 123, pp.7804-7820.
31. Iuzzolino, L., Dittmer, J., Dörner, W., Meyer-Klaucke, W. and Dau, H., 1998. *X-ray absorption spectroscopy on layered photosystem II membrane particles suggests manganese-centered oxidation of the oxygen-evolving complex for the S_0-S_1, S_1-S_2, and S_2-S_3 transitions of the water oxidation cycle*. Biochemistry, 37, pp.17112-17119.
32. Krewald, V., Retegan, M., Cox, N., Messinger, J., Lubitz, W., DeBeer, S., Neese, F. and Pantazis, D.A., 2015. *Metal oxidation states in biological water splitting*. Chemical science, 6, pp.1676-1695.
33. Pokhrel, R., Goetz, M.K., Shaner, S.E., Wu, X. and Stahl, S.S., 2015. *The "best catalyst" for water oxidation depends on the oxidation method employed: a case study of manganese oxides*. Journal of the American Chemical Society, 137, pp.8384-8387.

Chapter 6

Photo-electrochemical oxygen evolution reaction by biomimetic $CaMn_2O_4$ catalyst: Effects of particle shape on PEC oxygen evolution

Remarks:

The publication relevant to this chapter is "Ankita Gagrani, Mohammed Alsultan, Gerhard Swiegers, Takuya Tsuzuki, "*Photo-electrochemical oxygen evolution reaction by biomimetic $CaMn_2O_4$ catalyst*", **Applied Sciences**, 9, 2196, **2019**"**.** The abstract, introduction, experimental section and conclusion of the chapter were slightly modified from the publication in order to fit into the structure of the thesis.

Abstract

$CaMn_2O_4$ has been identified as the best photocatalytic material among manganese-based compounds studied in the previous chapters. In this chapter, the photo-electrocatalytic properties of $CaMn_2O_4$ with two different morphologies were investigated. $CaMn_2O_4$ powders with irregular-shapes and nanowire shapes were synthesized using mechanochemical processing and a hydrothermal method, respectively. The anode in a photo-electrochemical cell was fabricated by embedding $CaMn_2O_4$ powders within polypyrrole. The results showed that $CaMn_2O_4$ induced higher dark- and light- current in comparison to the control sample (polypyrrole alone). $CaMn_2O_4$ nanowires exhibited higher dark- and light- current in comparison to irregular-shaped $CaMn_2O_4$ powders. The difference was attributable to the higher surface area of nanowires compared to the irregular-shaped particles, rather than the difference in exposed crystal facets.

6.1 Introduction

In natural photosynthesis, bio-electricity decomposes water into hydrogen and oxygen within a unique catalytic centre composed of a $CaMn_4O_5$ cluster, in the oxygen evolving complex (OEC) enzyme in the Photosystem II protein [1-4]. This natural process is the most efficient known, for the photo-generation of O_2 from water.

$CaMn_2O_4$ was the best photocatalytic material among the manganese-based oxides studied in the previous chapters. There has been extensive investigation of catalytic water oxidation properties of $CaMn_2O_4$ [5-7] by other researchers. Han *et al*. reported an oxygen-reduction reaction (ORR) catalytic activity of $CaMn_2O_4$ microspheres consisting of aggregated nanoparticles [5]. Du. *et al*. demonstrated that one-dimensional $CaMn_2O_4$ nanostructures, synthesized using a solvothermal method, enabled quasi-four-electron transfer in the ORR [6]. These studies were electrochemical in nature, and therefore were conducted without any light irradiation. It is very important to study the water splitting in the presence of light, because the use of natural sunlight as the source of energy is critical in sustainability-related applications.

Najafpour *et al*. studied light-driven oxygen evolution by using an aqueous suspension of $CaMn_2O_4$ particles, however only in the presence of various sacrificial reagents [7]. Although the studies of photo-catalysts in the dispersed powder form are of significant interest, from practical perspective, it is crucial to study the immobilization of catalysts on conducting electrodes as an anode.

It has been reported that photocatalytic properties are greatly affected by the morphology of catalysts [8]. In this chapter, $CaMn_2O_4$ ultrafine powders with different morphologies were

studied as an anode material in photo-electrochemical cells for their catalytic and photocatalytic properties in the water oxidation reaction. In this study, we were able to produce $CaMn_2O_4$ with two different morphologies; irregular-shapes and nanowire shapes. The production of $CaMn_2O_4$ with other shapes was not successful.

6.2 Experimental Procedure

6.2.1 Synthesis of irregular-shaped $CaMn_2O_4$ particles

$CaMn_2O_4$ ultrafine particles were synthesized according to the procedure mentioned in Chapter 4. In brief, $CaMn_2(CO_3)_3$ nanoparticles, embedded within excess salt matrix, were first produced by mechanochemical processing, which were thermally decomposed into $CaMn_2O_4$. Excess K_2SO_4 salt was added to reduce the volume fraction of $CaMn_2(CO_3)_3$ in the product phase during mechanochemical synthesis so as to minimize particle agglomeration [9]. After the thermal decomposition of $CaMn_2(CO_3)_3$ into $CaMn_2O_4$, K_2SO_4 was removed by washing with deionised water (18 MΩ cm), using an ultrasonic bath and a centrifuge, until the total dissolved solid in the supernatant became less than 100 ppm. The washed powder was dried in an oven at 50°C for several hours.

6.2.2 Synthesis of $CaMn_2O_4$ nanowires

2 mmol of $CaCl_2$ (>93%, granular, anhydrous, Sigma Aldrich) and 2.8 mmol of $MnCl_2$ (99.9% Sigma Aldrich) were mixed in 10 mL of deionised water. In another beaker, 1.2 mmol of $KMnO_4$ (analytical grade, Univar) and 150 mmol of KOH (AnalaR NORMAPUR, VWR) were mixed in 10 mL of deionised water. Then the $KMnO_4$-KOH solution was added into the $CaCl_2$-

$MnCl_2$ solution dropwise, while stirring. A dark-brown precipitate was formed. The suspension was centrifuged to separate the precipitate from the supernatant. The remaining wet-cake was re-dispersed into 12 mL of ethanol and subjected to a hydrothermal treatment at 190°C for 40 h. The resulting precipitate was collected and washed 5-times with ethanol using a centrifuge and an ultrasonic bath.

6.2.3 Characterization techniques

The crystal structure of the powders was examined at room temperature using a Bruker X-ray diffraction instrument (XRD, D2 Phaser, USA) with Cu-Kα radiation of 1.54059 Å wavelength. The nanostructure and surface morphology of the powders were studied using a JEOL2100F field emission transmission electron microscope (TEM, JEOL, Japan) at 200 kV and also a Ultraplus field- emission scanning electron microscope (FESEM, Zeiss, Germany) at 1 kV. The specific surface area was measured by the Brunauer-Emmett-Teller (BET) N2-gas adsorption method using a TriStar II 3020 system (Micromeritics, USA). Prior to BET measurements, the powders were degassed under vacuum at 150 °C for 24 h. The bandgap energy of samples was estimated from UV-Vis optical absorption spectra taken using a Cary 60 spectrophotometer (Agilent, USA). Optical transmittance of the samples coated on a quartz plate was measured and the absorption spectra were converted into the Tauc plot of $(h\nu\alpha)^2$ versus hν, where h is the Planck's constant, ν is the photon's frequency, and α is the optical absorption coefficient. The linear zone of the Tauc curve was extrapolated to the energy axis to estimate the direct bandgap. X-ray photoelectron spectroscopy (XPS) was conducted using a SPECS PHOIBOS 100 Analyser installed in a high-vacuum chamber with a base pressure below 10–8 mbar. An incident monochromated X-ray beam of Al-Kα radiation with a photon energy of 1486.6 eV was used at 12 kV and 144 W. XPS binding energy spectra were recorded

at a pass energy of 20 eV and a step width of 0.05-0.1 eV in the fixed analyser transmission mode. To increase the signal/noise ratio, multi-scans were conducted and the signal intensity was accumulated. Broad survey scans were recorded at a pass energy of 60 eV and a step width of 0.5 eV. XPS data analysis was carried out using the commercial CasaXPS software package.

6.2.4 Preparation of $CaMn_2O_4$ electrodes on conducting glass slide

The method explained in Chapter 5 was used to prepare electrodes for photo-electrochemical water splitting.

6.2.5 Studies of $CaMn_2O_4$ electrode on FTO as OER photocatalysts

Working electrodes were placed within a fully-enclosed quartz cell (5 x 5 x 5 cm) inside a closed cabinet that comprised a Faraday cage. A Pt mesh (1 x 2 cm) was used as the counter electrode. A BASi Ag/AgCl aqueous salt bridge (KCl, 3 M) was used as a reference electrode. The cell was filled with a 0.2 M Na_2SO_4 aqueous solution electrolyte, adjusted to pH 12 by adding NaOH. The electrolyte was bubbled with N_2 gas for 30 min before each experiment. Linear sweep voltammetry (LSV) and chronoamperograms (CA) were performed using an EDAQ466 potentiostat. Where applicable, the sample was illuminated with a SoLux daylight MR16 halogen light bulb (12 V, 50 W, 24º; ca. 0.25 sun intensity) with a stable output range of 275 - 750 nm. The light was placed 10 cm from the working electrode. A Thorlabs visible-light bandpass filter (315-710 nm) was placed 1.5 cm in front of the light source to remove any heat (infra-red wavelengths) generated by the light source.

6.2.6 Qualitative analysis of evolved gas

A custom-built apparatus was used for photocurrent testing of samples on FTO glass with simultaneous gas analysis, as shown in Appendix III. The apparatus comprised a fully-enclosed electrochemical cell containing two sealed, half-cells whose electrolytes were separated only by a Nafion 117 proton exchange membrane (5 x 4 cm). The working electrode sample and a Ag/AgCl reference electrode were placed in the one half-cell whereas a platinum mesh electrode was placed in the other half cell. One wall of the former half-cell was a quartz sheet. The working electrode was illuminated using a SoLux daylight MR16 halogen light bulb. The electrode that contains irregular-shaped $CaMn_2O_4$ powders was connected to a potentiostat (CHI Instrument, USA). The gas outlets for the working and counter electrode half cells were connected to a dedicated Shimadzu GC-8A gas chromatograph (GC), via polymer-and-stainless-steel tubing. After fitting the electrodes, the electrolyte was poured into both half cells, which was bubbled with Ar gas overnight to make the cell air free without any external bias. In the gas streams passing through each half-cell, only Ar was detected, which also acted as a carrier gas for the connected GC throughout the photocurrent experiment. Thereafter, the Ar passing through each half cell was sampled, injected and analysed using the gas chromatograph, with the results plotted over 30 min of elution time. A voltage bias of 1.00 V (vs. Ag/AgCl) with and without light-illumination was then applied to the cell, whereafter the carrier gas was tested as described above, for electro-catalysis product gases using the GC. The identities of the gases in the carrier Ar were determined by their retention times.

6.3 Result and Discussion

6.3.1 Characterization of $CaMn_2O_4$ powder

Figure 6.1 shows the XRD pattern of the synthesized $CaMn_2O_4$ powders, where the diffraction peaks can be indexed to orthorhombic phase of $CaMn_2O_4$ (JCPDS card No 74-2293).

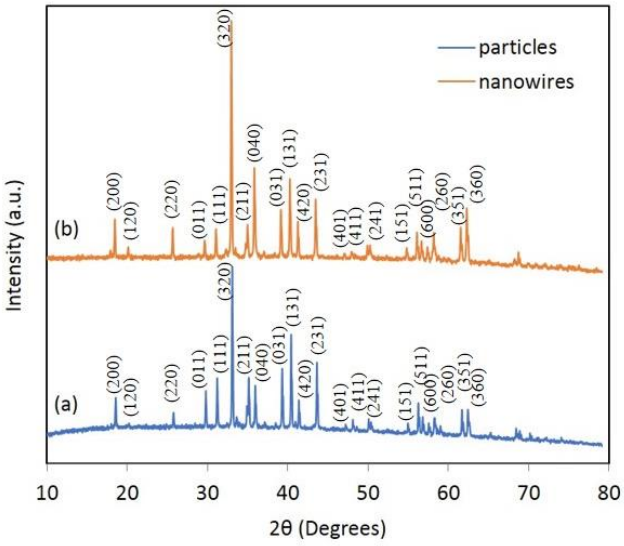

Figure 6.1. XRD patterns of (a) irregular-shaped $CaMn_2O_4$ particles, and (b) $CaMn_2O_4$ nanowires.

Figure 6.2 shows a typical SEM and TEM images of $CaMn_2O_4$ powders. The $CaMn_2O_4$ powder made by mechanochemical processing were irregular in shape with sizes from 200 nm to 2 µm (Figures 6.2a, 6.2b). The large particle sizes can be attributed to the higher temperature required to decompose the carbonate precursors. As evidenced in Figure 6.2c, irregular-shaped $CaMn_2O_4$ particles showed high crystallinity with clearly distinguished lattice fringes. The $CaMn_2O_4$ powder made using the hydrothermal method had wire shapes with diameters of ~500 nm and varying lengths (Figures 6.2d, 6.2e). The inset in Figure 6.2e shows the electron

diffraction pattern of the wires, from which the growth direction of nanowires was identified as [001] (Figure 6.2f). The BET surface areas of the irregular-shaped powder and nanowire powder were 4.7 m^2 g^{-1} and 5.4 m^2 g^{-1}, respectively.

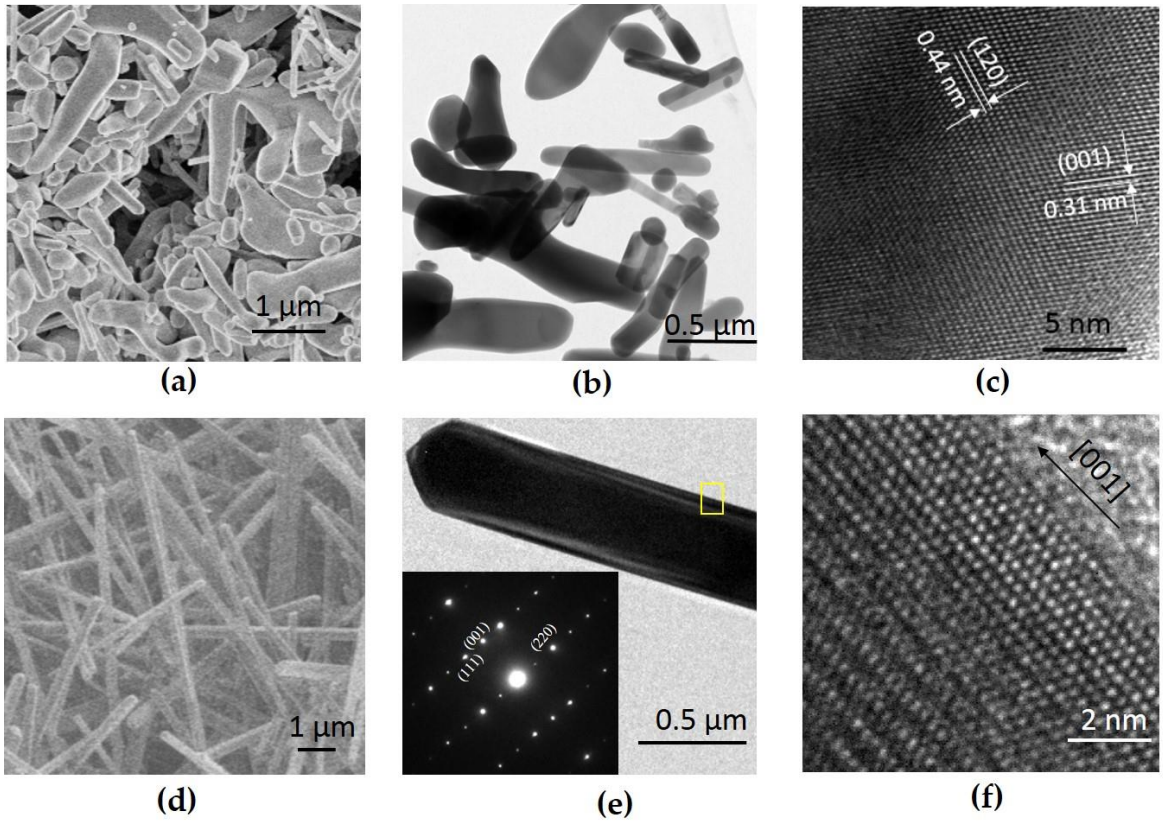

Figure 6.2. Electron micrographs of $CaMn_2O_4$ powder made by mechanochemical processing and subsequent heat treatment, (a) SEM, (b-c) TEM; and $CaMn_2O_4$ powder made using a hydrothermal method, (d) SEM and (e, f) TEM. The inset in Figure (e) is an electron diffraction pattern taken in the area indicated with a yellow square.

Figure 6.3 shows the XPS spectra of $CaMn_2O_4$ nanowires and irregular-shaped particles. As shown in Figure 6.3a, two strong peaks corresponding to $Mn2p_{3/2}$ and $Mn2p_{1/2}$ were observed at approximately 641 and 653 eV, respectively. Figure 6.3b shows the spectra near Mn3s peaks. Average oxidation state (AOS) was calculated using the linear relationship with splitting

energy between two Mn3s peaks [10]. AOS for irregular-shaped particles and nanowires was found to be 3.07 and 2.96, respectively, which is in good agreement with the theoretical value of 3.

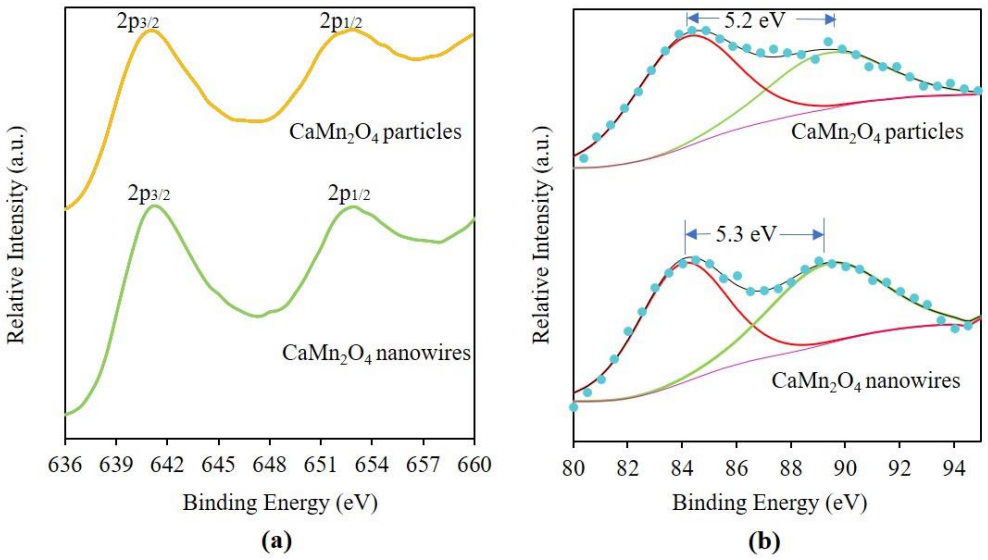

Figure 6.3. XPS spectra of irregular-shaped $CaMn_2O_4$ particles and $CaMn_2O_4$ nanowires; (a) Mn 2p and (b) Mn 3s regions.

Figures 6.4a and 6.4b show transmittance spectra of irregular-shaped $CaMn_2O_4$ particles and $CaMn_2O_4$ nanowires, respectively. The Tauc plots in Figures 6.4c and 6.4d suggests an optical band gap of 1.5 eV and 1.6 eV for irregular-shaped particles and nanowires, respectively.

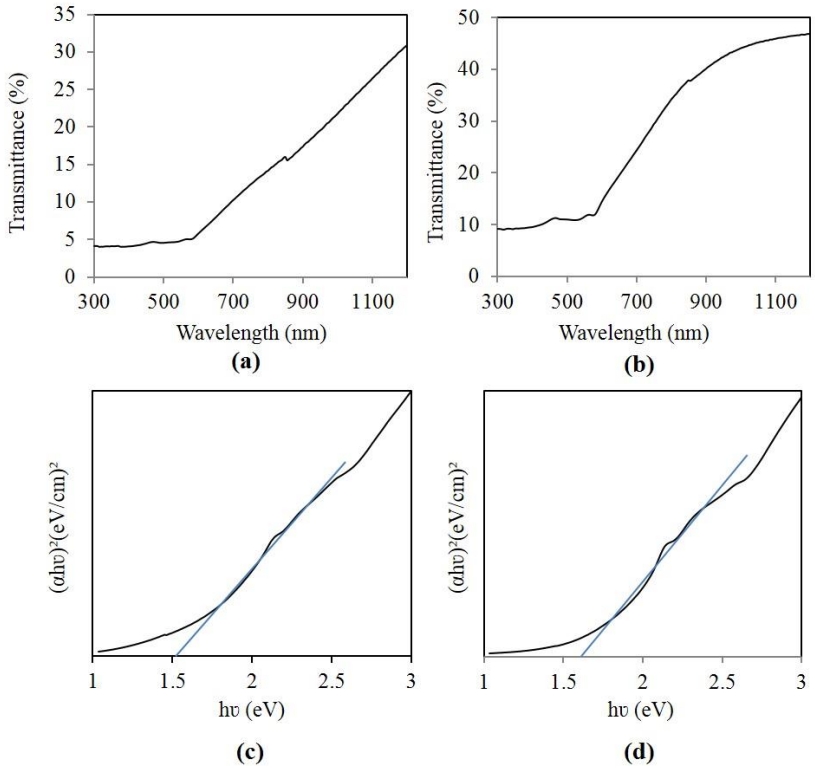

Figure 6.4. Transmittance spectra of (a) irregular-shaped $CaMn_2O_4$ particles and (b) $CaMn_2O_4$ nanowires; Tauc plots of (c) irregular-shaped $CaMn_2O_4$ particles and (d) $CaMn_2O_4$ nanowires.

6.3.2 Studies on Current Density

Figure 6.5 shows the electrocatalytic performance of the samples, tested in 0.2 M Na_2SO_4 aqueous solution, with the pH adjusted to 12, at 1.00 V (vs Ag/AgCl) bias, with and without light illumination.

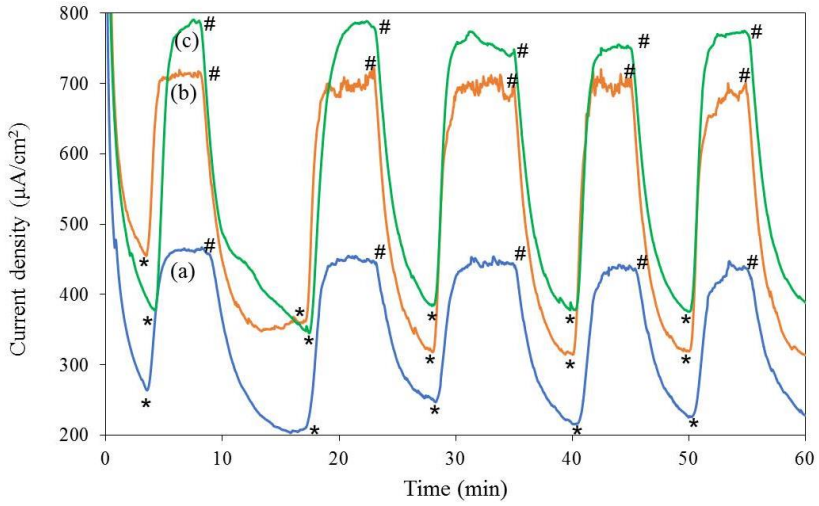

Figure 6.5. Chrono-amperograms at 1.00 V (vs Ag/AgCl) in 0.2 M Na_2SO_4 (pH 12) over 1 h of operation, with and without light illumination (0.25 sun), of FTO glass slides coated with thin films of: (a) polypyrrole only (control), (b) polypyrrole containing irregular-shaped $CaMn_2O_4$ particles, and (c) polypyrrole containing $CaMn_2O_4$ nanowires. (*='light on', #='light off').

As shown in Figure 6.5, a significant increase in both dark- and photo- current was observed for the PPy/$CaMn_2O_4$ films in comparison to the control PPy film alone. A significant increase in photocurrent was also observed when a small amount of $CaMn_2O_4$ powder was added to the PPy polymer. The control PPy film exhibited light and dark current densities of 447 µA cm^{-2} and 230 µA cm^{-2}, respectively, whereas the films prepared from the mixture of $CaMn_2O_4$ and PPy produced 701 µA cm^{-2} and 326 µA cm^{-2} for irregular-shaped particles, and 769 µA cm^{-2} and 380 µA cm^{-2} for nanowires in light and dark, respectively. It is also clear that the $CaMn_2O_4$ nanowires/PPy film produced higher dark and photocurrents than the irregular-shaped $CaMn_2O_4$/PPy film.

Table 6.1. Comparison between irregular-shaped $CaMn_2O_4$ powder and $CaMn_2O_4$ nanowires for BET specific surface area, increase in dark- and photo- current with regard to control electrode; BET specific surface area (S), dark current (I_D), photo-current (I_L), increase in dark current with respect to control (ΔI_D), increase in photo- current with respect to control (ΔI_L).

Electrode	S $m^2 g^{-1}$	I_D $\mu A\ cm^{-2}$	I_L $\mu A\ cm^{-2}$	ΔI_D $\mu A\ cm^{-2}$	ΔI_L $\mu A\ cm^{-2}$	$\Delta I_D/S$	$\Delta I_L/S$
Irregular-shaped particles/ PPy	4.7	326	701	96	254	20	54
nanowires/ PPy	5.4	380	769	150	322	28	60
PPy alone	N/A	230	447	N/A	N/A	N/A	N/A

Catalytic and photocatalytic activities occur on the surface of catalysts. Hence, in order to examine the intrinsic catalytic properties of materials, it is often convenient to normalize the indicators of photocatalytic activity with the specific surface area of materials. Table 6.1 compares the BET specific surface areas and increase in dark- and photo- current with regard to control electrode, between irregular-shaped $CaMn_2O_4$ powder and $CaMn_2O_4$ nanowires. Since the optical bandgap energies of irregular-shaped $CaMn_2O_4$ powder and $CaMn_2O_4$ nanowires are nearly the same, the differences in surface-area-normalized increase in photo-current, $\Delta I_L/S$, is expected to arise from the difference in particle shapes. Table 6.1 shows that, $\Delta I_L/S$ values of irregular-shaped $CaMn_2O_4$ powder and $CaMn_2O_4$ nanowires are similar to each other. The results suggest that the influence of particle shapes on the light-driven catalysis of $CaMn_2O_4$ is relatively weak. It is speculated that, the exposed facets along the growth-direction of nanowires do not have significantly different catalytic activities compared to the other crystal faces. On the other hand, the surface-area-normalized increase in photo-current, $\Delta I_D/S$, was higher for the electrode with nanowires than the electrode with irregular-shaped particles. The reason may be attributed to the difference in electric conductivity within the $CaMn_2O_4$/PPy

composite electrode. Rod- or wire- shaped particles have lower percolation threshold [11] and, given the semiconducting nature of $CaMn_2O_4$, wire-shaped particles will result in higher electrical conductivity than irregular-shaped particles in polymer composites.

6.3.3 Qualitative studies on the gas bubbles produced by the $CaMn_2O_4$/PPy electrodes

During the electrochemical reaction, gas bubbles were clearly visible on the $CaMn_2O_4$/PPy electrodes. Figure 6.6 shows the GC traces over 30 min of elution time for gases generated by the $CaMn_2O_4$/PPy films on FTO working electrode, with and without light illumination. In addition to the argon carrier gas, a large peak corresponding to oxygen was detected. A minor peak associated with hydrogen, which presumably crossed-over the Nafion membrane from the other half-cell, was also observed [12]. From the Figure 5.6, formation of hydrogen on anode also seems plausible due to more negative potential of PPy than H_2 generation. No other gas species was detected. Upon light illumination, the amount of O_2 relative to Ar increased.

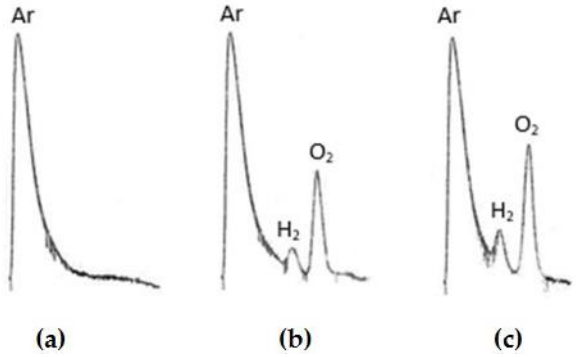

Figure 6.6. GC traces of collected gases (a) reference, (b) in the dark, and (c) under light irradiation.

6.3.4 EIS and Tafel Plot Studies

In order to investigate the nature of the catalytic process, electrochemical impedance spectroscopy (EIS) and Tafel plot studies were undertaken. EIS was conducted potentiostatically at 1.00 V (vs. Ag/AgCl) under the same conditions as the amperometric studies, with the same light source. Figures 6.7a and 6.7b show the Nyqist and Bode plots respectively, of the irregular-shaped particles/PPy film, the nanowires/PPy, and the control PPy electrodes without $CaMn_2O_4$, in the dark and under light illumination.

Following previous published work [12], the EIS data was modelled with the equivalent circuit shown in Figure 6.7c. The modelled results are depicted as the solid lines in Figure 6.7a. As can be seen, the modelled data yielded an excellent match with the measured data.

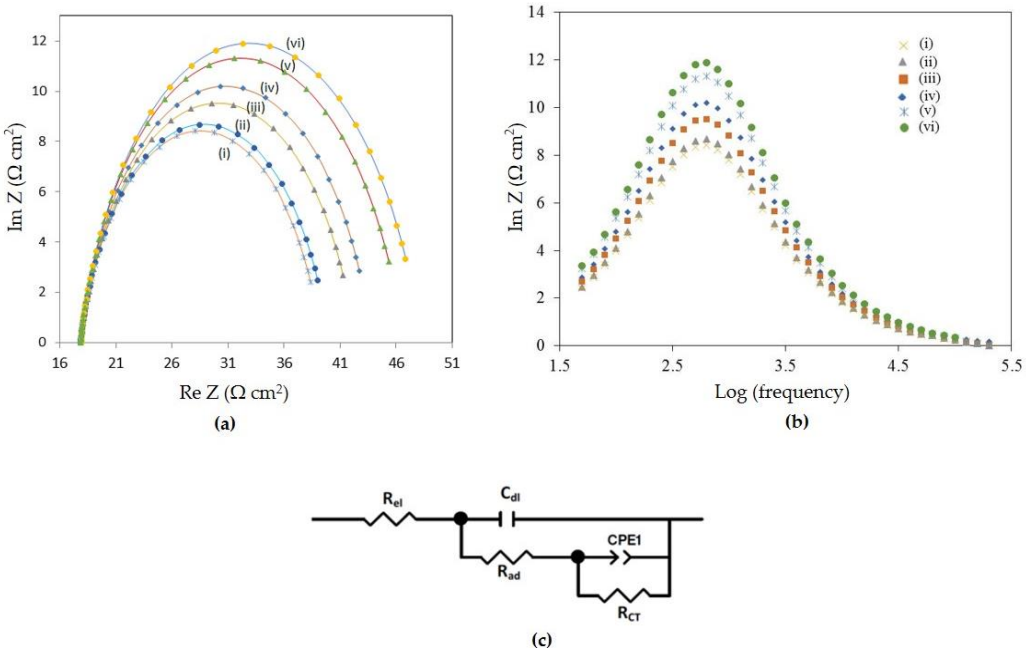

Figure 6.7. (a) Nyquist and (b) Bode plots showing measured data (individual data points) and modelled data (solid lines) using the equivalent circuit depicted in (c): (i) $CaMn_2O_4$ nanowires /PPy (with light illumination),(ii) $CaMn_2O_4$ nanowires / PPy (without light illumination), (iii)

irregular-shaped $CaMn_2O_4$ particles / PPy (with light illumination), (iv) irregular-shaped $CaMn_2O_4$ particles / PPy (without light illumination) (dark), (v) PPy only (with light illumination) and (vi) PPy only (without light illumination).

Table 6.2 shows the results derived from the modelling. It is evident from the Table 6.2 that C_{dl} was the highest for the $CaMn_2O_4$ nanowires/PPy sample. The capacitance C_{dl} is a comparative measure of the active area of the samples tested. Polypyrrole films exhibited the lowest values for C_{dl}. The higher catalytic performance of the $CaMn_2O_4$ nanowires/ PPy sample could therefore be attributed, at least in part, to a larger catalytically active area of nanowires.

Table 6.2. Data from electrochemical impedance spectroscopy (ohmic resistance (R_{el}), adsorption resistance (R_{ad}), diffuse layer capacitance (C_{dl}), catalytic charge transfer resistance (R_{CT}), and capacitance expressed in terms of a constant phase element (Q_{CPE}, n_{CPE}, and C_{CPE}). Data from Tafel plot studies (slope (A), exchange current density (i_o)). 'dark' = without light illumination; 'light' = with light illumination.

Sample	**R_{el}** Ω cm^2	**R_{ad}** Ω cm^2	**C_{dl}** µFc m^{-2}	**R_{CT}** Ω cm^2	**Q_{CPE}** $\mu\Omega^{-1}$ $cm^{-2}s^n$	**n_{CPE}**	**C_{CPE}** µF cm^{-2}	**A** mV/dec	**i_o** µA cm^2 x 10^{-4}
PPy (dark)	17.91	3.93	2.30	26.52	1.0687	0.74	0.013	41.308	4.53
PPy (light)	17.89	3.91	2.48	24.87	1.2032	0.74	0.015	39.667	3.47
Irregular-shaped particles/ PPy (dark)	17.88	3.69	2.78	22.85	1.527	0.74	0.020	39.224	1.92
Irregular-shaped particles/ PPy (light)	17.86	3.47	3.37	22.05	1.678	0.74	0.022	37.69	1.85
Nanowires/ PPy (dark)	17.84	2.42	5.86	19.81	2.757	0.74	0.040	37.099	1.16
Nanowires/ PPy (light)	17.83	2.37	6.02	19.19	3.276	0.74	0.051	36.747	1.07

In oxygen evolution (photo)electrocatalysis at pH 12, the catalytic performance may be controlled by reactant adsorption to the catalyst (with an associated resistance due to adsorption, R_{ad}) or by the fundamental catalytic turnover process (with an associated charge transfer resistance, R_{CT}) [12]. In the present study, operating at 1.00 V vs Ag/AgCl (compared to 0.8 V in previous studies [12]) appears to have made adsorption much less of an impediment than the catalytic turnover process, with the R_{CT} being, in all cases greater than the R_{ad}. Both the R_{CT} and the R_{ad} were low in comparison with previous conducting polymer films prepared by us [12]; this is to be expected from the higher applied bias.

Comparing the nanowires/PPy with the irregular-shaped particle/PPy, the resistances were marginally lower for the former than the latter, under both dark and light conditions, but of the same order as the control PPy film. The $CaMn_2O_4$ nanowires/PPy was therefore a slightly better catalyst than the irregular-shaped $CaMn_2O_4$ particles/PPy, particularly under light illumination. The ohmic resistance, R_{el}, was of the same order for all samples (17.83-17.91 Ω cm^2) (Table 6.2). Higher C_{dl} values were observed for both samples under light illumination. Hence the major effect of the light illumination appears to be the increase in the electrochemically active area of the films.

Figure 6.8 shows Tafel plots of the catalysts at much higher overpotentials than previously examined [12], with resulting data tabulated in the last two columns of Table 6.2. The exchange current density, i_o, provides a measure of the rate of catalysis at the reversible potential, when the overpotential is zero. The catalytic performance as a function of increasing bias, is given by the Tafel slope. As shown in Table 6.2, the higher applied potential also appears to have had a beneficial effect on the Tafel data, which were improved relative to previous studies [12]. The exchange current density and the Tafel slope of the prepared samples varied in the order

nanowires/PPy < irregular-shaped particles /PPy. However, the difference between the nanowires/PPy and irregular-shaped particles /PPy was insignificant, which explains nearly the same photocurrent produced by the samples. The slightly higher dark- and photo- current for the nanowires /PPy in comparison to irregular-shaped particles /PPy could be attributed to the higher electrochemically active area of the former relative to the latter.

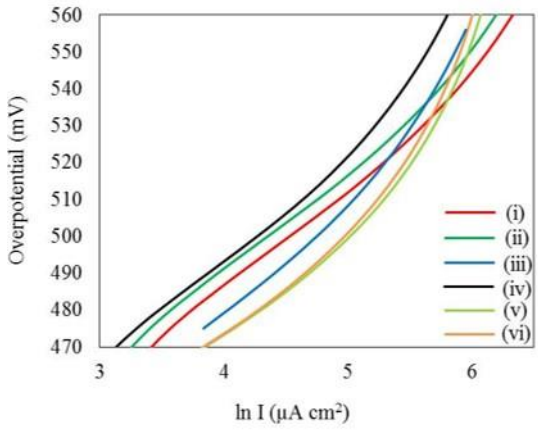

Figure 6.8. Tafel plots of (i) $CaMn_2O_4$ nanowires /PPy (with light illumination), (ii) $CaMn_2O_4$ nanowires /PPy (without light illumination, (iii) irregular-shaped $CaMn_2O_4$ particles /PPy (with light illumination), (iv) irregular-shaped $CaMn_2O_4$ particles /PPy (without light illumination) (dark), (v) PPy only (with light illumination) and (vi) PPy only (without light illumination).

6.4 Chapter summary

In the present study, $CaMn_2O_4$ ultrafine powders with different morphologies were synthesized and their catalytic performance in photo-electro-chemical water splitting was investigated. $CaMn_2O_4$ powders with irregular-shapes and nanowire shapes were synthesized using a dry mechanochemical method and a hydrothermal method, respectively.

To study their photo-electrocatalytic properties, $CaMn_2O_4$ powders were embedded within polypyrrole to form an anode in a photo-electrochemical cell. It was found that, irrespective of the morphology of $CaMn_2O_4$, the presence of $CaMn_2O_4$ in the electrode resulted in higher dark- and light- current, in comparison to the control without $CaMn_2O_4$. The evolution of O_2 gas from the electrode surface was also observed. Thus, $CaMn_2O_4$ showed a catalytic property in the water oxydation reaction. Upon light illumination, the current density was increased and the evolution of O_2 gas also increased, demonstrating the photocatalytic nature of $CaMn_2O_4$.

The electrode with $CaMn_2O_4$ nanowires exhibited higher dark- and light- current in comparison to the electrode with irregular-shaped $CaMn_2O_4$ particles. Electrochemical impedance spectroscopy studies revealed that the electrochemically active area increased in the order: PPy alone < irregular-shaped $CaMn_2O_4$ particles /PPy < $CaMn_2O_4$ nanowires /PPy, which was identified as a reason for the higher dark- and photo-current of $CaMn_2O_4$ nanowires/PPy electrode. However, surface-area-normalised data suggest that the influence of particle shapes on the light-driven catalysis of $CaMn_2O_4$ is relatively weak. The result suggests that the difference in catalytic activities among the crystal facets of $CaMn_2O_4$ may be rather small.

6.5 References

1. Ramírez, A., Bogdanoff, P., Friedrich, D. and Fiechter, S., 2012. *Synthesis of $Ca_2Mn_3O_8$ films and their electrochemical studies for the oxygen evolution reaction (OER) of water*. Nano Energy, 1, pp.282-289.
2. Najafpour, M.M., Pashaei, B. and Nayeri, S., 2012. *Calcium manganese (IV) oxides: biomimetic and efficient catalysts for water oxidation.* Dalton Transactions, 41, pp.4799-4805.
3. Najafpour, M.M., 2011. *Calcium-manganese oxides as structural and functional models for active site in oxygen evolving complex in photosystem II: Lessons from simple models.* Journal of Photochemistry and Photobiology B: Biology, 104, pp.111-117.
4. Najafpour, M.M., 2011. *Amorphous Manganese-Calcium Oxides as a Possible Evolutionary Origin for the $CaMn_4$ Cluster in Photosystem II.* Origins of Life and Evolution of Biospheres, 41, pp.237-247.
5. Gagrani, A. and Tsuzuki, T., 2019. *Calcium manganese oxides as biomimetic catalysts in energy applications: A short review*. Chemical Engineering Science, 194, pp.116-126.
6. Du, J., Pan, Y., Zhang, T., Han, X., Cheng, F. and Chen, J., 2012. *Facile solvothermal synthesis of $CaMn_2O_4$ nanorods for electrochemical oxygen reduction*. Journal of Materials Chemistry, 22, pp.15812-15818.
7. Najafpour, M.M., Ehrenberg, T., Wiechen, M. and Kurz, P., 2010. *Calcium Manganese (III) Oxides ($CaMn_2O_4 \cdot x\,H_2O$) as Biomimetic Oxygen-Evolving Catalysts.* Angewandte Chemie International Edition, 49, pp.2233-2237.
8. Peter, I.J., Praveen, E., Vignesh, G. and Nithiananthi, P., 2017. *ZnO nanostructures with different morphology for enhanced photocatalytic activity.* Materials Research Express, 4, 124003.
9. Tsuzuki, T., Pethick, K. and McCormick, P.G., 2000. *Synthesis of $CaCO_3$ nanoparticles by mechanochemical processing*. Journal of Nanoparticle Research, 2, pp.375-380.
10. Sun, M., Zhang, B., Liu, H., He, B., Ye, F., Yu, L., Sun, C. and Wen, H., 2017. *The effect of acid/alkali treatment on the catalytic combustion activity of manganese oxideoctahedral molecular sieves*. RCS Advances, 7, pp.3958-3965.
11. Schilling, T., Miller, M.A. and Van der Schoot, P., 2015. *Percolation in suspensions of hard nanoparticles: From spheres to needles*. EPL (Europhysics Letters), 111, 56004.
12. Alsultan, M., Balakrishnan, S., Choi, J., Jalili, R., Tiwari, P., Wagner, P. and Swiegers, G.F., 2018. *Synergistic Amplification of Water Oxidation Catalysis on Pt by a Thin-Film Conducting Polymer Composite.* ACS Applied Energy Materials, *1*, pp.4235–4246.

Chapter 7

Summary and future work

7.1 Summary

This thesis reports the investigation into the synthesis of ultrafine powders of manganese dioxide and calcium manganese oxides by mechanochemical processing and also their photocatalytic activities on dye degradation for the application as an anode in water splitting. The motivation behind the present study was to address research gaps in the field of bioinspired catalysts, by focusing on the following specific objectives:

1) To develop a new method to synthesise manganese-based oxides (amorphous and crystalline α-MnO_2, $Ca_2Mn_3O_8$, $CaMn_2O_4$, $CaMnO_3$) using mechanochemistry. Mechanochemical processing induces chemical reactions at near room temperature without help from hazardous organic solvents, and thus it is considered as a potentially green method to synthesise nanomaterials. MnO_2 was selected with an aim to understand the role of calcium in the catalytic process.
2) To determine band edge positions of calcium manganese oxides and investigate their photocatalytic performance in dye degradation.
3) To study their performance as a photo-anode in photo-electro-chemical cells for oxygen evolution through water splitting and elucidate the influence of structural similarity to the natural OEC, on water splitting.
4) To investigate the role of morphology of catalysts on photo-electro-chemical water splitting.

The study demonstrated a solvent-free method to synthesize manganese-based oxide catalysts. MnO_2, $Ca_2Mn_3O_8$, $CaMn_2O_4$ and $CaMnO_3$ ultrafine particles were successfully synthesized in two steps; mechanochemical processing and subsequent heat treatment. In the first step, a solid-

state displacement reaction between a calcium salt, a manganese salt and K_2CO_3 resulted in the formation of $Ca_xMn_{1-x}CO_3$ nanoparticles. The second step involved the thermal decomposition of $Ca_xMn_{1-x}CO_3$ nanoparticles into $Ca_xMn_{1-x}O_y$. During the heat treatment, particles were embedded within a solid salt matrix that acted as a physical barrier between nanoparticles. This prevented particle agglomeration, resulted in higher surface areas of catalysts compared to the previously reported dry synthesis methods. In general, particles with high surface areas offer more catalytic reaction sites, thus offer an improved efficiency during catalytic application. It signifies the importance of using this synthesis technique to evaluate the catalytic and photocatalytic performance of manganese-based oxides [1]. The synthesis approach can also be applied to producing other high performing semiconductor photocatalysts for energy and environmental applications.

The study of band-edge position and bandgap energy revealed that, theoretically, the selected manganese-based oxide catalysts can absorb the visible solar spectrum, degrade organic pollutants by free-radical generation, and generate oxygen through photo-electro-catalytic water splitting. However, experimentally, at pH 7, manganese oxides and calcium manganese oxides showed poor charge transfer efficiency, leading to poor photocatalytic dye degradation. Poor photocatalytic degradation was also partially attributed to the photo absorption by dye molecules and intrinsic properties of the catalysts, including crystal structure and physiochemical properties. Nonetheless, the results showed the capability of the compounds to act as a photocatalyst. Lowering the pH to 3 resulted in increased dye decolourisation under dark and light conditions, which was attributed to the reductive dissolution of manganese compounds and photo corrosion.

For the study of photo-electrochemical water splitting, polypyrrole, a conducting polymer, was used along with catalyst powders in the anode of a photo-electrochemical cell. The combination of polypyrrole and manganese-based catalysts was effective in increasing charge separation efficiency and providing structural stability to the electrode. Among all tested compounds, $CaMn_2O_4$ showed the highest photocurrent. Samples containing calcium atoms performed better than the ones without calcium. The study showed that having a cubane like shape of calcium manganese oxide may play an important role in water splitting. However, overall catalytic activities are influenced by numerous factors and thus further research is required to elucidate the role of calcium and structural similarity to the natural OEC cubane. This study also found that oxygen evolution catalysis by $CaMn_2O_4$ is affected more by surface area than particle morphology [2].

In summary, this work has contributed to the research field of bio-inspired photocatalysts. The study demonstrated an environmentally friendly and scalable platform technology for the low-cost fabrication of manganese-based oxide photocatalysts and the engineering of PEC water splitting devices using the bio-inspired catalysts. New knowledge about the manganese-based oxide photocatalysts including bandgap energy and band edge positions was obtained. New understanding about their catalytic and photocatalytic water oxidation performance was developed. These findings will be helpful in designing sustainable technologies for the environment.

7.2 Future work

This thesis has demonstrated for the first time a simple, low-cost and green synthesis approach for bio-inspired photocatalysts and demonstrated their application in photo-electrochemical

oxygen evolution by water splitting. However, many opportunities for extending the scope of this thesis remain. This section presents some of these directions.

7.2.1 Optimisation of water splitting parameters

In the fifth and sixth chapter of this thesis, the oxygen evolution ability of manganese-based oxides has been investigated at fixed parameters. Further studies regarding fine tuning and optimization of various parameters, for example light intensity, voltage, pH and concentration of the electrolyte, would be significantly useful in advancing the knowledge in the field of water splitting using these catalysts. In addition, the future studies regarding mechanism of water splitting by detailed electrochemical impedance spectroscopy studies and determination of rate determining steps would be very useful. Upon optimisation, comparison with a benchmark material such as Pt should also be conducted.

7.2.2 Reusability/long term stability of catalyst

The main purpose of this thesis was to demonstrate the photocatalytic ability of bio-inspired manganese-based catalysts along with their application in a PEC cell. Therefore, the catalysts were tested for only one cycle during dye degradation experiments and for only 1 h during oxygen evolution experiment. However, for practical purposes, it is critical to retain high performance of the catalysts in long-cyclic runs. Therefore, further studies are required to demonstrate reusability of the catalyst in the dye degradation experiments and long-term stability of the photo anodes in the oxygen evolution experiments.

7.2.3 Role of calcium

The role of Ca in photo-induced water splitting by calcium-manganate ceramics has not been fully studied. Elucidating the catalytic role of calcium in calcium-manganate ceramics is important not only for optimising their water-oxidation activities but also for advancing our understanding of the mechanism of natural photosynthesis. For this, it is important to develop techniques to synthesise structurally well-defined Ca–Mn–O systems with the ability to tailor the surface characteristics such as the concentration of Ca [3]. Alternatively, Mechanochemical synthesis using non-stoichiometric mixture of raw materials may allow the formation of Ca–Mn–O systems with controlled calcium deficiency.

7.2.4 Role of manganese oxidation state

In the present study, manganate compounds with manganese oxidation state of 3 and 4 were investigated. In natural photosynthesis, it is believed that the oxidation states of manganese in Mn_4Ca cubane have significant influence on water splitting [4]. Modification of the oxidation states of the Mn ions and creation of oxygen vacancies in the $CaMn_xO_y$ nanoparticles without altering crystal structure, will not only influence optical bandgap energy and modify the photon-capture efficiency, but also modify electric conductivity, thus contributing to photocatalytic efficiency. The influence of manganese oxidation state between 3 and 4 or even below 3, may shed new light on the role of manganese oxidation states in the photocatalysis. The reduction of oxidation states in Mn ions and creation of oxygen vacancies without changing crystal structure may be possible by annealing the synthesised nanoparticles in an inert gas atmosphere or under reducing gases.

7.2.5 Facet engineering

Catalytic and photocatalytic reactions occur on the surface of manganate particles. The crystal facets exposed on the particle surface can play critical roles in determining catalytic activity. Each facet consists of a crystal plane with a unique atomic arrangement, coordination environment, and electrochemical potential [5]. As such, each facet has specific catalytic activity and reaction-selectivity. Facet engineering is equivalent to the morphology-controlled synthesis of nanoparticles. The desired facets or crystal planes may be selectively exposed on the particle surface by tuning the growth rates of nano-crystallites along specific crystal orientations. In this study, we were able to create only two different morphologies to $CaMn_2O_4$. It will be interesting to develop synthesis techniques to create different morphologies and compare their light-driven water-splitting properties. This will help tailor the water-splitting efficiency as well as elucidate the role of calcium in the water-splitting process.

7.2.6 Role of local atomic arrangement

The similarity in the local structure of manganate compounds may come into play in many forms, not only the dependence of facets exposed on the particle surface but also the difference in the oxidation states of each manganese ions in the structure. For the study of the local structure of manganate compounds, the use of computational chemistry such as density functional theory could be useful to explore the potential water splitting catalytic pathways in the manganate materials. The computational analysis will rationalise the observed experimental performances and identify promising avenues for structural modification to optimise water-splitting performance.

7.2.7 Different calcium manganese oxides

Biomimetic photocatalytic water splitting is an emerging technology for addressing the future energy demands. In this thesis, three calcium manganese oxides were selected, based on their local atomic arrangement. Several other calcium manganese oxides, such as $CaMn_3O_6$, $CaMn_4O_8$ etc., with varying crystal structure and manganese oxidation states, can be very interesting and appealing for solar fuel production [3, 6]. Thus, their synthesis and photocatalysis could be suited for a dedicated follow-up study. In that case, this research area can be greatly benefitting from the development of efficient biomimetic catalysts.

7.2.8 Other applications

Recently calcium manganese oxides have been demonstrated to be effective catalysts in several applications, including metal air batteries [3]. However, there is much room for further improvement by, for example, using different stoichiometric Ca–Mn–O systems, introduction of defects and impurities, nanomization, and facet-engineering. Further, electrochemical performance of metal-air batteries is affected by several factors, such as nature of electrolyte, solvent, morphology of cathode material, amount of active material on cathode, pressure of air/oxygen [7]. In this regard, further research is necessary to fully understand the potential and limitations of calcium manganese oxides in metal-air battery applications.

Ca–Mn–O systems have unique redox-catalytic activities, which may be useful as an electrode material in supercapacitance. However, no study on the application of Ca–Mn–O systems in supercapacitors has been reported to date [2].

7.3 References

1. Gagrani, A., Zhou, J. and Tsuzuki, T., 2018. *Solvent free mechanochemical synthesis of MnO_2 for the efficient degradation of Rhodamine-B*. Ceramics International, 44, pp.4694-4698.
2. Gagrani, A., Alsultan, M., Swiegers, G.F. and Tsuzuki, T., 2019. *Photo-Electrochemical Oxygen Evolution Reaction by Biomimetic $CaMn_2O_4$ Catalyst*. Applied Sciences, 9, p.2196.
3. Gagrani, A. and Tsuzuki, T., 2019. *Calcium manganese oxides as biomimetic catalysts in energy applications: A short review*. Chemical Engineering Science, 194, pp.116-126.
4. Sproviero, E.M., Shinopoulos, K., Gascon, J.A., McEvoy, J.P., Brudvig, G.W. and Batista, V.S., 2007. *QM/MM computational studies of substrate water binding to the oxygen-evolving centre of photosystem II*. Philosophical Transactions of the Royal Society B: Biological Sciences, 363, pp.1149-1156.
5. Liu, G., Jimmy, C.Y., Lu, G.Q.M. and Cheng, H.M., 2011. *Crystal facet engineering of semiconductor photocatalysts: motivations, advances and unique properties*. Chemical Communications, 47, pp.6763-6783.
6. Barrocas, B., Sério, S., and Jorge, M.M., 2014. *Hierarchically Grown $CaMn_3O_6$ Nanorods by RF Magnetron Sputtering for Enhanced Visible-Light-Driven Photocatalysis.* The Jounal of Physical Chemistry C, 118, pp.24127-24135.
7. Christensen, J., Albertus, P., Sanchez-Carrera, R.S., Lohmann, T., Kozinsky, B., Liedtke, R., Ahmed, J. and Kojic, A., 2011. *A critical review of Li/air batteries. Journal of the Electrochemical Society*, 159, pp.R1-R30.

Appendix I

pH dependent catalytic redox properties of Mn_3O_4 nanoparticles

Appendix I

Materials Chemistry and Physics 231 (2019) 41–47

Contents lists available at ScienceDirect

Materials Chemistry and Physics

journal homepage: www.elsevier.com/locate/matchemphys

pH dependent catalytic redox properties of Mn_3O_4 nanoparticles

Ankita Gagrani, Bolun Ding, Yang Wang, Takuya Tsuzuki*

Research School of Engineering, Australian National University, Canberra, ACT, 2601, Australia

HIGHLIGHTS

- Mn_3O_4 nanoparticles were synthesised by a green method.
- Effect of pH on the catalytic redox properties of Mn_3O_4 was reported.
- Mechanism of the pH dependent redox catalytic property was proposed.

ARTICLE INFO

Keywords:
Manganese oxide
Nanoparticles
Antioxidant
Dye degradation
Mechanochemical processing

ABSTRACT

Manganese-based materials have unique redox properties, attractive to many applications in the energy, environment and biomedical sectors. In particular, Mn_3O_4 is known to act as both an oxidising and a reducing agent. However, pH-dependence of the redox properties of Mn_3O_4 nanoparticles is not yet well understood. In this study, Mn_3O_4 nanoparticles were mechanochemically synthesised and their redox catalytic activities were studied under different pH conditions. Mn_3O_4 nanoparticles with sizes between 10 and 90 nm were prepared via a mechanically-induced solid-state displacement reaction between $MnCl_2$ and K_2CO_3 and subsequent heat treatment. The effect of pH on the oxidative decomposition of a model organic dye revealed that Mn_3O_4 nanoparticles showed oxidative catalytic activity only when pH was below 5. At a higher pH, Mn_3O_4 nanoparticles showed strong free-radical scavenging activities, suitable for reducing oxidative stress in many locations of the body and for creating new design of energy-storage materials.

1. Introduction

Redox catalysts have significant importance in the applications related to sustainable development, including renewable energy, chemical manufacture, environmental remediation and health security [1]. In particular, manganese oxides have attracted increasing scientific interests because of its earth-abundant and inexpensive nature of the constituent elements that is advantageous in sustainability-related applications [2].

Due to the multivalent nature of manganese, manganese oxides exhibit structurally diverse systems. Among them, Mn_3O_4 is a spinel-structured stable oxide with unique magnetic, catalytic and electrochemical properties [3–5]. Its redox properties were utilised as a thermochemical energy storage material [6] and a supercapacitor electrode [7]. Its oxidative catalytic and photocatalytic properties were used in electrochemical water splitting to generate hydrogen fuel [8], photodecomposition of organic pollutants in water [9], and removal of CH_4 and CO to reduce air pollution [10,11]. For those applications, nanoscale Mn_3O_4 is advantageous due to the high specific surface area. The potential applications of Mn_3O_4 nanoparticles in the biomedical sector was also recognised recently. Mn_3O_4 is found biocompatible [12]. Karunakaran et al. showed excellent antioxidant and antimicrobial activities of Mn_3O_4 nanoparticles [13]. Free radicals induce oxidative damage to biomolecules which leads to many diseases including atherosclerosis, ageing, cancer, diabetes mellitus, and inflammation [14]. As such, Mn_3O_4 nanoparticles with antioxidative and free-radical scavenging properties can be used to treat many diseases such as hepatic fibrosis [15].

Of particular interest is that Mn_3O_4 acts as both an oxidising agent and a reducing agent, or a free-radical scavenger and generator [16]. Whether Mn_3O_4 acts as a reducing agent or an oxidising agent depends on the redox condition of the environment, such as the presence of other oxidants or reducing agents. However, the influence of pH on the redox activities of Mn_3O_4 has not been investigated, despite its importance in many applications. For example, therapeutic agents experience various pH levels in different locations in the body and hence it is critical to understand the effect of pH on free-radical scavenging activities [17]. The pH of waste water and electrolyte in

* Corresponding author.
E-mail address: takuya.tsuzuki@anu.edu.au (T. Tsuzuki).

https://doi.org/10.1016/j.matchemphys.2019.04.017
Received 5 October 2018; Received in revised form 25 March 2019; Accepted 5 April 2019
Available online 08 April 2019
0254-0584/

Appendix I

supercapacitors and water-splitting cells also varies and potentially influences oxidative catalytic properties of Mn_3O_4. In this work, the pH dependence of oxidative dye degradation and free-radical scavenging properties of Mn_3O_4 was studied using nanoparticles.

In order to realize industrial applications of manganese-oxide catalysts, it is critical to develop sustainable and scalable production techniques and to determine their catalytic properties under real-life conditions. In the present study, Mn_3O_4 nanoparticles were synthesised by thermal decomposition of $MnCO_3$ nanoparticles that was produced by dry mechanochemical processing. Mechanochemical processing has long been used as a green synthesis method for a wide range of nanoparticles [18]. The technique utilises a ball mill as a chemical reactor wherein reactions are induced into a powder charge by the input of mechanical energy though the collision events of grinding media. This process does not require the use of organic solvents and high temperature processes, thus is considered as a potentially green synthesis method [19].

In dry milling, the solid phase acts as a physical barrier between nanoparticles during the particle-growth stage, which limits the formation of particle agglomeration [20]. As such, dry mechanochemical processing can produce nanoparticles with low degrees of agglomeration and high specific surface areas. The resulting characteristics are suitable for evaluating the catalytic properties of materials. In this regard, for the investigation of pH-dependent free radical generation/scavenging properties of Mn_3O_4 nanoparticles, mechanochemical processing has an advantage over other synthesis methods such as liquid-based [21–23] or vapour-phase synthesis techniques [24]. Chen et al. produced Mn_3O_4 via a mechanochemical reaction, but they used Mn powder and water instead of dry milling. As a result, the resulting particles showed a high degree of agglomeration [25]. To the best of our knowledge, no study has been reported on the dry synthesis of well-dispersed Mn_3O_4 nanoparticles by mechanochemical processing.

2. Materials and methods

2.1. Preparation of Mn_3O_4 nanoparticles

First, $MnCO_3$ nanoparticles were synthesised by dry mechanochemical processing via the reaction $MnCl_2 + K_2CO_3 \rightarrow MnCO_3 + 2KCl$. Stoichiometric amounts of $MnCl_2$ (99.9%) and K_2CO_3 (AnalaR NORMAPUR) dry powders were placed in a sealed steel vial with hardened steel balls of 9.2 mm in diameter. For the purpose of limiting nanoparticle agglomeration, KCl powder (AnalaR NORMAPUR) was also added to the starting powder mixture as an inert diluent, with the amount that the volume fraction of $MnCO_3$ in the product phase is 10% [20]. All the chemicals were used without further purification. A ball-to-powder weight ratio of 10:1 was used throughout the investigation. Milling was performed for 4 h in a SPEX 8000 M mill. In order to thermally decompose $MnCO_3$ nanoparticles while dispersed in the KCl solid matrix, the as-milled powder was heat treated at 200 °C, 400 °C and 600 °C for 1 h under a nitrogen gas atmosphere and then the sample was allowed to cool down to room temperature in air. After heat treatment, KCl was washed away with deionised water using an ultrasonic bath and a centrifuge. The remaining brown powder was dried in an oven at 50 °C for 8 h.

The structure and crystal phase of the powder were examined using a D_2 Phaser X-ray diffractometer (XRD: Bruker USA) with Cu-Kα radiation. Thermogravimetric analysis (TGA) was carried out using a STA 8000 simultaneous thermal analyser (PerkinElmer, USA) under a constant nitrogen flow of 100 ml min^{-1} with a heating rate of 10 °C min^{-1}.

X-ray photoelectron spectroscopy (XPS) was conducted using a SPECS PHOIBOS 100 Analyser installed in a high-vacuum chamber with a base pressure below 10–8 mbar. An incident monochromated X-ray beam of Al-Kα radiation with a photon energy of 1486.6 eV was used at 12 kV and 144 W. XPS binding energy spectra were recorded at a pass energy of 20 eV and a step width of 0.05–0.1 eV in the fixed analyser transmission mode. To increase the signal/noise ratio, multi-scans were conducted and the signal intensity was accumulated. Broad survey scans were recorded at a pass energy of 60 eV and a step width of 0.5 eV. XPS data analysis was carried out using the commercial CasaXPS software package.

The nanostructure and surface morphology of the powder were investigated using a CM300 transmission electron microscope (TEM: Philips, Netherland) at 300 kV. For TEM analysis, the nanoparticles were dispersed in ethanol and a drop of the suspension was placed on a carbon-coated copper grid. The specific surface area of the nanoparticles was measured by the Brunauer-Emmett-Teller (BET) N_2-gas adsorption method using a TriStar 3020 (Micromeritics, USA). Prior to BET measurements, dry nanoparticles were degassed at 150 °C for 24 h. An average particle size was estimated from specific surface area using the equation

$$D_{BET} = 6000/(\rho A) \quad (1)$$

where A is specific surface area in m^2g^{-1}, ρ is the theoretical density of Mn_3O_4 expressed in g/cm^3 and D_{BET} is the diameter of particles in nm [26]. UV–Vis absorption spectra were measured using a Cary 60 spectrometer (Varian, USA). The band gap energy of Mn_3O_4 nanoparticles was estimated by converting the UV–Vis absorption spectra into Tauc plots [27]. Zeta Potential of Mn_3O_4 particles, dispersed in different pH solutions, was measured using a Zetasizer-Nano-S dynamic light scattering device (Malvern, USA). The isoelectric point of Mn_3O_4 was determined from the zeta potential curve.

2.2. pH-dependence of free radical scavenging activity

The free radical scavenging activity of Mn_3O_4 nanoparticles was investigated using 2,2′-azino-bis(3-ethylbenzothiazoline-6-sulphonic acid) (ABTS) radical at different pH [28]. An ABTS stock solution was prepared by adding 20 mg ABTS in 5 ml water. To this solution, 3.4 mg potassium persulfate was added to generate ABTS radical cations ($ABTS^{\cdot+}$) and the mixture was left for 16 h in the dark at room temperature. 50 ml of DI water was taken in different beakers and 1.2 ml of ($ABTS^{\cdot+}$) solution was added to each of them. The pH of the solutions was adjusted using 0.1 M HCl. The pH range from 3 to 9 was investigated to cover most of the pH conditions in the human body. Subsequently, 8 mg of nanoparticles were dispersed in the solution and 4 ml solution was taken out at a regular interval and centrifuged at 12,000 rpm for 10 min to separate Mn_3O_4 nanoparticles. Optical absorbance of the solution was measured using a Cary 60 spectrophotometer (Agilent, USA) at 734 nm. The percentage for scavenging ABTS radicals was calculated using the following equation:

$$\% \text{ decolorization} = [1 - (\text{Absorbance}_{60min}/\text{Absorbance}_{0min})] \times 100 \quad (2)$$

2.3. pH-dependence of oxidative dye degradation

In order to investigate the oxidation property of Mn_3O_4 nanoparticles, oxidative degradation of Rhodamine-B (RhB) dye was studied. First, 50 ml of RhB solution with a concentration of 0.01 mg ml^{-1} was taken in a silica beaker. The pH of the initial solution was measured and adjusted using 0.1 M HCl. The pH range from 3 to 9 was investigated to cover most of the pH conditions in the human body. Then 8 mg of Mn_3O_4 powder was dispersed in the RhB solution using an ultrasonicator. A low-density polyethylene film (> 85% transparent to UVA and UVB) was placed to seal the beaker to prevent water evaporation. No other oxidising agent was added. Aliquots (4 ml) were collected at various irradiation times and centrifuged at 12,000 rpm for 10 min to remove Mn_3O_4 nanoparticles from the RhB solution. Degradation of RhB was monitored by measuring the optical absorption spectra of the RhB solution using a Cary 60 spectrophotometer (Agilent,

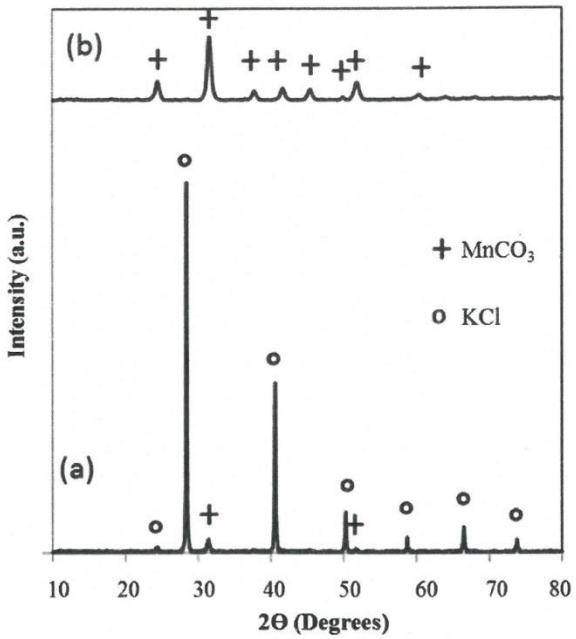

Fig. 1. XRD patterns of (a) an as-milled powder after milling for 4 h and (b) a powder after washing and drying.

USA). Since the peak position of the characteristic light absorption spectrum of RhB shifts depending on pH, the degradation of RhB was studied by considering the total area under the absorption peak in the wavelength range from 450 to 600 nm, instead of the absorbance intensity at a particular wavelength.

To understand the effect of light irradiation on the dye degradation reaction, the suspension was also irradiated with simulated sunlight using a Suntest CPS + instrument (Atlas, USA) equipped with a 1500 W Xenon lamp and a daylight filter. The irradiation intensity was 65 W m^{-2} over the wavelength range of 300–800 nm. Aliquots (4 ml) were collected at a regular interval and degradation in the presence of light was measured using the same procedure as without light irradiation, as mentioned above.

3. Results and discussion

3.1. Synthesis of Mn_3O_4 nanoparticles

Fig. 1(a) shows an XRD pattern of the as-milled powder after milling for 4 h. Prominent diffraction peaks can be indexed to KCl (JCPDS #41–1476) along with minor peaks associated with $MnCO_3$. Fig. 1(b) shows an XRD pattern of the powder after washing to remove KCl. The diffraction peaks can be indexed to $MnCO_3$ (JCPDS #86–0173). The result indicates that $MnCO_3$ was formed through the reaction $MnCl_2 + K_2CO_3 \rightarrow MnCO_3 + 2KCl$ during milling. Fig. 2 shows a TGA curve of the powder milled for 4 h. The weight change until 200 °C can be attributed to moisture loss. A decline in weight is evident between 250 °C and 600 °C. Theoretically, the decomposition of $MnCO_3$ into Mn_3O_4 results in 33.6% of weight loss due to the formation of CO_2 gas. By the time the temperature reached 600 °C, a weight loss of 32.1% was observed, which is indicative of the decomposition of $MnCO_3$ into Mn_3O_4.

Fig. 3 shows XRD patterns of the powder heat-treated at 200 °C, 400 °C, and 600 °C for 1 h and subsequently washed to remove KCl. The pattern of the sample heat-treated at 200 °C consisted of peaks corresponding to $MnCO_3$ only. Heat treatment at 400 °C resulted in a mixture of $MnCO_3$ and Mn_3O_4. After heat treatment at 600 °C, no other peaks except Mn_3O_4 (JCPDS # 80–0382) were evident in the XRD pattern. The result indicates the gradual decomposition of $MnCO_3$ into Mn_3O_4 within the wide temperature range between 200 °C and 600 °C. The

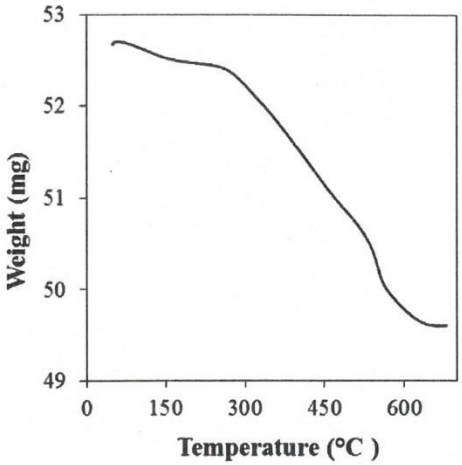

Fig. 2. TGA curve of the as-milled powder after milling for 4 h.

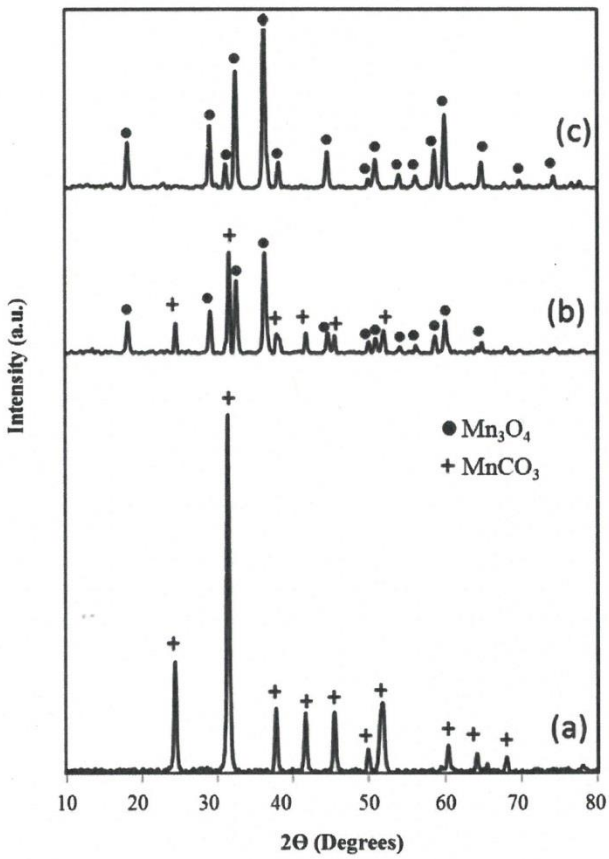

Fig. 3. XRD patterns of the powders heat treated under N_2 at (a) 200 °C, (b) 400 °C, and (c) 600 °C for 1 h and subsequently washed.

result is in good agreement with the TGA data.

The chemical composition of the Mn_3O_4 particles was also analysed by XPS. Fig. 4(a) shows that Mn 2p1/2 and Mn 2p3/2 peaks were centred at 652.7 and 641.0 eV, respectively. The spin energy separation between the binding energy peaks of Mn 2p1/2 and Mn 2p3/2 was 11.7 eV, which was in good agreement with the previous report on Mn_3O_4 [29]. The binding energy of the Mn 2p3/2 peak components was 640.5 and 642.8 eV, which could be attributed to the Mn 2p3/2 of MnO and MnO_2, respectively [29,30]. Fig. 4(b) shows the XPS spectrum in the O 1s region, where the peak could be deconvoluted into three peaks. The peak located at 529.4 eV could be attributed to lattice oxygen in Mn_3O_4 [29,30], and peaks at 531 and 532.8 eV were present due to

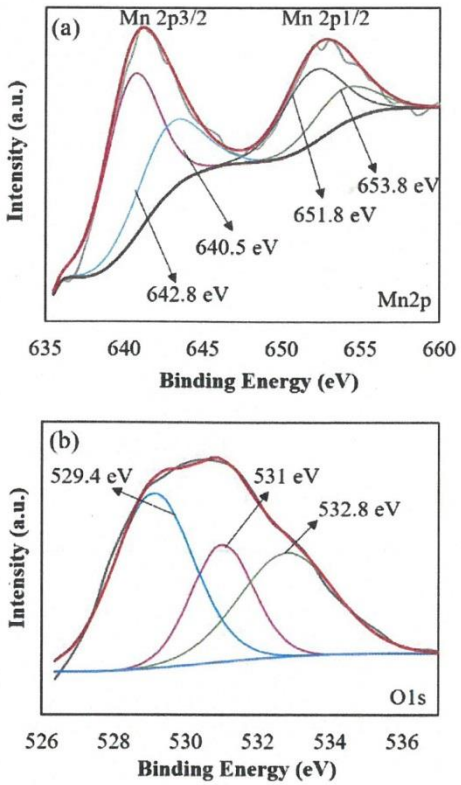

Fig. 4. Fitted XPS spectra of Mn_3O_4 for (a) Mn 2p and (b) O1s regions.

hydroxyl groups on the surface and water, respectively [31]. The total manganese-to-oxygen ratio (Mn/O) in the lattice was 0.72, which was close to the theoretical value of 0.75. Therefore, XPS further confirmed that the resulting particles were Mn_3O_4.

Fig. 5(a) shows a TEM micrograph of the $MnCO_3$ powder. The powder consisted of nanoparticles of 5–20 nm in diameter and some agglomerates of up to 100 nm. The small particle sizes are typical feature of dry mechanochemical processing using solid-state displacement reactions [26]. Fig. 5(b) shows a TEM micrograph of Mn_3O_4 powder. The powder consisted of crystalline nanoparticles of 10–90 nm in size and the majority of the particles are in the size range between 20 and 50 nm. The formation of large Mn_3O_4 particles may have resulted from agglomerated $MnCO_3$ particles.

The BET surface area of the Mn_3O_4 powder was 42.3 m^2g^{-1}, which corresponds to a spherical particle size of 29 nm. The average crystallite size estimated using the Scherrer equation [32] from the diffraction peaks between 29° and 38° was 23 nm. These particle sizes estimated from various methods were in reasonable agreement with each other, which indicates a relatively low degree of particle agglomeration [33].

Fig. 6 shows the optical absorption coefficient in the form of $(\alpha h\nu)^2$ versus $h\nu$ for Mn_3O_4 nanoparticles, where h is the Planck's constant, ν is the photon's frequency, and α is the absorption coefficient. The intercept of the straight line with the x-axis (energy axis) indicates an optical

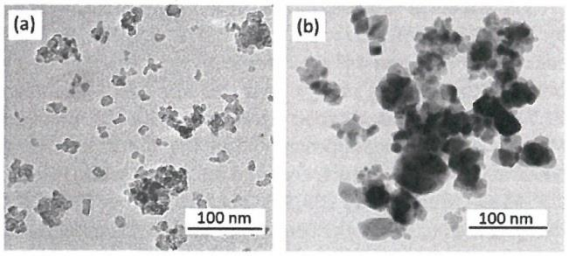

Fig. 5. TEM micrographs of (a) $MnCO_3$ and (b) Mn_3O_4 nano powders.

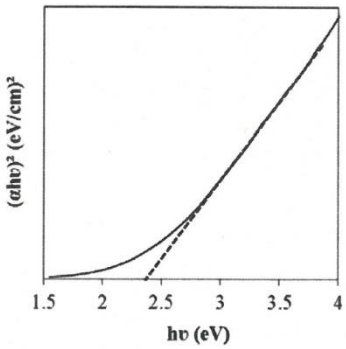

Fig. 6. Tauc plot of Mn_3O_4 nanoparticles.

bandgap energy of 2.35 eV. The obtained bandgap energy is slightly higher than but in reasonable agreement with the reported value of 2.23 eV [34].

3.2. Oxidative catalytic degradation of Rhodamine-B

Fig. 7 shows optical absorption spectra of RhB dye solutions under different pH conditions in the dark and under light irradiation. Fig. 8 gives the magnitude of dye removal as a function of time, in $-\ln(C/C_0)$, where C is the absorbance value of RhB at each reaction time and C_0 is the absorbance value before the irradiation. It is evident that the dye removal was effective only when pH was lower than 5. At pH 9 and pH 7, only 5% and 3% of the dye was removed within 70 min under light and dark conditions, respectively. Lowering the pH to 5 resulted in the magnitude of dye removal to reach 10% and 5% with and without light irradiation. Upon lowering the pH to 3, the magnitude of dye removal increased further to reach 31% and 26% under light and dark conditions, respectively. Similar pH effects were observed on the decomposition of diphenylthiocarbazone by Mn_3O_4 in the past [35]. It was reported that dye degradation by Mn_3O_4 at near-neutral pH was possible only in the presence of oxidising agent H_2O_2, with or without light irradiation [9], or surface modification by citric acid [36].

An attempt was made to calculate the reaction rate constant. Although the magnitude of dye removal at pH 5, 7 and 9 was very low, it was possible to fit the data points with a pseudo first order kinetic model as shown in Table 1 and Fig. 8. However, dye removal at pH 3 did not follow first order nor second order kinetics (Fig. 8, Fig. S1).

There are two probable mechanisms for dye removal; adsorption and oxidative decomposition. The adsorption of dye species on the catalyst surfaces is enhanced by electrostatic attraction between dye molecules and catalyst surface. This occurs within a pH range where the dye and catalyst have opposite electrostatic charges. RhB is a cationic dye. The isoelectric point (IEP) of Mn_3O_4 we measured was 3.6 (Fig. S2), similar to the reported IEP values of Mn_3O_4, 3.3–5.2 [37]. Above this IEP, the particle surface is negatively charged due to de-protonation. As such, it can be expected that the adsorption of RhB on the Mn_3O_4 surfaces is stronger above pH 5. However, the experimental results (Figs. 7 and 8) do not support this assumption; the reduction of RhB concentration by Mn_3O_4 was stronger when pH was lowered below the IEP. Therefore, the major cause of the dye removal by Mn_3O_4 at pH 3 cannot be attributed to adsorption.

Chowdhury et al. discussed that the oxidative catalysis by Mn_3O_4 at a low pH is due to heterogeneous surface oxidation associated with reductive dissolution [38]. In this model, an organic compound forms a precursor complex on the surface of Mn_3O_4, where electron transfer occurs from the organic compound to Mn_3O_4, followed by the release of oxidized organic products and Mn^{2+}. According to this model, the oxidation rates of organic compounds by Mn_3O_4 decrease with increasing pH values, due largely to the fact that the redox potential of the catalyst increases as the pH decreases according to the Nernst

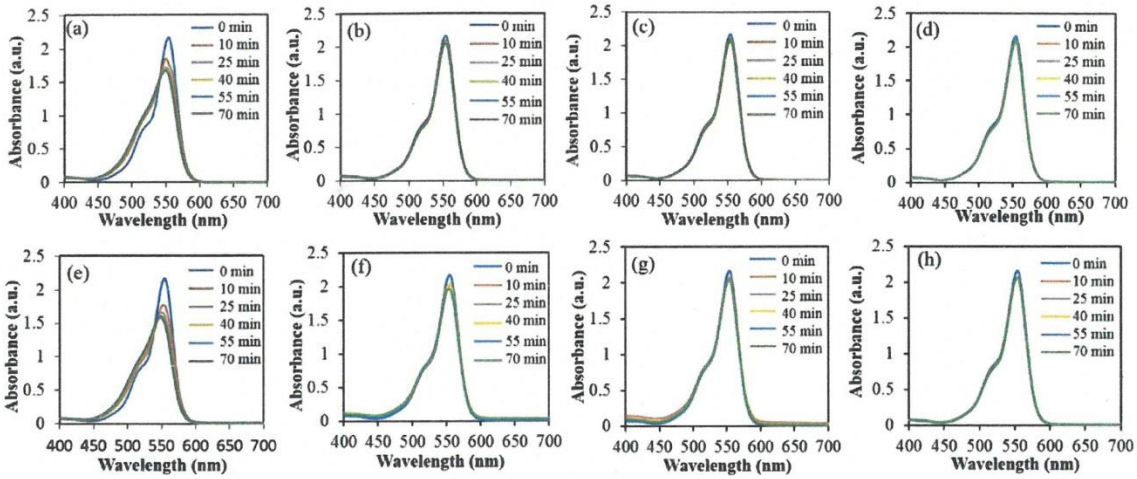

Fig. 7. Exposure time profiles of UV–Vis absorbance spectra of Rhodamine-B solutions in the presence of Mn_3O_4 in the dark at (a) pH 3, (b) pH 5, (c) pH 7, (d) pH 9 and under light irradiation at (e) pH 3, (f) pH 5, (g) pH 7, (h) pH 9.

equation [39]. The result in the present study supports this model to describe the pH dependence of oxidative catalytic dye degradation by Mn_3O_4.

It is speculated that, increased solubility of Mn_3O_4 in an acidic environment assists the oxidation of organic compounds. At a low pH, Mn_3O_4 can be reductively dissolved to form Mn^{2+} instead of Mn^{3+} [40], as Mn^{3+} is unstable in water [41]. Hence the dissolution of Mn_3O_4 in the presence of dye molecules can accompany redox reactions and, in turn, oxidative decomposition of the dye.

The present study showed that, with light irradiation, the degradation rate of RhB was slightly faster at the lower pH (increased by 5% at pH 3 and 5 as compared to 2% at pH 7 and 9). The enhancement by light irradiation may be attributable to photo-induced dissolution of Mn_3O_4 [42,43] where the change in oxidation states from $Mn^{3+/4+}$ to Mn^{2+} promotes oxidative degradation of RhB [44]. Mn_3O_4 has a bandgap energy of ~2.35 eV that is suitable for visible light absorption, but photocatalytic dye degradation by Mn_3O_4 would be negligible. This is because the valence band edge position of Mn_3O_4 is ~1.2 eV v.s. NHE, below the electrochemical potential of the reactions to directly oxidized OH^- and H_2O into •OH radicals (1.99 eV and 2.27 eV v.s. NHE, respectively) [45], so that •OH radicals cannot be photo-generated. In fact, despite some reports showing that impurity doping [46] or combination with photo-sensitizers [47] and graphene [48] enables Mn_3O_4 to act as a photocatalyst, photocatalytic activities of pristine Mn_3O_4 as a stand-alone catalyst has not been reported.

3.3. Free radical scavenging activity

Fig. 9(a–e) show the optical absorption spectra of $ABTS^{\bullet+}$ solutions at different pH levels upon addition of the Mn_3O_4 powder. The absorption peak-height decreased more, as pH levels increased, indicating

Table 1
Dye degradation reaction rate constant.

pH	K (min^{-1}) under light conditions	K (min^{-1}) under dark conditions
5	0.0012	0.0006
7	0.0006	0.0003
9	0.0005	0.0003

that the radical scavenging activity was stronger at higher pH. Similar pH effects were observed for the CeO_2 nanoparticles where antioxidant activity was weak under acidic conditions [49,50]. Fig. 9(f) shows -ln C/C_0 as a function of reaction time at each pH. It is evident that the radical scavenging reaction followed pseudo-first-order kinetics.

Fig. 10 shows the pH dependence of oxidant and anti-oxidant behaviour of Mn_3O_4. Rate constants of the radical scavenging reaction (anti-oxidative behaviour) were calculated from the fitting of -ln C/C_0 plots as a function of reaction time in Fig. 9(f). In Fig. 10, oxidative dye degradation rates are expressed in 1-C/C_0, instead of rate constant, because dye degradation at pH 3 did not follow first-order or second-order kinetics and did not allow the calculation of a rate constant (Fig. 8). Fig. 10 shows that Mn_3O_4 nanoparticles act as an oxidant in aqueous environments below pH 5, while they behave as an anti-oxidant above pH 5.

The mechanism of free-radical scavenging process is due to the presence of mixed valence state $Mn^{3+/4+}$ on the particle surface and can be expressed as [51].

$$Mn^{3+} + ABTS^{\bullet+}\ (\text{blue green}) \rightarrow Mn^{4+} + ABTS\ (\text{colorless}) \quad (4)$$

$$Mn^{3+} + OH^{\bullet} \rightarrow Mn^{4+} + OH^- \quad (5)$$

$$3Mn^{3+} + O_2^{\bullet-} \rightarrow 3Mn^{4+} + 2O^{2-} \quad (6)$$

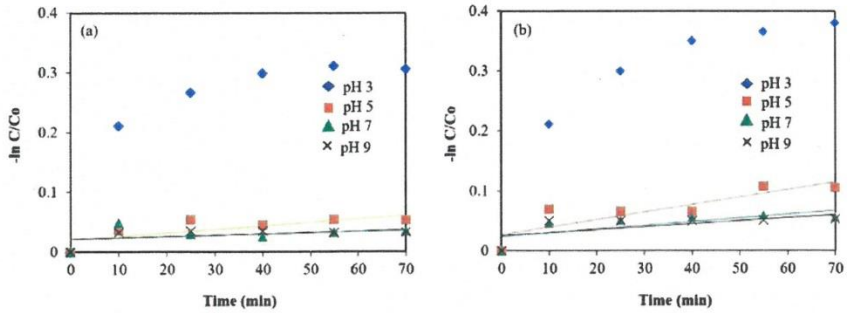

Fig. 8. Dye degradation process at various pH values (a) in the dark, and (b) under light irradiation.

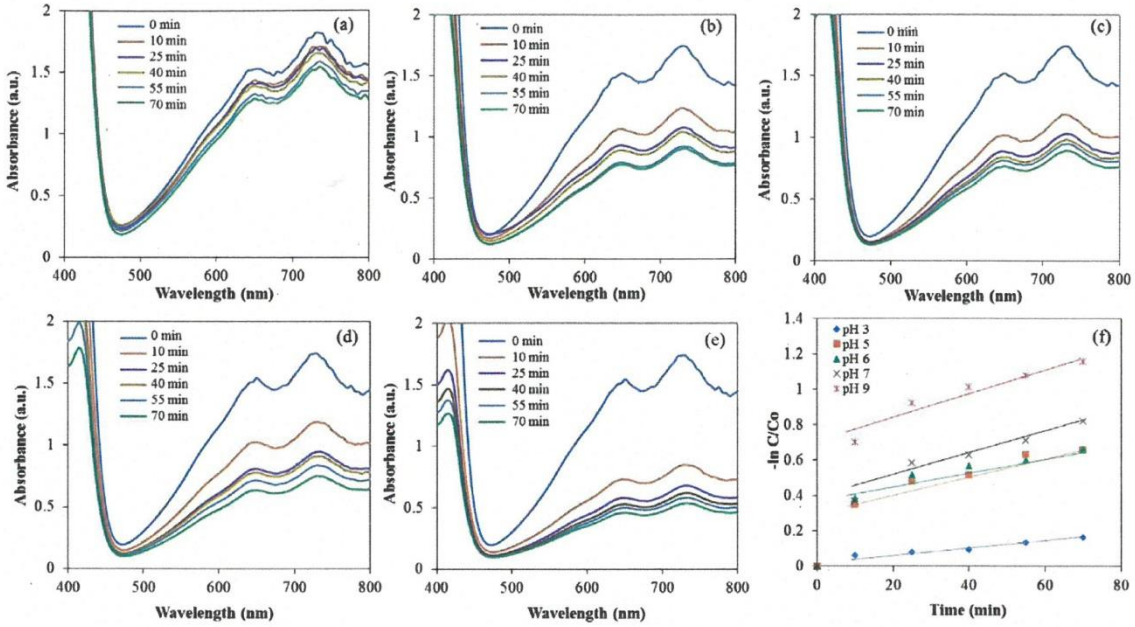

Fig. 9. Time profiles of UV–Vis absorbance spectra of ABTS solutions in the presence of Mn_3O_4 at (a) pH 3, (b) pH 5, (c) pH 6, (d) pH 7, (e) pH 9 and (f) -ln C/C_0 as a function of reaction time.

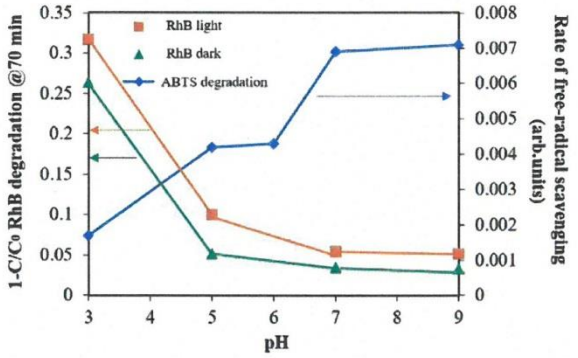

Fig. 10. pH dependent oxidant and anti-oxidant behaviours of Mn_3O_4.

However, at a pH lower than 5, the oxidising activity, that is caused by reductive dissolution of Mn_3O_4, becomes prominent, which reduces Mn^{3+} into Mn^{2+} instead of oxidising Mn^{3+} into Mn^{4+} [44]. This in turn suppresses the radical scavenging reaction at a pH lower than 5.

4. Conclusions

The present study demonstrated for the first time the dry synthesis of Mn_3O_4 nanoparticles by potentially-green mechanochemical processing using a solid-state displacement reaction. It also investigated the pH dependence of their redox catalytic activities.

Mn_3O_4 nanoparticles of < 100 nm in diameter with a low degree of agglomeration were successfully synthesised in two steps. In the first step, a solid-state displacement reaction between $MnCl_2$ and K_2CO_3 resulted in the formation of $MnCO_3$ nanoparticles. The second step involved the thermal decomposition of $MnCO_3$ nanoparticles into Mn_3O_4 under a nitrogen-gas atmosphere. The heat treatment was carried out while the particles were embedded within the solid salt matrix that acted as a physical barrier between nanoparticles, which enabled to achieve a low degree of agglomeration of resulting nanoparticles.

Mn_3O_4 nanoparticles caused oxidative decomposition of a model organic dye but only when pH was below 5, with and without the irradiation of simulated sunlight. The oxidation property in aqueous environments can be attributed to the heterogeneous surface oxidation accompanied by the reductive dissolution of Mn_3O_4. On the other hand, when pH was higher than 5, Mn_3O_4 showed free-radical scavenging properties. Thus, the present study demonstrated that Mn_3O_4 nanoparticles act as both an oxidant and an anti-oxidant, depending on the pH environment. The information is of particular importance to use Mn_3O_4 nanoparticles in biomedical and sustainability-related applications.

Acknowledgment

Ankita Gagrani acknowledges the PhD research fellowship from the Australian National University. The authors also acknowledge the access to the facilities of the Centre for Advanced Microscopy (CAM) with funding through the Australian Microscopy and Microanalysis Research Facility (AMMRF).

Appendix A. Supplementary data

Supplementary data to this article can be found online at https://doi.org/10.1016/j.matchemphys.2019.04.017.

References

[1] A. Bumajdad, M. Madkour, Y.K. Abdel-Moneam, M. El-Kemary, J. Mater. Sci. 49 (2014) 1743–1754.
[2] M. Wiechen, M.M. Najafpour, S.I. Allakhverdiev, L. Spiccia, Energy Environ. Sci. 7 (2014) 2203–2212.
[3] Y. Tan, L. Meng, Q. Peng, Y. Li, Chem. Comm. 47 (2011) 1172–1174.
[4] K.A.M. Ahmed, Q. Zeng, K. Wu, K. Huang, J. Solid State Chem. 183 (2010) 744–751.
[5] S. Xing, Z. Zhou, Z. Ma, Y. Wu, Mater. Lett. 65 (2011) 517–519.
[6] A.J. Carrillo, D.P. Serrano, P. Pizarro, J.M. Coronado, Energy Procedia 73 (2015) 263–271.
[7] Y. Luo, T. Yang, Z. Li, B. Xiao, M. Zhang, Mater. Lett. 178 (2016) 171–174.
[8] C. Ottone, M. Armandi, S. Hernández, S. Bensaid, M. Fontana, C.F. Pirri, et al., Chem. Eng. J. 278 (2015) 36–45.
[9] Y. Wang, L. Zhu, X. Yang, E. Shao, X. Deng, N. Liu, et al., J. Mater. Chem. 3 (2015) 2934–2941.
[10] E.R. Stobbe, B.A. de Boer, J.W. Geus, Catal. Today 47 (1999) 161–167.
[11] Y.-F. Han, F. Chen, Z.-Y. Zhong, K. Ramesh, E. Widjaja, L.-W. Chen, 7 (2006) 739-744..
[12] R. Savla, O.B. Garbuzenko, S. Chen, L. Rodriguez-Rodriguez, T. Minko, Pharm. Res. (N. Y.) 31 (2014) 3487–3502.
[13] G. Karunakaran, M. Jagathambal, E. Kolesnikov, A. Dmitry, A., Ishteev, A. Gusev,

Appendix I

et al., JOM 69 (2017) 1325–1333.
[14] C.W. Choi, S.C. Kim, S.S. Hwang, B.K. Choi, H.J. Ahn, M.Y. Lee, et al., Plant Sci. 163 (2002) 1161–1168.
[15] A. Adhikari, N. Polley, S. Darbar, D. Bagchi, S.K. Pal, Future Sci. OA 2 (2016) 146.
[16] P.L.B. Cheton, F.S. Archibald, Free Radic. Biol. Med. 5 (1988) 325–333.
[17] A. Karakoti, S. Singh, J.M. Dowding, S. Seal, W.T. Self, Chem. Soc. Rev. 39 (2010) 4422–4432.
[18] T. Tsuzuki, P.G. McCormick, J. Mater. Sci. 39 (2004) 5143–5146.
[19] K. Wieczorek-Ciurowa, K. Gamrat, J. Therm. Anal. Calorim. 88 (2007) 213–217.
[20] T. Tsuzuki, K. Pethick, P.G. McCormick, J. Nano Res. 2 (2000) 375–380.
[21] F. Nâamoune, B. Messaoudi, A. Kahoul, N. Cherchour, A. Pailleret, H. Takenouti, Ionics 18 (2012) 365–370.
[22] L.-X. Yang, Y. Liang, H. Chen, Y.-F. Meng, W. Jiang, Mater. Res. Bull. 44 (2009) 1753–1759.
[23] F. Yang, M. Zhao, Q. Suna, Y. Qiao, RSC Adv. 5 (2015) 9843–9847.
[24] Y.Q. Chang, D.P. Yu, Y. Long, J. Xu, X.H. Luo, R.C. Ye, J. Cryst. Growth 279 (2005) 88–92.
[25] D. Chen, S. Ni, G.L. Chen, Z.H. Chen, Adv. Mater. Res. 26 (2007) 671–674.
[26] B. Akbari, M.P. Tavandashti, M. Zandrahimi, Iranian J. Mater. Sci. Eng. 8 (2011) 48–56.
[27] B.D. Viezbicke, S. Patel, B.E. Davis, D.P. Birnie III, Phys. Status Solidi B 252 (2015) 1700–1710.
[28] D. Andreescu, G. Bulbul, R.E. Özel, A. Hayat, N. Sardesai, S. Andreescu, Environ. Sci. Nano 1 (2014) 445–458.
[29] A.M.E. Raj, S.G. Victoria, V.B. Jothy, C. Ravidhas, J. Wollschläger, M. Suendorf, et al., Appl. Surf. Sci. 256 (2010) 2920–2926.
[30] Z. Liu, L. Zhang, G. Xu, L. Zhang, D. Jia, C. Zhang, RSC Adv. 7 (2017) 11129–11134.
[31] N. Li, Y. Tian, J. Zhao, J. Zhang, J. Zhang, W. Zuo, et al., Appl. Catal. B Environ. 214 (2017) 126–136.
[32] F.T.L. Muniz, M.A.R. Miranda, C.M. dos Santos, J.M. Sasaki, Acta Crystallogr. 72 (2016) 385–390.
[33] T. Tsuzuki, P.G. McCormick, J. Am. Ceram. Soc. 84 (2001) 1453–1458.
[34] T. Larbi, A. Amara, L.B. Said, B. Ouni, M.H. Lakhdar, M. Amlouk, Mater. Res. Bull. 70 (2015) 254–262.
[35] K.A.M. Ahmed, K. Huang, Arab. J. Chem. 12 (2019) 429–439.
[36] A. Giri, N. Goswami, C. Sasmal, N. Polley, D. Majumdar, S. Sarkar, et al., RSC Adv. 4 (2014) 5075–5079.
[37] M. Tetsuo, K. Shigeharu, Bull. Chem. Soc. Jpn. 47 (1974) 1586–1588.
[38] A. Chowdhury, M.S. Azam, M. Aktaruzzaman, A. Rahim, J. Hazard Mater. 172 (2009) 1229–1235.
[39] M.M. Walczak, D.A. Dryer, D.D. Jacobson, M.G. Foss, N.T. Flynn, J. Chem. Educ. 74 (1997) 1195–1197.
[40] S. Bakardjieva, P. Bezdička, T. Grygar, P. Vorm, J. Solid State Electrochem. 4 (2000) 306–313.
[41] T. Takashima, K. Hashimoto, R. Nakamura, J. Am. Chem. Soc. 134 (2012) 1519–1527.
[42] J. Han, W. Qiu, W. Gao, J. Hazard Mater. 178 (2010) 115–122.
[43] B.C. Faust, M.R. Hoffmann, Environ. Sci. Technol. 20 (1986) 943–948.
[44] A.T. Stone, J.J. Morgan, Environ. Sci. Technol. 18 (1984) 450–456.
[45] Y. Ma, J. Jiang, A. Zhu, P. Tan, Y. Bian, W. Zheng, H. Cui, J. Pan, Inorg. Chem. Front. 5 (2018) 2579–2586.
[46] T. Yoshinaga, M. Saruyama, A. Xiong, Y. Ham, Y. Kuang, R. Niishiro, et al., Nanoscale 10 (2018) 10420–10427.
[47] S.A.B. Asif, S.B. Khan, A.M. Asiri, Nanoscale Res. Lett. 10 (2015) 355.
[48] A.A. Amer, S.M. Reda, M.A. Mousa, M.M. Mohamed, RSC Adv. 7 (2017) 826–839.
[49] J.M. Perez, A. Asati, S. Nath, C. Kaittanis, Small 4 (2008) 552–556.
[50] B.C. Nelson, M.E. Johnson, M.L. Walker, K.R. Riley, C.M. Simset, Antioxidants 5 (2016) 15.
[51] J. Yao, Y. Cheng, M. Zhou, S. Zhao, S. Lin, X. Wang, J. Wu, S. Li, H. Wei, Chem. Sci. 9 (2018) 2927–2933.

pH dependent catalytic redox properties of Mn_3O_4 nanoparticles

Ankita Gagrani[a], Bolun Ding[a], Yang Wang[a], and Takuya Tsuzuki*[a]

[a]*Research School of Engineering, Australian National University, Canberra, ACT, 2601, Australia*

Electronic Supplementary Information

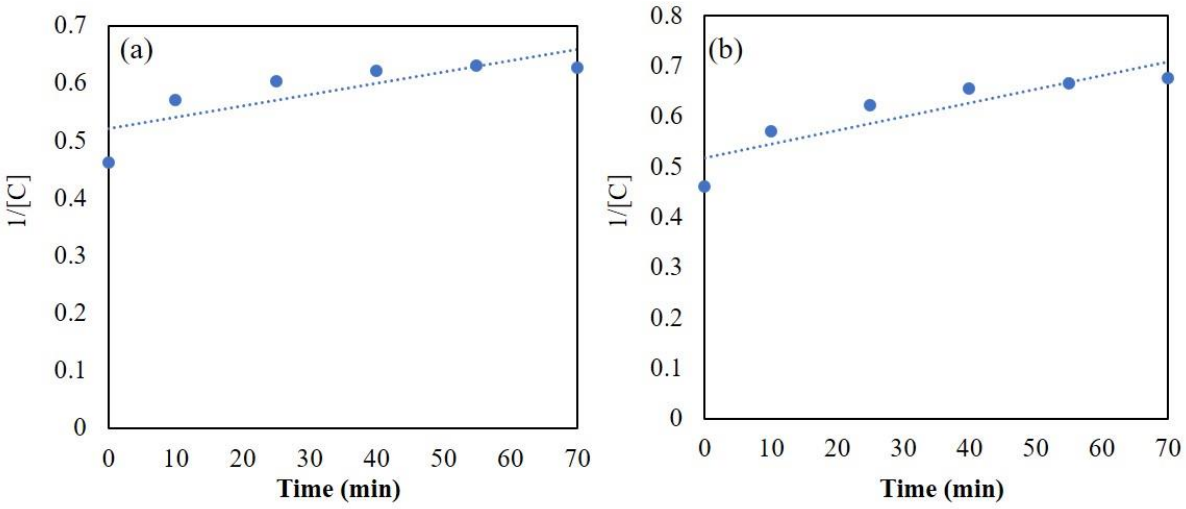

Figure S1. Dye degradation rate at pH 3, (a) in the dark and (b) under light irradiation, showing that the data points do not follow second order kinetics.

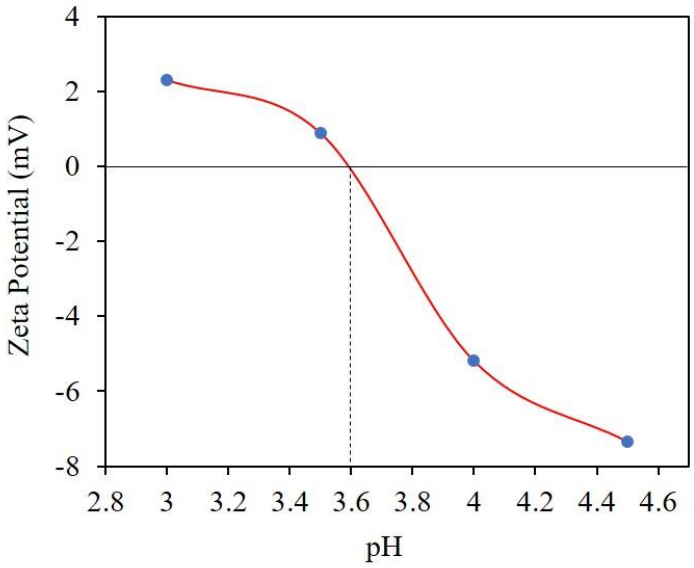

Figure S2. Zeta Potential of Mn_3O_4 at different pH. Blue circle: experimental data; red line: Bezier spline fit.

Appendix II

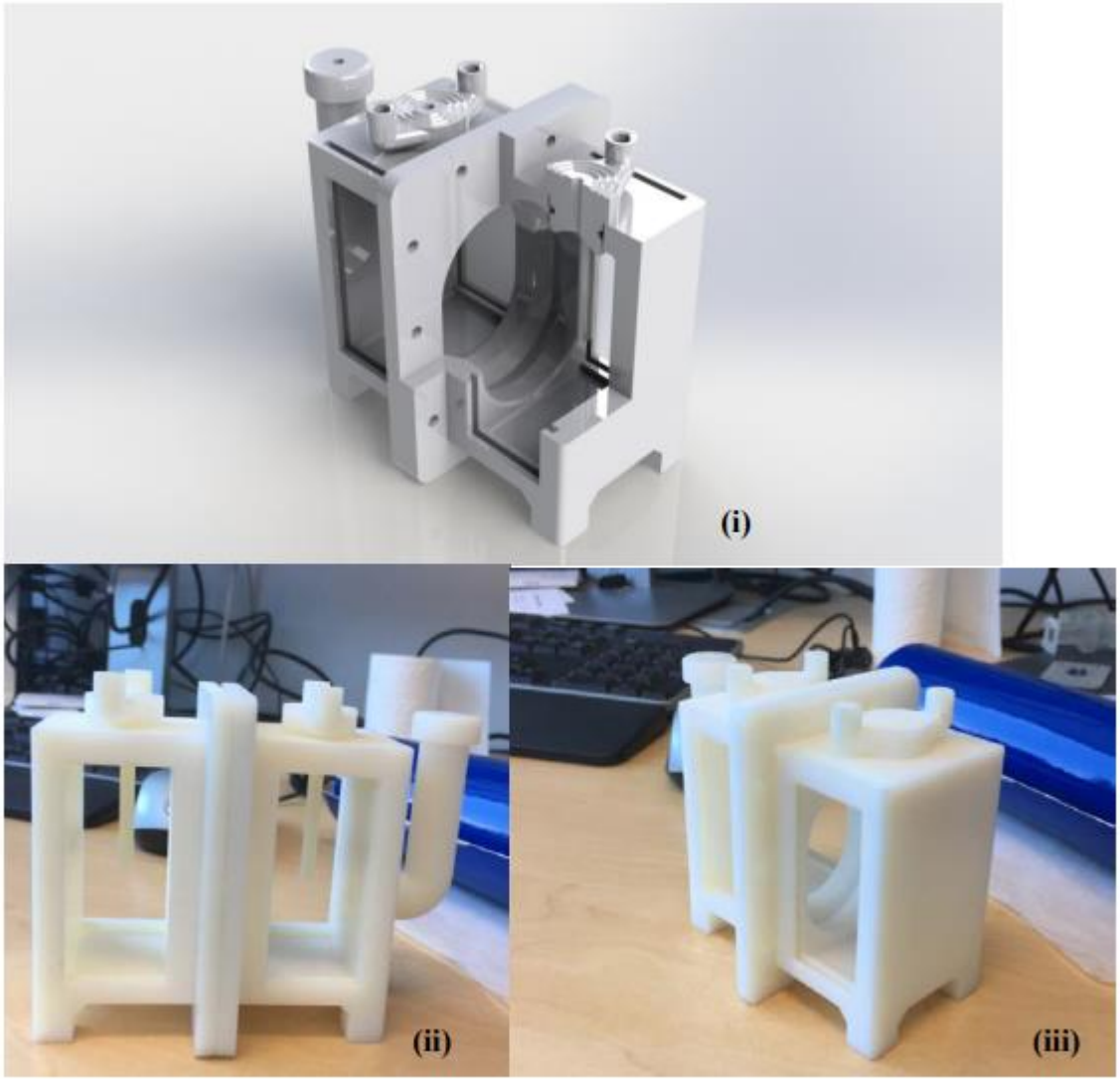

Figure A2.1. (i) Partially cutaway, cross-sectional view (computer-generated) of the sealed cell used in the gas analysis studies; (ii) and (iii) Photographs of the cell prior to being fitted with quartz windows [1].

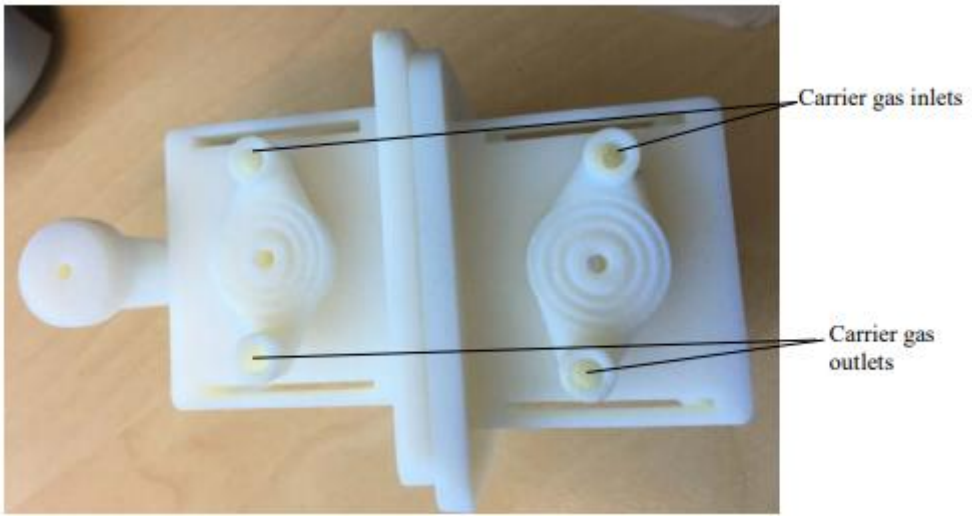

Figure A2.2. Photograph of the top of the cell showing gas inlets/outlets [1].

A2.1 References

Alsultan, M., Balakrishnan, S., Choi, J., Jalili, R., Tiwari, P., Wagner, P. and Swiegers, G.F., 2018. *Synergistic Amplification of Water Oxidation Catalysis on Pt by a Thin-Film Conducting Polymer Composite.* ACS Applied Energy Materials, 1, pp.4235–4246.